Title

Micro/nano acoustofluidics: materials, phenomena, design, devices, and applications

Journal

Lab on a Chip, 18(14)

ISSN

1473-0197

Authors

Connacher, William
Zhang, Naiqing
Huang, An
et al.

Publication Date

2018-07-10

DOI

10.1039/c8lc00112j

Peer reviewed

Micro/Nano Acoustofluidics: Materials, Phenomena, Design, Devices, and Applications[†]

William Connacher,[a] Naiqing Zhang,[b‡] An Huang, Jiyang Mei, Shuai Zhang, Tilvawala Gopesh, and James Friend[a*]

Acoustic actuation of fluids at small scales may finally enable a comprehensive lab-on-a-chip revolution in microfluidics, overcoming long-standing difficulties in fluid and particle manipulation on-chip. In this comprehensive review, we examine the fundamentals of piezoelectricity, piezoelectric materials, and transducers; revisit the basics of acoustofluidics; and give the reader a detailed look at recent technological advances and current scientific discussions in the discipline. Recent achievements are placed in the context of classic reports for the actuation of fluid and particles via acoustic waves, both within sessile drops and closed channels. Other aspects of micro/nano acoustofluidics are examined: atomization, translation, mixing, jetting, and particle manipulation in the context of sessile drops and fluid mixing and pumping, particle manipulation, and formation of droplets in the context of closed channels, plus the most recent results at the nanoscale. These achievements will enable applications across the disciplines of chemistry, biology, medicine, energy, manufacturing, and we suspect a number of others yet unimagined. Basic design concepts and illustrative applications are highlighted in each section, with an emphasis on lab-on-a-chip applications.

1 Introduction

The problems and promise of microfluidics have served to motivate researchers for over twenty-five years. Small volumes, fast processing, dynamic control, low costs, and hand-held devices compete with numerous difficulties in actuation, manipulation, and eventual integration into practical devices.[1] The goal is to replace each step in a macro-scale process with a micro-scale counterpart and then to seamlessly integrate these parts without compromising the advantages, all embodied by integrated devices that can be used by non-experts. In 2014, Sackmann *et al.*[2] raised the question: *Why hasn't microfluidics seen widespread adoption?* Becker[3] noted five years prior to that, in 2009, that the success of any new discipline hinges upon a "killer application", and that microfluidics still lacked one. In the eight years since, much has been accomplished in the discipline, with Becker and Gärtner[4] and others finally expressing a cautiously optimistic outlook.

However, an answer overlooked by many researchers is that much of the benefit of microfluidics is lost when actuation still must rely on an external bench-top pneumatic pump connected by a tangle of tubes—for example, the first figure in Whitesides' review. Such a system is difficult to operate by an expert in a laboratory, let alone a non-expert with a hand-held version. Biological assays represent one of the most important applications for lab-on-a-chip devices, yet requires mixing—difficult via traditional microfluidics where laminar flow is difficult to overcome and diffusion is glacially slow. Passive mixers[5] offer solutions in some cases, but require complex architectures. A good argument was put forth by Collins *et al.*:[6] relying on spatially and temporally distant means of pressure reduces the dynamic control one has over microfluidic processes. Finally, Sackmann *et al.*[2] point out that macro-scale technologies have likewise been advancing and, in order to compete, microfluidics must do better than simply matching the performance of larger technology for the same tasks, a sort of *red queen*[7] evolutionary problem in developing and applying microfluidics technology. In this review, we will show that the actuation of fluids and particles via acoustic waves can overcome these hurdles and help fulfill the promise of microfluidics.

Vibration as a means to manipulate particles within fluids (and gases) has interested the scientific community since the work of Chladni *et al.*,[8] Faraday *et al.*,[9] and Kundt *et al.*.[10] Fluid actuation by acoustic waves is complex in analysis but simple in practice, with little hardware required to operate, and offering large actuation forces and force gradients. The seeds of acoustofluidics date

[a] *Corresponding author: jfriend@eng.ucsd.edu*

[b] *Medically Advanced Devices Laboratory, Center for Medical Devices and Instrumentation, Department of Mechanical and Aerospace Engineering, University of California San Diego, La Jolla CA 92093–0411 USA.*

† Electronic Supplementary Information (ESI) available: [details of any supplementary information available should be included here]. See DOI: 10.1039/b000000x/

from two centuries ago, and acoustics was considered a classic discipline as early as the 1960's. Few new areas of research had developed in acoustics until a recent and dramatic resurgence as a result of interesting results at small scales (*see* reviews on microscale acoustofluidics from Friend *et al.*,[11] Ding *et al.*,[12] Yeo *et al.*,[13] and more recently Destgeer *et al.*[14]).

While some of the effects discussed in this review were known by Chladni, Faraday, Kundt, and their contemporaries, the acoustic devices available to them and fellow researchers until the 1960's were inadequate for small-scale applications. They were either underpowered, providing little more than laboratory curiosities like "quartz wind",[15] or generated ultrasound with wavelengths at centimeter to meter length scales from relatively large, inefficient, and strongly heating transducers. These devices brought with them a collection of side effects from cavitation to weak acceleration unfortunately incompatible with micro/nano-scale fluidics.

Notably, the phenomenon of surface acoustic wave (SAW) propagation on a substrate was first reported by Lord Rayleigh in 1885,[16] but these were only properly produced with the maturation of microfabrication to form interdigital transducers (IDTs), thin finger-like electrodes formed upon a piezoelectric substrate as described by White and Voltmer in 1965.[17] Many of the most recent reports in micro/nano acoustofluidics have relied on SAW generation at tens to hundreds of MHz, which was not possible prior to IDTs and reduces the acoustic wavelength to a scale compatible with microfluidics. There is an ancillary effect that is arguably far more significant. Because the particle velocity in typical acoustic devices is limited to around 1 m/s regardless of size or frequency due to the limitations in material integrity, selecting higher operating frequencies allows a concurrent increase in particle acceleration, to as much as 10^8 m/s^2. It is this very large acceleration that is responsible for many of the observed effects in acoustofluidics.

In this review, we first examine the piezoelectric materials that underpin this transformation in micro/nano-scale fluidics and then describe the basic device architecture used to generate acoustic waves before reviewing the most recent developments in the field. We explore mixing, manipulation of particles, translation, jetting, and atomization in sessile drops, and then consider mixing, pumping, and particle and drop manipulation in closed channels. Nanoscale phenomena are examined as a new direction of work, and the review closes with coverage of an important observational technique, laser Doppler vibrometry.

2 Piezoelectric Materials and Electro-acoustic Waves

Microscale acoustofluidic actuation relies on the generation of acoustic waves in piezoelectric materials. The well-known *direct piezoelectric effect* generates electric charge upon the application of mechanical stress in certain materials; the generation of mechanical strain from the application of an electric field is the *inverse piezoelectric effect*.[18] Atoms or molecules present in the solid lattice structure of the material are either ions in the typical case[19,20] or have strong polarization—a separation of dissimilar charges, forming an electric dipole—in the case of some piezoelectric polymers such as poly-vinylidene fluoride (PVDF).[21,22] In single crystal piezoelectric media formed from ions, the ions exhibit miniscule, thermodynamically favorable misalignment that forms dipoles over each unit cell of the crystal material. This misalignment tends to be identically oriented throughout the crystal, and so its effect accumulates for each repeated unit in the crystal as *polarization*, growing to become physically significant and present in a natural state as *remanent polarization*.[23] Polycrystalline piezoelectric material exhibits similar behavior, though the orientation of the "misalignment" is unique to the *domains*, one or more of which are present in each crystal grain that forms the material.[24] An extremely large voltage is applied to polycrystalline piezoelectric material in the desired polarization direction for a few minutes to several hours while immersed in an inert fluid[25,26] in order to reorient the polarization of each of these domains to generally lie along a particular direction. This step is necessary to form a useful piezoelectric coupling effect in any such media that lacks remnant polarization.

Piezoelectric materials have long been used to generate and detect acoustic waves. Rochelle salt and quartz were employed in the first large-scale application of piezoelectrics to acoustically detect submarines during World War I.[27] The earliest medical applications were for ultrasonic imaging of tissues in medicine.[28,29] High-power ultrasound has been applied in industrial mixing and cleaning, applications familiar to most researchers.[30,31] Other common uses include non-contact sensors and range-finders;[32,33] more recently, local harvesting of energy from motion to eliminate or reduce the need for batteries have driven innovative use of piezoelectric materials.[34] The simplest of all these piezoelectric ultrasonic devices tend to be driven at resonance via planar electrodes on both faces of a flat and thin piezoelectric element, itself polarized from one to the other planar electrode. These may be sandwiched into a rod to form a Langevin transducer,[35] and rarely other modes of vibration are used, usually to generate more complex motion necessary for actuators or motors.[36,37] Regardless of the application, the waves generated by piezoelectric media was generally limited to bulk acoustic waves (BAW) until the advent and broad acceptance of IDTs,[17] which enabled high frequency SAW. The demonstration by White and Voltmer of spatially periodic thin-film metal electrodes on a piezoelectric quartz bar to produce a traveling SAW was broadly taken up by the electronics industry for use in signal processing at frequencies ranging from 10 MHz to 1 GHz. "True" SAW or Rayleigh waves are confined within three to four wavelengths of the surface of the material. Leaky SAW (LSAW),[38] Love waves,[39] Bleustein-Gulayev waves,[39] surface skimming bulk waves (SSBW),[40] and surface transverse waves (STW)[41] are generally categorized as pseudo-SAW (PSAW), may have some limited applications in acoustofluidics, but mainly lie outside the scope of this review.

In order to generate high frequency acoustic waves, a panoply of piezoelectric materials have been used over the last 50 years. Polycrystalline piezoelectrics can be fabricated in more and simpler ways and have greater electromechanical coupling coefficients than single crystalline piezoelectrics, implying a greater ability to transform energy from one form to the other. However, single crystal materials have higher quality factors, and lower damping than polycrystalline materials, and so the choice of material in a given application is not straightforward.[42] Single-crystal piezoelectric media are however generally compatible with microfabrication facilities whereas, for example, lead zirconate titanate (PZT),[43] the most common polycrystalline ceramic piezoelectric material, is not. Furthermore, PZT is toxic, with significant excess lead oxide present along the grain boundaries,[44] and facing regulations that aim to eliminate it from use.[45] There have been some successes in eliminating lead while retaining good performance from polycrystalline ceramics, most notably those derived from potassium sodium niobate (KNN).[46] The granular nature of polycrystalline piezoelectrics limits their use to relatively low frequencies ($\mathscr{O}$(1 kHz–1 MHz)) due to the finite size of the grains and domains within the material that strongly interact with the generation and propagation of acoustic waves at greater frequencies to generate heat.[47] Though some researchers over the years have synthesized polycrystalline ceramic piezoelectric materials with submicron grain size in an aim to increase the useful frequency range to 100 MHz or more,[48] these materials have not been widely employed. The likely reason is the existence of single crystal materials that operate at high frequencies ($\mathscr{O}$(1 MHz–1 GHz)) with superior characteristics.

The materials most popularly used to make SAW devices include quartz, lithium tantalate (LT, $LiTaO_3$) and lithium niobate (LN, $LiNbO_3$). Others include gallium arsenide (GaAs), cadmium sulfide (CdS), zinc oxide (ZnO), lithium tetraborate ($Li_2B_4O_7$), and langasite ($La_3Ga_5SiO_{12}$).[49] All piezoelectric materials are anisotropic, and because these choices are especially so, the type of wave generated from them is strongly dependent on the material orientation. White and Voltmer[17] used a Y-cut, Z-propagating quartz plate. Shortly after, in the late 1960's Bell Laboratories were credited for the development of lithium tantalate (LT) and lithium niobate (LN) which exhibit significantly stronger electromechanical coupling coefficients than quartz.[50,51] Due to its exceptionally high coupling coefficient relative to other single crystalline materials for SAW, LN has become ubiquitous for this application. Typically, wafers are obtained by growing a boule (*see* Fig. 1) of LN from a seed crystal with the desired orientation, which is cut into wafers of the required thickness.

Initially, SAW devices were designed so that waves propagated along the symmetric crystal axes. Later on, as enhanced properties along different rotated cuts were discovered, these cuts gained popularity in various applications. In particular, the Y-cut, Z-propagating orientation of LN (YZ LN) was extensively used for SAW filters requiring Rayleigh waves. Due to the dependence of wave velocity on the propagation direction in an anisotropic material like LN, waves in rotated cuts propagating in a direction not aligned with a principal axis in the material translate laterally in a phenomena known as *beam steering*.[52] With further studies, particularly the works of Takayanagi *et al.*[53] and Slobodnik *et al.*,[54] the 131° Y-rotated cut of LN was found to have exceptional electromechanical coupling and low beam steering and became widely used. However, this cut exhibited spurious parasitic waves, and in 1976, Shibayama *et al.*[55] determined that the 127.86° Y-rotated cut reduced the generation of these parasitic waves and consequently had the highest electromechanical coupling coefficient and lowest insertion loss. The 127.86° Y-rotated X-propagating cut of LN (128° YX LN) became the most popular and widely accepted orientation for applications requiring Rayleigh waves. Other cuts of LN have even higher electromechanical coupling coefficients, but these produce spurious modes and beam steering that preclude them from applications requiring "true" SAW. Among the other cuts, the 36°, 41°, and 64° Y-rotated cuts are the most popular. Table 1 lists some of the best-known cuts of LN and their electromechanical coupling constants, where $K^2 = 2\Delta v/v = 2\left(v_f - v_m\right)/v_f$. Here, v_f is the wave velocity in the free substrate and v_m is the wave velocity measured along a short-circuited plane.

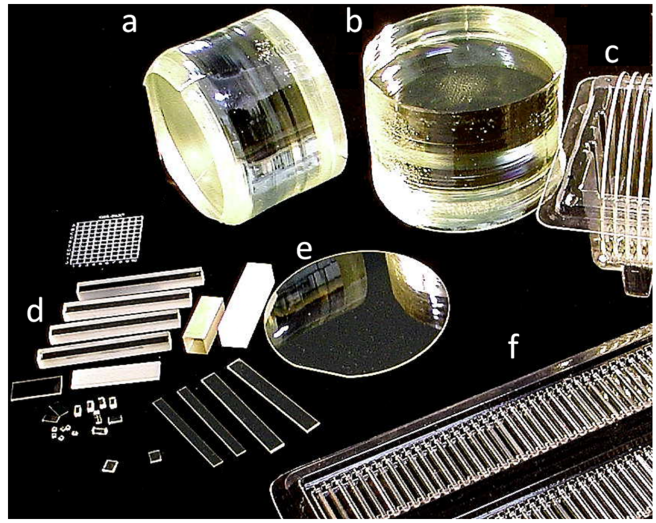

Fig. 1 (a, b) A boule of LN, (c,e) with wafers and (d,f) other shapes cut for typical applications. *Image provided by Precision Micro-Optics, MA, USA.*

Table 1 Commonly used cuts of LN and their corresponding electromechanical coupling coefficients and velocities. Reproduced with permission from Shibayama *et al.*,[55] Campbell,[56] Ciplys *et al.*,[57] Soluch *et al.*[58] and Hickernell *et al.*[59]

Cut	$2\Delta v/v$ (%)	Velocity (m/s)
YZ[57]	4.82	3488
ZX[57]	0.53	3798
ZY[57]	2.25	3903
XY[57]	3.58	3748
20° XY[58]	1.6	3727
120° XY[58]	4.1	3403
XZ[57]	5	3483
YX[57]	1.54	3769
36°[56] YX	16.7	4802
41° YX[59]	17.2	4752
64° YX[59]	10.8	4692
128° YX[55]	5.3	3992

Evidently, the 41° and 64° YX cuts of LN have higher electromechanical coupling coefficients than the 128° YX, however, these generate PSAW and not "true" SAW/Rayleigh waves. Cuts that produce non-Rayleigh SAW have been used to make SAW resonator filters[60] (64° YX) and delay lines for liquid sensors[61] (41° YX) among other applications.

The majority of research conducted with SAW for microfluidics has utilized 128° YX LN. Recently, there have been some studies which demonstrate the use of X-cut LN.[62] Materials most commonly used in acoustofluidics are anisotropic in nature due to their crystal structure. The 128° YX and X-cut LN, for example, can generate SAW of the same frequency and amplitude only in one direction. Any veering from the primary propagation direction is affected by beam steering and changes in frequency and electromechanical coupling coefficients. Kurosawa *et al.*[63] demonstrated this for a two-axis motor made using the 128° YX LN wafer, showing that the vibration displacement and velocity were 200% higher in the X-axis propagation direction compared to the Y-axis propagation direction. In order to overcome the anisotropic nature of the substrate, Guo *et al.*[64] and Devendran *et al.*[65] demonstrated perpendicular IDT pairs at 45° to the X-axis to create an orthogonal standing wave of the same frequency. However, the issue of *beam steering* remains. The superior electromechanical coupling present along the X axis and the unmatched wave velocities along the X and Y axes contribute to wave propagation with a lateral component. As a result, high frequency SAW devices made using LN substrates are limited to a single direction for acoustic wave propagation if optimal performance is desired.

2.1 Acoustic Wave Measurement

A laser Doppler vibrometer (LDV) is an interferometer that uses the Doppler effect to measure vibrations. When light encounters a moving surface, the reflected light incurs a frequency shift depending on the velocity of the surface and the wavelength of the light. In an LDV, the laser is split into a reference beam, directed straight to the photodetector; and a measurement beam, which reflects off the vibrating surface before being combined with the reference beam at the photodetector. This superposition creates a modulated signal, thus revealing the Doppler shift in frequency (*see* Fig.2). Signal processing and analysis provide the vibrational velocity and displacement of a point on the surface in the direction normal to the surface. The in-plane motion can be measured using a different configuration where two measurement beams impinge on a spot with an angle between them, thus yielding interference fringes, though other methods exist.[66] As well, the LDV can be operated in scanning mode so that sequential measurement at many points reveals the vibrational motion of a portion of the surface with desired resolution. These and other advances are covered by Castellini *et al.*[67] and a more recent review was published by Rothberg *et al.*[68].

The LDV has been extensively used in aerospace,[69] automotive,[70] and hard disk drive[71] industries, and for land-mine detection.[72] The technology has also been broadly accepted for use in microelectromechanical systems (MEMS) applications.[73] In the context of acoustofluidics, the LDV is well-suited to measure and characterize vibrational motion in the solid surfaces of devices. While the primary aim is usually the determination of the resonance frequencies and mode shapes of the devices (*see* Fig.3), the

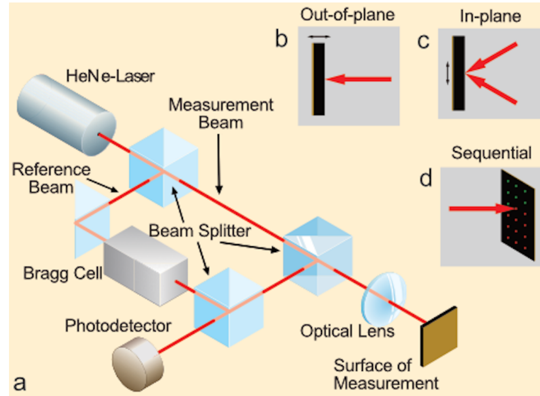

Fig. 2 a) The interaction of the reference and measurement beams to produce a Doppler shift at the photodetector in this configuration of a Polytec laser Doppler vibrometer. b) Out-of-plane vibration measured by a single beam normal to the surface. c) In-plane vibration measured by two beams aimed at the same point with an angle between them. d) Sequential measurement, which is used to obtain the vibration of the surface in phase.

LDV can also be used to identify the type of waveform obtained: Lamb, SAW, BAW, Love, etc. The piezoelectric coefficients (as discussed in Section 2) of materials used in acoustofluidics can also be measured with remarkable accuracy.[74] Due to the high frequencies and small amplitudes involved (especially in SAW), measurement of the vibration driven velocity has been vital for analytical validation which would otherwise be impossible at the micro/nano scale. This capability has been particularly useful for characterization of nanofluidic devices[75] and cantilevers for atomic-force microscopy (AFM).[76] The technology can also be applied to identify vibrations on fluid surfaces[77] and even in air flow.[78] This capability has been helpful in studying fluid atomization and particularly in confirming the absence of the well-known Faraday wave response at half the excitation frequency.[79]

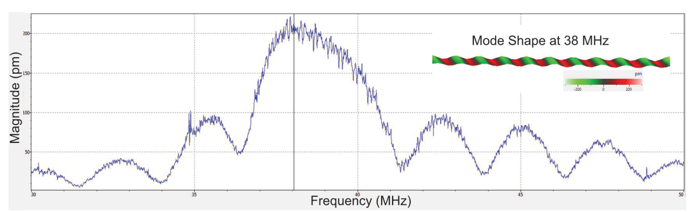

Fig. 3 The resonance mode of a SAW device is revealed by this graph of amplitude vs frequency at a single point over an averaging period while the device is driven with a multi-frequency signal. Once this resonance is known, a sequential measurement over a region of the surface while the device is driven a the resonance frequency reveals the vibration mode, SAW in this case.

The technology has some limitations. The choice of interferometer design has important implications for the sensitivity and measurement range of the LDV, especially in scanning mode. For example, the Sagnac design is inherently more mechanically stable than others due its lack of moving parts (more detail on this topic is provided by Tachizaki[80]). Non-ideal behavior of the interferometer has been known to lead to significant error when measuring small displacements. This and other sources of error, particularly alignment-based error, are covered by Siegmund.[81] Unwanted light waves can interfere with the desired interaction between the reference and measurement beams—known as three-wave interference—but the artifacts of this can be predicted.[82] The vibration of rotating objects and the in-plane motion can likewise be measured, but the setup is relatively complex.[83]

Digital holographic (DH) microscopy has been investigated as an alternative to LDV. Data from a high density of points can be obtained simultaneously using DH but, so far it lacks the ability to provide continuous (non-stroboscopic) measurements at frequencies greater than 1 MHz. Poittevin *et al.*[84] provide a good introduction to the interested reader, and Leclercq *et al.*[85] demonstrate the ability to simultaneously measure three dimensions of displacement in acoustic waves traveling in a solid using three-color DH. Typically, particle tracking is accomplished by optical videography and particle image velocimetry (PIV), but Cacace *et al.*[86] have applied DH to track particles in 3D that are moving under acoustophoresis. In the future, digital holography may enable new insights into previously well studied acoustofluidic phenomena.

2.2 Electronic Communication

The first widespread use of SAW was in wireless communication, playing a critical role in that industry to this day.[87] As filters and duplexers, they provide precise and sharp signal filtering and multiplexing[87,88]. These aspects are relevant to the lab-on-a-chip community for two reasons. First, they demonstrate applications where, like lab-on-a-chip devices, space is at a premium in handheld devices. Second, they indicate potential future routes of research in acoustofluidics lab-on-a-chip applications in analogy to the development of the technology for communications.

The working principle of SAW filters for communication[89] is illustrated in Fig. 4. An IDT (receiver) transfers the incoming electrical signal into SAW by the inverse piezoelectric effect,[90] where approximately 90% of the energy is transmitted in mechanical form and the remainder is transmitted in electrical form to the output transducer (transmitter), where the SAW is converted back to an electrical signal via the direct piezoelectric effect. The IDT design determines the characteristics of the SAW receiver-transmitter combination: a *filter*. The same basic principle has been used for SAW based biosensors, to be discussed in Section 4.2.6. The typical frequency response of a SAW filter is shown in Fig. 4(b). The desired signal shows least attenuated while the rest of the signals are strongly attenuated. This sharp filtering and high selectivity is what makes SAW filters popular in the wireless communication industry.[88,90] Fig. 4 shows the typical frequency response of a SAW duplexer, essentially a combination of two or more SAW filters[91] that provide one-way paths from the transmitter to the antenna to the receiver. The effort made in this discipline solved telecommunications problems at remarkably high frequencies, 1–100 GHz, and laid the groundwork for micro/nano acoustofluidics devices appearing today.

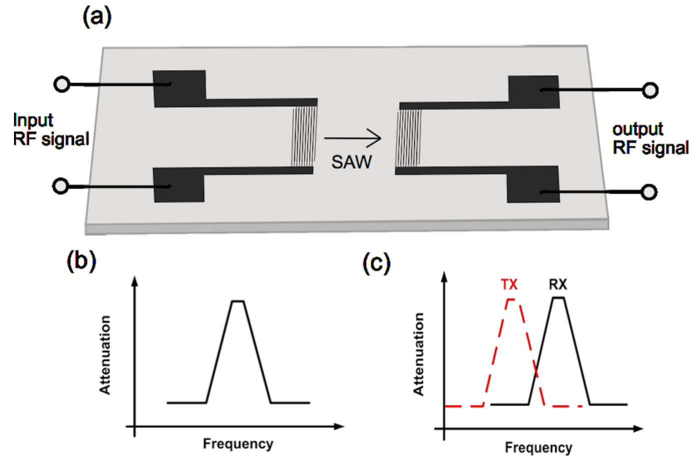

Fig. 4 (a) The working principle of SAW devices in communication. A pair of IDTs are usually included, functioning as an input source (receiver, Rx) and output source (transmitter, Tx), respectively. Typical frequency characteristics of (b) Typical characteristics response of a SAW filters, and (c) SAW duplexers with similar characteristics as SAW filters shown to pass the signals at two different frequencies for cellular applications.

3 Electrode Design

Most acoustofluidic devices use either very simple thickness mode transducers are photolithographically patterned IDTs, which sometimes require complex micro-fabrication. Below we highlight two notable exceptions. Rezk *et al.* proposed a low cost alternative to photolithographic IDT fabrication. Aluminum foil electrodes were simply cut with scissors and clamped in place on a LN substrate to produce a Lamb wave device capable of producing flow in a channel, mixing in a drop, and atomization from a drop.[92] It is likely that this type of electrode will significantly reduce performance due to poor electrical and mechanical contact, but may still be useful for some applications where cost and complexity are extremely limiting. Another alternative to expensive microfabrication was demonstrated by Nam and Lim[93] in the form of patterned conductive liquid, but this method was able to produce IDTs for SAW rather than Lamb waves. Nam fabricated channels in PDMS taking the negative shape of the intended IDT design and these were then filled with eutectic gallium indium. Azimuthal flow was achieved at 162 mW and colored dye could be mixed with a viscous, 25% glycerin solution within one second using 578 mW of power.

The substrate thickness is an important factor in IDT design, as it determines the minimum frequency of the SAW. Most suppliers provide 500 μm thick wafers, and the Rayleigh SAW is known to extend four to five wavelengths of distance into the substrate. This places a lower limit on the frequency suitable to form true Rayleigh SAW of about 40 MHz. Using frequencies below this value cause the acoustic wave to penetrate all the way through the substrate to the other side forming, alongside Rayleigh SAW, spurious Lamb waves that can shed energy through the back side of the substrate into its mounting and affecting the wave propagation and device performance. This is not merely a theoreti-

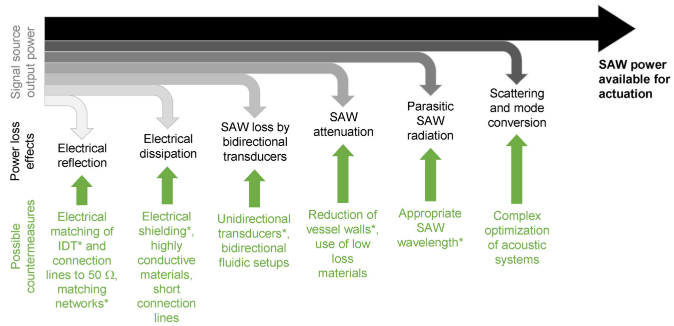

Fig. 5 Power drains in typical SAW microfluidic devices along with proposed engineering solutions. Reprinted from Winkler *et al.* [94]

cal problem, as we have seen (in unpublished work) strong fluid transport in 20 MHz shear-horizontal SAW (SH-SAW) devices that should show no fluid transport at all. The 36° Y-rotated, X-propagating lithium tantalate cut used in this case also generated Lamb waves that appeared to be responsible for the confusing observations.

More importantly, much of the literature reports the generation of SAW at frequencies well below 40 MHz without noting or apparently being aware that this problem could arise. In our case, we were forced to use 20–30 MHz SAW for many years due to limitations of our laser Doppler metrology equipment, and fortunately this problem no longer exists.

In order to realize full miniaturization and widespread adoption, SAW microfluidics will require high power efficiency. Winkler *et al.* laid out the most important efficiency drains in these devices and proposed engineering solutions[94] (*see* Fig. 5). They covered optimal electrical impedance through IDT design, use of unidirectional IDTs, passive matching circuits, passivation and electrical shielding for submerged devices, and choice of wavelength based on geometry. Many of these solutions were utilized in a recent paper[95] demonstrating an atomization specific device, which will be discussed in section 4.2.5.

Heating occurs in acoustofluidics since energy must inherently be dissipated on chip in order to produce fluid and particle motion and resistive heating can be minimized or controlled but never eliminated. This is sometimes considered an issue (e.g. evaporation in digital microfluidics), but can be controlled to support additional functionallity. Shilton *et al.* described the progress made in studying and using acoustofluidic heating, for example in PCR, in their paper on controlling and optimizing this phenomena.[96] Drops could be reliably heated to a stable temperature up to twelve degrees above room temperature within three seconds. The temperature increase was precisely controlled by the frequency and power. This heating was decoupled from the spurious resistive heating due to the IDT.

3.1 Straight IDTs

SAW are typically generated by applying an oscillating electrical signal matching the resonant frequency of the IDT. This signal translates into an acoustic wave via the inverse piezoelectric effect as described earlier. In the literature, frequencies in the 1 MHz–1 GHz range have been used in the study of acoustofluidics, which correspond to wavelengths between 200 and 4 μm for the case of 128 ° YX LN, implying a range of feature sizes of 50 to 1 μm. These feature sizes are typically microfabricated by photolithography and lift-off.[97]

The first and simplest IDTs[17] consisted of straight rectangular metal bars—referred to as fingers—deposited onto the surface of a piezoelectric substrate and alternately connected on either end to contact pads or "bus bars" as pictured in Fig. 6. This structure creates an array of electric fields of alternating direction between the transducer finger pairs that in turn create, via the inverse piezoelectric effect, alternating regions of compressive and tensile strain in the substrate. Each finger pair thus produces displacement in the substrate that oscillates with the electric field and radiates a SAW.[17] The periodicity of the finger pairs defines the wavelength of the resulting SAW (λ_{SAW}) such that the distance from one finger to the next is $\lambda_{\text{SAW}}/4$. The surface wave velocity (v_R) depends on the material properties of the substrate, the propagation direction, and the thickness of the IDT. Consequently, the center frequency ($f_r = \omega/2\pi = v_R/\lambda_{\text{SAW}}$) of a given device is determined by the choice of substrate, propagation direction, and IDT design.[17,98]

The thickness of the metal film that comprises the IDT, h, is typically chosen so that the film thickness ratio $h/\lambda_{\text{SAW}} \approx 1\%$ so as to strike a balance between the efficient transmission of electric current in thicker films and the lower mass present upon the substrate for thinner films. Excessively thin films can cause premature finger failure and localized heating from ohmic losses,[99] while excessively thick or heavy films can reduce the resonance frequency of SAW in the IDT region compared to the surrounding region that have no fingers, unintentionally producing an acoustic cavity. Slightly thicker films, $h/\lambda_{\text{SAW}} \approx 1\%$, are optimal in most cases for reflectors, structures that appear similar to IDTs but act to reflect the SAW on the piezoelectric surface to form an acoustic cavity or improve the device's efficiency. The details of IDT finger design, and the closely related details of SAW reflector design, are provided in substantial detail in Morgan *et al.*[90] and references therein.

As the SAW propagates through subsequent finger pairs, the wave is diffracted, creating a near-field region of largely parallel wavefronts known as the Fresnel region. The far-field region, where the SAW is broadly diffracted along major and minor lobes, is known as the Fraunhofer region. To minimize diffraction losses, the aperture of the IDT must be contained within the Fresnel region. For design purposes, a Fresnel parameter (F) is defined as $F = 4\lambda_{\text{SAW}} D_F/a^2$ where a is the aperture width (shown in Fig. 6 and D_F is the distance from the IDT edge. To remain within the Fresnel region, the aperture should be selected such that $F < 1$.

The efficiency of a SAW device is commonly linked to its quality factor,[100] $Q = f_r/\triangle f$, where $\triangle f$ is the width of the resonant peak in frequency space measured at one-half the peak's highest amplitude. The quality factor is influenced by dielectric losses of the piezoelectric materials, loading effects, ohmic losses, and acoustic leakage to the substrate. The number of finger pairs (N_p) of a SAW IDT is an important parameter partially due to its effect on the quality factor.[90] The other aspect that drives the choice of

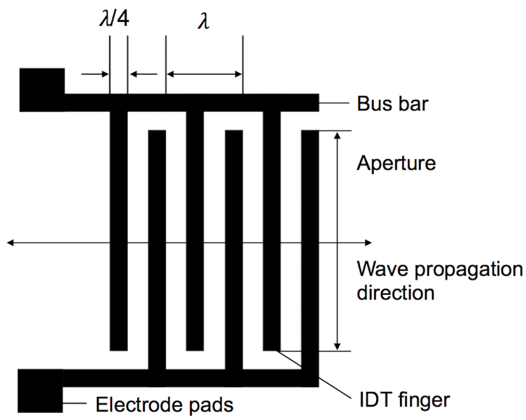

Fig. 6 A SAW device consisting of comb-like interdigital transducers (IDT fingers), bus bars, and electrode pads on a piezoelectric substrate (e.g. 128–YX LN). The resulting traveling wave propagates as shown (perpendicular to the fingers), which can be observed using a laser Doppler vibrometer (LDV). The periodicity of the finger pairs defines the wavelength of the resulting SAW, λ_{SAW}.

the number of finger pairs in a SAW IDT is the effective piezoelectric coupling coefficient of the substrate, which can be defined in terms of the change of SAW velocity from an open-circuit configuration to a short-circuit configuration, divided by one-half of the average of that velocity, $2\Delta v/v$. The greater the coupling, the greater the amount of energy that can be transduced in the IDT to mechanical output as a SAW. The amplitude of the SAW increases with N_p up to a material dependent limit, but the bandwidth is likewise reduced. In signal processing applications, optimizing N_p is a complex procedure.[90] However, when the primary concern is transduction power alone, typical in acoustofluidics, the constraints are simpler. For example, the bandwidth must only be sufficent to allow the device to be driven by signal generation and frequency response analysis equipment.

Optimization begins by defining the electrical admittance ($Y_t(\omega)$) of the IDT, which is dominated by capacitance (C_t), conductance ($G_a(\omega)$), and susceptance ($B(\omega)$), as in $Y_t(\omega) = G_a(\omega) + j(\omega)B(\omega) + j(\omega)C_t$. The equivalent circuit therefore consists of three components in parallel. When a voltage (V) is applied to the transducer, the power that is absorbed and produced are respectively defined as

$$P_a = \frac{1}{2} G_a V^2 \tag{1}$$

and

$$P_s = \frac{1}{4}\omega\varepsilon_\infty a N_p^2 \left(\frac{\triangle v}{v}\right)\left(\frac{\sin(x)}{x}\right)^2, \tag{2}$$

where ε_∞ is the capacitance per period of a unit-aperture, single electrode transducer, which depends on the substrate. At a certain frequency, the susceptance becomes negative and begins to counteract the capacitive term. When these terms cancel out, the admittance becomes real and directly corresponds to a resistive load, and also corresponds to the most efficient operation of the IDT. This occurs when the following equations are satisfied: $N_p = v\pi Q_t/2\triangle v$ and $\triangle f/f_r = 1/N_p$. Therefore, N_p=21 for a single electrode IDT, as in Fig. 7(a), with a bandwidth of 0.05, while N_p = 26 for the double electrode IDT with a bandwidth of 0.038 on 128° YX LN (*see* Fig. 7 (b)).

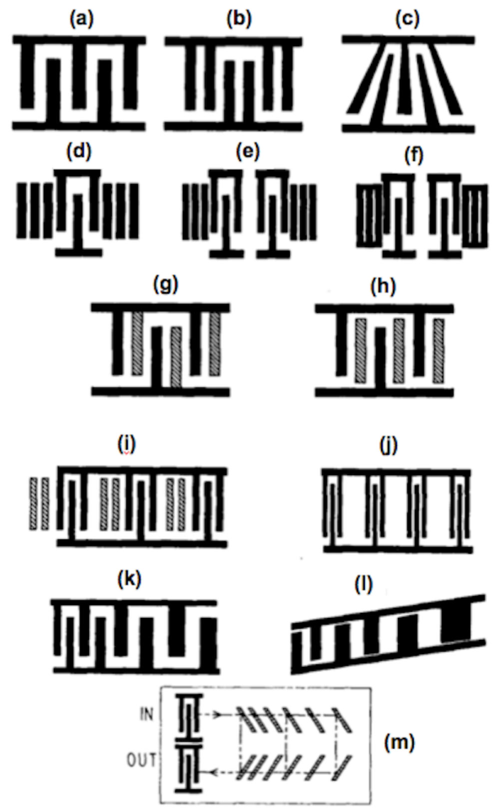

Fig. 7 Common IDT designs for SAW devices: (a) single electrode IDT, (b) double electrode IDT, (c) slanted-finger IDT (SFIT) on collimating substrate shown with exaggerated tilt, (d) one-port resonator, (e) two-port resonator with open-circuited reflection-grating elements, (f) two-port resonator with short-circuited reflection-grating elements, (g) double-metalization single- phase unidirectional transducer (SPUDT), (h) floating-electrode SPUDT,(i) Lewis-type SPUDT,(j) "conventional" comb-filter, (k) chirped IDT, (i) chirped IDT for slanted-array compressor (SAC), and (m) geometry of a reflective array compressor using etched-groove reflectors. Reprint permis. Campbell (1989).[88]

Figure 7 depicts other commonly used IDT designs to fit different design requirements. The double electrode IDT (*see* Fig. 7(b)) eliminates the in-phase reflections produced by standard, single electrode IDTs by producing 180° phase shifted reflections that cancel out. The electrode sampling frequency changes from $2f_r$ to $4f_r$. Ma *et al.*[101] presented a self-aligned method to fabricate double electrode IDTs. The slanted-finger IDT (SFIT) (*see* Fig. 7(c)) is used to generate a wide-band response filter. The maximum angle that can be achieved depends on the coupling coefficient of the substrate. For example, the limit for a YZ LN substrate is 7° due to beam steering losses. The chirped IDT (*see* Fig. 7(k)) has a linear gradient in finger spacing that allows it to resonate at a wide range of frequencies, allowing the excitation of SAW at different wavelengths by tuning the input signal. Another common method of reducing SAW efficiency loss due to in-phase reflection is by adding reflectors, as shown in Fig. 7 (d), (e), and (f). The reflectors are typically the same size as the fingers and are offset by one wavelength from the fingers. Finally, to decrease the reflection loss from a source or finite impedance, a single-phase unidirectional transducer (SPUDT) design is used to cancel out those reflections (Fig. 7(g)-(i)).[56,102] Normally waves radiate in both directions from an IDT, but SPUDTs radiate in only one desired direction, towards the right in Fig. 7.

3.2 Focused IDTs

Compared to the designs described in Fig. 7, focused IDTs (FIDTs) can generate SAW with higher intensity by laterally focusing the SAW energy towards the main axis of the IDT, producing what is called a higher beamwidth compression ratio, $\eta_c = W_b/w$, where W_b is the -3 dB transverse bandwidth and w is the equivalent aperture of the FIDT. They have been utilized in many applications, such as signal processing convolvers,[103–105] storage correlators,[106] and time-Fourier transformers.[107] High intensity acoustic fields can also be generated, and thus enhance the acoustic-electric effect in order to manipulate electron-hole pairs in GaAs quantum wells.[108] Later in this review we will see examples of their use in acoustofluidic devices.

The FIDTs were first introduced by Kharusi *et al.* in 1972.[109] They proposed a structure that consisted of a series of identical curved fingers, so-called conventional circular-arc-shaped FIDTs (*see* Fig. 8(a)), which focus the waves into a narrow rectangular region along the X propagation axis. They discovered that the degree to which the waves were focused and the focal length depended on the anisotropy of the substrate. Their results matched Cohen *et al.*'s finding[110] that the focal length is given by $R_f/(1-2b)$, where R_f is the finger curvature and b represents the anisotropy of the substrate material ($b = 0$ for an isotropic substrate). In addition, they emphasized that the focusing properties of conventional circular-arc-shaped FIDTs do not improve as N_p is increased. Therefore, this type of FIDT was suggested to not be used on a highly anisotropic material, such as LN. In the 1980s, Fang *et al.*[111] calculated the amplitude field of circular-arc-shaped FIDTs on YZ LN and confirmed that the acoustic energy could be focused into a long, narrow region about the propagation axis on a substrate with high anisotropy (*see* Fang *et al.*[111], Fig. 3). Their results showed the beam compression ratio to be about 3% at a distance farther than R_f, which coincided with their experimental data. An important discovery in their work was that the actual focal point for SAW generated from a given set of fingers in the FIDT did not correspond with the geometric focal point. The anisotropy of the substrate typically causes the actual focal point for the SAW to lie up to two times farther away from the IDT than the geometric focal point.

More recently, an alternative FIDT design was investigated by Wu *et al.*[112],[113] consisting of a series of concentric fingers (*see* Fig. 8(b)) that focus the waves to a single spot. These concentric-arc-shaped FIDTs produce higher SAW intensity and beamwidth compression ratios than the conventional circular-arc-shaped FIDTs. The intensity of the SAW is proportional to N_p^2— much stronger than the N_p dependence of a straight IDT with an equivalent aperture. So as N_p increases, concentric-arc FIDTs display a stable amplitude field and better focusing characteristics while the conventional circular-arc FIDTs become unsteady. Moreover, increasing the curvature of the arc does not increase the amplitude, but it does increase the compression ratio, according to Wu *et al.*'s data.

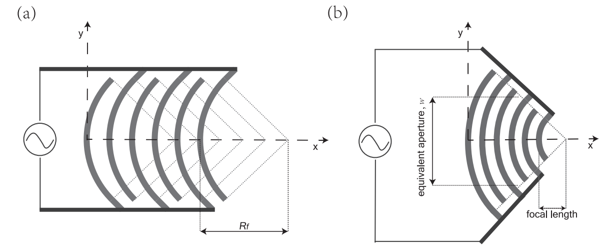

Fig. 8 Commonly used FIDTs designs: (a) conventional circular-arc structure (characterized by R_f as curvature of transducer finger) and (b) concentric circular-arc structure (characterized by w as equivalent aperture). It shows clearly that the concentric design focuses to a point instead of a narrow region, resulting in better focusing property.

Like the traditional FIDT design, modified circular-arc FIDTs exhibit an actual focal point farther away than the geometric focal point due to the anisotropy of the material, as was discussed earlier in the section. Positive values of b in $R_f/(1-2b)$ tend to defocus the transducer, while negative values of b bring the focal plane closer toward the transducer. Shilton *et al.*[114] experimentally showed that a concentric-circular FIDT focused to a point $\sim$1.7 times farther than the geometric center (*see* Fig. 9 (d)). This agreed with earlier work in which Wu *et al.*[113] measured the amplitude vs propagation distance of various configurations of concentric FIDTs and concluded that the actual focal length was $\sim$1.5–1.8 times greater than the geometric focal length. Work done earlier by Kharusi *et al.*[109] recognized this phenomena and suggested another type of FIDT design, the group-velocity surface shape. This type of shape, as its name indicates, consists of points tracked by the end of the energy velocity vector and ensures that waves are focused to a single point despite the dependence of wave velocity on propagation direction in an anisotropic material. The group-velocity surface pattern would become identical to the circular-arc pattern in the case of an isotropic surface. Further investigation by Wu *et al.*[112,113] revealed that this shape is indeed a superior focusing structure, producing a higher intensity and beam compression ratio than the concentric circular-arc shape. An efficient application of this group velocity design was reported by Laude *et al.*[115], as they constructed the IDTs in an fully annular shape following the wave surfaces for Y cut and Z cut LN. The generated SAWs were experimentally proven to greatly overcome the anisotropy of the piezoelectric substrates and converge to an intense spot at the center.

Besides curved and annular FIDTs, there are other designs potentially useful in lab-on-a-chip applications. Riaud *et al.*[116] proposed an array of IDTs (IDTA), which consisted of 32 unidirectional slightly curved IDTs placed along the wave surface of the substrate to compensate for beam steering. By tuning the input signal of each IDT using the inverse filter method,[117] the IDTA was reported to be able to not only focus the waves at an arbitrary position, but also generate swirling SAWs, with an even higher

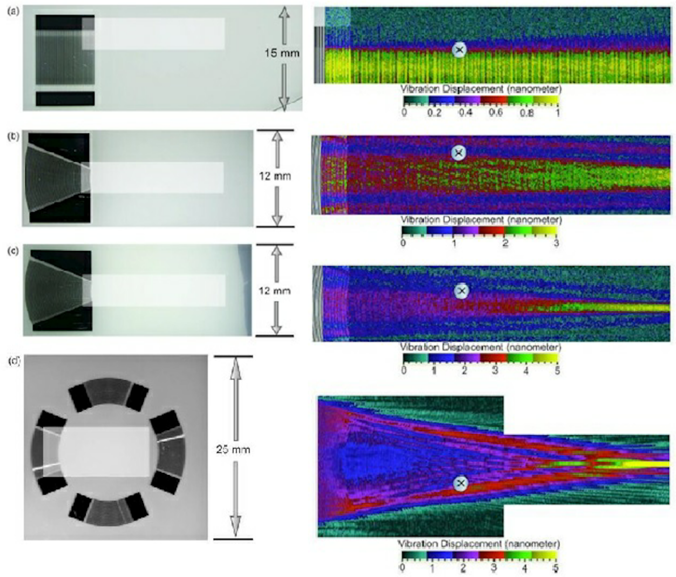

Fig. 9 The distribution of SAW displacement on a LN substrate of different IDT designs at a center frequency of 30 MHz: (a) straight SPUDT, (b)&(c) focusing elliptical SPUDTs with approximate eccentricities of 0.616 & 0.831 respectively, and a (d) focusing circular SPUDT. It shows that the displacement of the SAW produced by straight SPUDT is uniform on the substrate, a line parallel to the propagation direction for the elliptical SPUDTs, and a single point with a circular SPUDT. Reprint permis. Shilton (2008).[114]

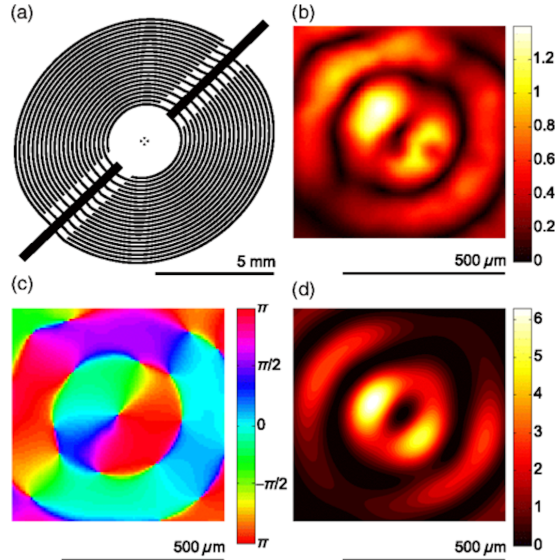

Fig. 10 (a) Single spiraling IDTs design. (b) Experimental substrate vertical vibration amplitude (max amplitude 1.4 nm_{pp} at 7 V_{rms}). (c) Experimental substrate vertical vibration phase. (d) Calculated potential well from experimental data (max height 6.3 fJ). Figures are reprinted with permission from Riaud (2017).[118] Copyright (2017) American Physics Society.

intensity at the center. Later on, an alternative design, called the single spiraling IDT, was introduced by the same group[118] ()*see* Fig. 10) that encoded the SAWs like a hologram and induced acoustical vortices when there was fluid on the surface. Applications of these SAW devices will be further discussed in subsection 4.2.2.

Efforts have been made to visualize the amplitude field generated by FIDTs. Tan *et al.*[119] were able to directly visualize SAW using smoke particles with a mean diameter of 250 nm. The large transverse surface accelerations generated by SAW carry these particles aloft to relatively low vibration regions (*see* Fig. 11). Furthermore, Shilton *et al.*[114] showed SAW propagation patterns generated on a 128° YX LN surface for a straight SPUDT, concentric-elliptic SPUDTs with various eccentricities, and a concentric circular SPUDT by scanning the surface with an LDV (*see* section 2.1. Their results (*see* Fig. 9) offer clear visual evidence that curved IDT fingers focus SAW while straight SPUDTs do not. However, the smoke particle method allows measurement in larger frequency and amplitude ranges and does so in a shorter time compared to LDV visualization. Rambach *et al.*[120] recently introduced another rapid and simple method of visualization using a wetting fluid film on the piezoelectric substrate, where film deformation was induced by acoustic radiation pressure causing a visible contrast between excited and non-excited areas. This method not only makes visualization of the sound path possible, but also possibly exposes the crystal anisotropy and SAW velocity.

The above contributions have allowed FIDTs to be widely employed in acoustofluidic applications where their high intensity and greater bandwidth compression ratio can be utilized. Sessile

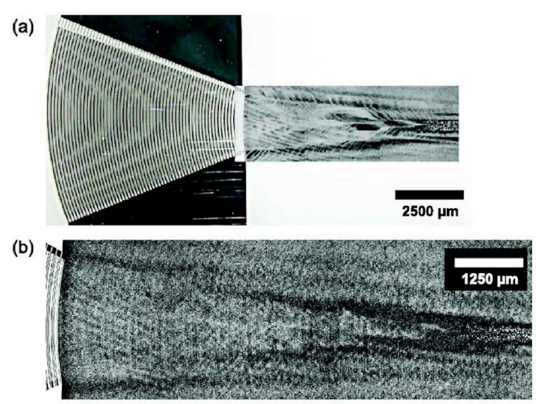

Fig. 11 Visualization of SAW generated by FIDT with 250 nm sized smoke particles placed on the substrate after (a) 15 s exposure, and (b) after 30 s exposure. The distribution of pattern is achieved by the large transverse surface acceleration that carries the particles aloft to relatively quiescent regions nearby via acoustic streaming. Figures are reprinted with permission from Tan (2007).[121]

drop translation and merging, particle concentration and mixing, and cell sorting have all benefited from the use of FIDTs due to their ability to maximize the proportion of acoustic energy that results in efficient acoustic force gradients and acoustic streaming. These advances will be covered in Sections 4.2.2, 4.3, and 4.4.

4 Microscale Acoustofluidics

4.1 Principles of Operation

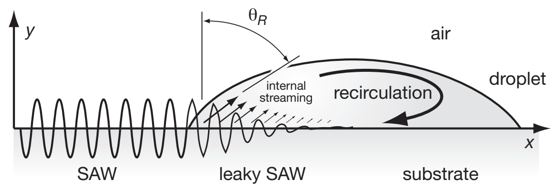

Fig. 12 Sketch of a SAW acting on a small sessile drop. The acoustic energy is diffracted into the fluid at the Rayleigh angle, θ_R, leading to internal streaming in the small fluid volume, which drives recirculation. Adapted from Li *et al.* [122]

Surface acoustic waves propagate upon single crystal piezoelectric substrates with weak attenuation. Upon encountering a fluid on the surface (*see* Fig. 12), SAW "leaks" into the fluid, forming sound that propagates in the fluid and acting to quickly attenuate the SAW in the substrate. The mechanism of the acoustic energy attenuation is balanced by viscous attenuation and dialative dissipation. This can be described as: $\frac{\partial W}{\partial t} + \nabla \cdot J = \rho_0 v_o [b u_0 \cdot \nabla u_0 - u_0 \cdot \nabla \times \nabla \times u_0]$, where W is the acoustic energy density, J is the energy flow, $\nabla \times \nabla \times u_0$ describes the viscous attenuation, and $u_0 \cdot \nabla u_0$ describes the dilatative dissipation. The sound, a progressive longitudinal acoustic wave, travels through the liquid at a Rayleigh angle $\theta_R = sin^{-1}(v_l/v_R)$ Arzt *et al.* [123], where v_l and v_R represent the speed of sound in the liquid and the speed of the Rayleigh SAW upon the solid substrate, respectively. For example, for the case of SAW traveling from 128° YX LN into water, v_l =1485 m/s and $v_R = 3965$ m/s, results in $\theta_R = 22°$.

Generally, the acoustic wave will turn into the media with a slower acoustic velocity, analogous to Snell's law. It is important to remember, however, that modal conversion can occur, allowing acoustic waves to travel across interfaces even when the Snell's law prediction suggests total internal reflection would occur, as explained in Hodgson *et al.* [124] where modal conversion from longitudinal acoustic waves (sound) in a fluid to Lamb waves in a superstrate are found. Furthermore, SAW likewise will leak into viscoelastic solids, particularly those typically used in microfluidics like polydimethylsiloxane (PDMS). While SAW devices can be used in enclosed microfluidics devices that employ PDMS, it is best to minimize the area of PDMS bonding to the piezoelectric substrate over the region carrying the SAW. Inexpensive alternatives to PDMS are possible to mitigate this problem, especially via the use of ultraviolet-sensitive, low-viscosity epoxies for layer bonding. [125]

The length along the surface of the piezoelectric substrate over which a Rayleigh wave decays by a factor of e due to the leakage of SAW into the fluid to transmit sound is the attenuation length $\alpha^{-1} \propto 1/f$: [123]

$$\alpha^{-1} = \frac{\rho_s v_R \lambda_{\mathrm{SAW}}}{\rho_f v_l}, \tag{3}$$

where ρ_f and ρ_s are the densities of the fluid and the solid respectively, v_l is the speed of sound in the fluid media and $v_R = f\lambda_{\mathrm{SAW}}$ is the Rayleigh wave phase velocity. The sound wave in the fluid, on the other hand, propagates uniaxially at the Rayleigh angle [126] and has a distinctly different attenuation length, $\beta^{-1} \propto 1/f^2$:

$$\beta^{-1} = \frac{\rho_0 {v_l}^3}{4\pi^2 f_{\mathrm{SAW}}^2 \left(\frac{4}{3}\mu + \mu'\right)}, \tag{4}$$

where f_{SAW} is the SAW frequency and μ and μ' are the shear and bulk viscosities of the fluid, respectively. Values of the solid and fluid attenuation lengths in the LN-water system were measured by Dentry *et al.* [98] and are listed in Table 2.

Table 2 Attenuation length of the SAW surface displacement at the LN and water interface, expressed as α^{-1} (*see* Eqn. 3) and attenuation length of the sound in water, expressed as β^{-1} (*see* Eqn. 4). Reproduced with permission from Dentry (2014). [98]

f_{SAW}(MHz)	α^{-1}(mm)	β^{-1} (mm)
19.7	2.4	120
54.2	0.87	16
122	0.39	3.1
240	0.19	0.80
490	0.097	0.19
936	0.046	0.052

Attenuation of the sound in the fluid induces a momentum flux responsible for the formation of steady state fluid flow: acoustic streaming. [126,127] Acoustic streaming can be crudely classified depending on the acoustic path length permitted in the fluid and the location of viscous attenuation. Schlichting streaming is the result of viscous shear attenuation near the solid-fluid boundary [128] and Eckart streaming is the result of sound attenuation in the bulk of the fluid. [15] Rayleigh streaming arises from Schlichting streaming. [16] Further details on the types of streaming, their respective characteristics, and previous studies are summarized in Table 1 of the review by Friend and Yeo [11]. In cases where a free fluid surface is present, the nature of streaming and how it causes fluid transport is slightly more complex. [129] In later sections, we will explore how streaming produces fluid and particle motion.

Particle behavior in acoustofluidic systems is typically controlled by the following forces: direct and indirect (Bjerknes) acoustic radiation forces, viscous Stokes drag, van der Waals forces, and electrostatics and electrodynamics. The latter two, van der Waals and electrically-driven forces, tend to be negligible in acoustofluidics, though there have been reports of combining these phenomena to achieve results not possible with acoustics alone. The direct SAW radiation force under a traveling wave was derived by King [130] and is expressed as:

$$F_{rt} = 2\pi\rho_0 A^2 \left(\frac{kr}{2}\right)^6 \left[\frac{1+\frac{2}{9}\left(1-\left(\frac{\rho_0}{\rho_p}\right)^2\right)}{2+\left(\frac{\rho_0}{\rho_p}\right)^2}\right] \tag{5}$$

where r is the particle radius, $k = \omega / v_R$ is the wavenumber of SAW, A is the amplitude of the incident wave, ρ_0 is the liquid density, and ρ_p is the particle density. On the other hand, the radiation force under a standing wave is expressed as:[131]

$$F_{rs} = \left(\frac{\pi p_0^2 r^3 \beta_w}{2\lambda_{\mathrm{SAW}}} \right) \left(\frac{5\rho_p - 2\rho_0}{2\rho_p + \rho_0} - \frac{\beta_c}{\beta_w} \right) (\sin(2kx)) \tag{6}$$

where p_0 is the acoustic pressure, x is the position of the particle, λ_{SAW} is the wavelength of SAW, and β_c and β_w are the compressibility of the particle and the surrounding fluid, respectively. Notice that the radiation force is proportional to r^6 for a traveling wave, but only proportional to r^3 for a standing wave. However, the reader should consult more recent literature by Bruus,[132] Lauga,[133] and Marston[134] to properly take into account fluid and particle compressibility and other important effects. We finally note that acoustic radiation interacts with surfaces in a more complicated way, demanding care in its treatment.[135]

The stream-wise drag experienced by a particle of radius r can be approximated by the Stokes drag equation, $F_D = 6\pi\mu r v_D$, where v_D is the velocity difference between the surrounding fluid and the particle. Finally, the Bjerknes force, an interparticle force arising from the scattering of the incident acoustic wave can be used to describe the interparticle interactions between bubbles[136] or compressible particles.[137–140] The Bjerknes force is defined as:

$$F_B = 4\pi r^6 \left[\frac{(\rho_p - \rho_0)^2 \left(3\cos^2\theta - 1\right)}{6\rho_0 r^4} U^2 - \frac{\omega^2 \rho_0 (\beta_c - \beta_w)^2}{9L^2} {p_0}^2 \right] \tag{7}$$

where U is the particle velocity amplitude, L is the distance between two particles, θ is the contact angle between the fluid and particle, and p_0 is the acoustic pressure amplitude.

4.2 Fluid Manipulation in Sessile Drops

Sessile drops rest on top of a surface and have been successfully actuated by electrowetting, SAW, and even light using special photoresponsive surfaces,[141] forming virtual walls using optical illumination of photoelectric layers.[142,143] The dominant application of these technologies is in biological assays. The reader is referred to the review by Haeberle *et al.* for a comparison of these and other methods for microfluidic lab-on-a-chip platforms.[144] However, none of the other methods are capable of all the types of actuation described in this section.

Both acoustic streaming within the drop and acoustic radiation force on the free surface of the drop can be induced using SAW. Traveling SAW (TSAW) and standing SAW (SSAW) dominate the literature, but other acoustic modes are also useful in select situations. However, we note that acoustic waves in solids are not easily isolated so that unintended modes are often present. These waves, whether SAW or not, deliver sound into a sessile drop at the Rayleigh angle as described in Section 4.1, as long as the wave propagates from a region without the fluid to a region where the fluid is present. In general, the effect of the acoustic wave in the drop depends on the properties of the original wave in the substrate, the properties of the fluid, and the geometry of the drop. We break down manipulation into four regimes: mixing, translation, jetting, and atomization. For each regime, we highlight recent work regarding the basic understanding of the phenomena as well as recent advances in the associated applications. After mixing we pause to consider particles in sessile drops.

4.2.1 Mixing

Acoustic streaming at the Rayleigh angle produces recirculation in a stationary sessile drop (*see* Fig. 12). Almost fifteen years ago, Wixforth *et al.*[145] described the idea of an acoustically-actuated, miniaturized digital droplet lab on a chip, including sessile drop transport and internal mixing with recirculation. The primary internal flow promotes mixing in the drop, but is not generally helpful for other applications such as particle concentration as will be explained in Section 4.2.2. Li *et al.*[122] demonstrated that an azimuthal flow with a vertical component can be induced in a sessile drop from asymmetric SAW exposure on a LN substrate, driving vortical flow about a tilted axis.[146] Li *et al.*[122] provided several designs for generating asymmetric SAW as illustrated in Fig. 13.

Improvements have been made in producing internal flow in drops by exploring other types of acoustic waves. Shilton *et al.*[114] explored circular and elliptical FIDTs in a similar asymmetric exposure arrangement. Elliptically focused SAW produced more intense streaming and thus stronger primary internal flow while circularly focused SAW produced stronger azimuthal flow, concentrating the SAW power to a single small region of size comparable to the SAW wavelength, accentuating the effects of the asymmetric droplet placement.

Theoretical work on acoustic streaming, which induces mixing in sessile drops, was undertaken by Nyborg in the 1960s who suggested that the nonlinear hydrodynamic term due to the Navier-Stokes momentum equation could be neglected .[147] He argued that streaming and the resulting fluid velocity were both second order phenomena and thus the above term was fourth order and negligible. In the 1970s, Lighthill argued that the nonlinear term was only negligible for slow streaming .[126] Shiokawa followed Nyborg's use of an effective body force for calculating streaming velocity in the theory following his experimental work on manipulation of sessile drops using acoustic streaming .[148] Both authors neglect viscosity and argue that the attenuation, which is fundamental to streaming, comes mostly from refraction of the wave at the solid/fluid interface rather than from viscous attenuation.

Most modern numerical work on streaming has closely followed Shiokawa's procedure including a 3D simulation of low power mixing performed in 2010 by Alghane *et al.*[149]. They include the nonlinear hydrodynamic term, but continue to neglect viscosity. They experimentally measured the SAW amplitude as a function of input power and separately measured the streaming velocity as a function of input power. Then, in their numerical calculation, they determined streaming velocity in three spatial dimensions as a function of SAW amplitude and correlated these results to their experiments using a fitting relationship between the two measured quantities. The numerical and experimental results illustrate some simple flows in relatively large drops (30 μL) under relatively low power (up to 0.025 W).

In contrast, Vanneste and Bühler[150] contributed a numerical formulation of acoustic streaming that incorporates viscous attenuation. They derive three contributions to the resulting mean flow: internal Eulerian, boundary Eulerian, and Stokes drift. They point out that without viscous dissipation (as formulated above) Reynolds stress and the pressure gradient are balanced and there can be no mean flow generated in the interior. Instead of using the effective body force in the averaged momentum equation, they use an averaged vorticity equation due to Eckart.[15] The authors are able to apply their results to a variety of geometries, but their solutions are only in two dimensions. Importantly, neither of these two numerical simulations accounts for acoustic radiation force and the reflections that result from a finite boundary.

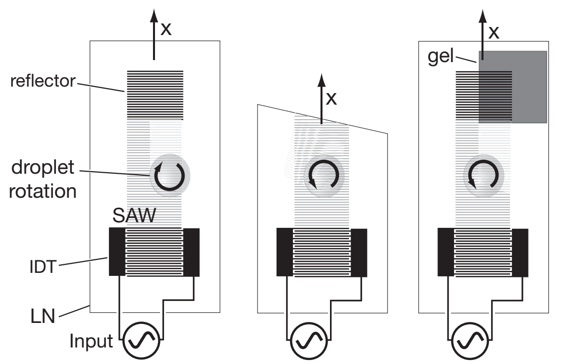

Fig. 13 Three methods used to produce azimuthal flow via asymmetric SAW actuation. (a) Symmetry is broken offsetting the drop from the center line, (b) Asymmetry is generated from the angled edge of the LN substrate, and (c) Asymmetry is generated by absorbing SAW in one region, while reflecting them in another.

In 2014, Rezk *et al.*[151] were able to produce *poloidal* flow using a simplified transducer, a pair of L-shaped electrodes that generate Lamb waves. Poloidal flow only occurred above a critical frequency that was found to be dependent on the diameter of the drop. Lamb waves occur in the bulk of the substrate so their attenuation is different from that of SAW, but the concept is the same. The acoustic streaming-driven primary internal flow from the Lamb wave becomes poloidal flow only when both the acoustic energy impinges radially from all sides and the attenuation length of the Lamb wave in the substrate is less than the radius of the drop as in Fig. 14. Since the attenuation length is dependent on frequency, the existence of a critical frequency is due to the necessity of this attenuation length being less than the drop radius for the poloidal flow to exist.

At the same time, Riaud *et al.*[152] described a more complicated acoustic wave that they claim allows greater control over the internal flow. They suggested the use of helical waves (Bessel beams) to generate cyclone-like flow with both poloidal and toroidal streamlines. Theoretically, the shape of vortices in the fluid can be controlled by the boundary conditions of the fluid and the properties of the helical acoustic waves. Specifically, the axial vorticity is controlled by the acoustic field while the azimuthal vorticity is controlled by the boundary conditions. This result is analogous to the conclusions drawn above regarding internal flow produced by asymmetry and different wave-forms.[153] Riaud *et al.* argue mathematically that these effects are decoupled. This im-

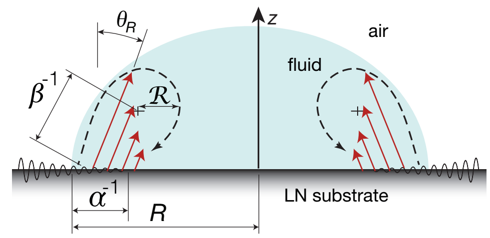

Fig. 14 Poloidal flow is set up in a sessile drop due to the chosen ratio of drop radius, R, to recirculation length, $\mathscr{R}$, which depends on β, α, and θ_R. Corrected and adapted with permission from Rezk *et al.*[92] Copyright (2014) American Chemical Society.

plies that the variables can be independently chosen to produce desired internal flows. They also observed a curious phenomena: fluid flowed *away* from the acoustic energy source when the acoustic beam-width was small compared with the width of the fluid boundary, but flowed *toward* the source when the beam was confined. The authors call these repeller and attractor vortices respectively. The helical acoustic waves used to produce these flow effects can be generated using inverse filtering techniques. In fact, in another paper Riaud *et al.*[62] demonstrate the production of "swirling SAW" by an array of IDTs; in a more recent paper, Riaud *et al.*[118] also use these waves for particle manipulation.

Riaud *et al.*[154] also investigated the effects of viscosity on acoustic streaming flow, showing that it strongly affects the Eckart streaming in the bulk of the sessile drop and therefore should be considered even though it is absent from the velocity expression obtained by a balance of acoustic attenuation and fluid shear. This is an important improvement upon the traditional perspective perhaps best espoused by Lighthill *et al.*[126]: viscosity is crucial to acoustic streaming, yet its specific value is said to not affect the streaming characteristics. This work expands on the simulations by Vanneste *et al.* described earlier. They reproduced experimentally observed flow patterns in sessile drops actuated by SAW with hydrodynamic simulation and were able to show how this relates to the acoustic field. They found that the acoustic field that drives streaming is dominated by a small number of caustics despite the presence of a chaotic field (this chaotic field was quantified earlier by Shilton in the context of flow in microfluidic wells[155]). In the case of a sessile drop on LN they use scaling to reduce the problem to dimensionless numbers for surface attenuation and bulk attenuation that may be used to predict flow patterns in new situations.

One of the major advantages of sessile drop microfluidics is the extremely small sample volumes that are possible. Recently, Shilton *et al.*[156] were able to shrink the size of sessile drops while maintaining control of the flow for mixing, and Miansari *et al.*[75] were able to crudely manipulate 10 fℓ droplets in a nanoslit using SAW.

Generally, these devices are operated below a critical input power necessary to translate the sessile drop across the substrate. This critical power depends on the contact line pinning of the drop, in turn dependent upon the wetting properties of the fluid/surface combination; for example, Shilton *et al.*[153] report the critical power for their arrangement to be 700 mW. Once identified for a given system, this critical power level represents the upper practical limit for inducing mixing, flow, or internal manipulation within the droplet.

4.2.2 Particle, Colloidal, and Cell Manipulation in Sessile Drops

The manipulation of micro-scale objects in fluid by SAW relies on both the acoustic streaming-induced flow described in the previous section and the acoustic radiation force and other forces introduced in section 4.1. Acoustic streaming depends upon the properties of the acoustic wave generated by the source and by the geometry and fluid properties of the drop. The size, density relative to the fluid, and compressibility of the particles determine the effectiveness of acoustic radiation forces upon them.

Concentration, separation, or isolation of target particles are typical needs in biochemical analysis. For dilute samples, an effective collection procedure for the targeted particles can significantly reduce the amount of fluid handling.[157] Particle concentration helps to minimize measurement noise and improve detection sensitivity. Acoustic forces can be used to non-invasively position, concentrate, or fractionate particles. In something of a scientific curiosity, standing waves were first identified by the concentration of suspended particles at acoustic pressure nodal or antinodal planes in a fluid by Kundt and Lehmann in 1874.[158] However, the process was slow, with concentration requiring at least several minutes. Recently, researchers have used SAW devices to accelerate and otherwise improve concentration, separation, and centrifugation.

The position of the particles in sessile drops vary with the drag force and acoustic radiation force applied to the particles. Destgeer *et al.* investigated four regimes of particle position.[159] A droplet with $R > \alpha^{-1}$ has reduced potential for symmetrical vortices. Droplet size and SAW attenuation length also determine whether the acoustic radiation field produces standing waves or traveling waves in the case of counter-propagating IDTs. If $R > \alpha^{-1}$, then TSAW is generated from each side of the drop. If $R < \alpha^{-1}$, then standing waves are set up in the portion of the drop where overlap occurs.

As described in Section 4.2.1, Li produced azimuthal flow in a sessile drop. This type of flow allows particles to be rapidly concentrated at the center of the drop due to shear-induced migration. It is important to note that concentration was only observed in a range of applied power between 150–450 mW while dispersion was observed on either side of this range. This intermediate range of SAW power represents an ideal state below which streaming does not overwhelm particle concentration and above which the particles are transported.[122] Li *et al.* showed that bioparticles remained viable and were concentrated to within 10% of the drops volume under asymmetric SAW actuation. These results show promise for use in conjunction with the bio-sensors discussed in Section 4.2.6 in order to reduce the sensitivity requirements among other applications.

Wilson *et al.* introduced a method using phononic superstrates to achieve programmable complex fluid manipulation on-chip.[160] The phononic structures can produce filter and waveguide effects by scattering and reflecting the SAW without fabricating multiple IDTs on the substrate. They chose a square array of circular holes made in a silicon wafer via dry-etch photolithography and demonstrated centrifugation of 10 μm polystyrene beads and blood cells in a droplet using either a filter-based design or a waveguide-based design. This technique may be useful in certain specialized applications where a single SAW device could be used for multiple types of manipulation depending on the superstrate, which could be switched out as desired. Later on, Riaud *et al.*[116] claimed an improved result from a set of 32 IDTs patterned in a circle and driven by a programmable circuit in order to effectively drive planar waves. They demonstrated droplet division, merging, and atomization with the platform. Moreover, they later demonstrated particle manipulation and positioning through careful control of the signals input into the IDTs.[118]

As mentioned earlier FIDTs can improve fluid actuation in SAW devices. Shilton found that a concentric circular-arc SPUDT was capable of concentrating particles in microliter drops in under 1 second, which is an order of magnitude faster than the straight SPUDT.[114]

Destgeer *et al.*[161] have claimed that the conclusions made by Rezk *et al.* about their poloidal flow, Lamb wave device are incorrectly based entirely on acoustic streaming flow without due consideration of the acoustic radiation force. The experiments by Rezk included only one droplet size (1.5 mm) and single particle size (5 μm), whereas those by Destgeer included a range of particle sizes and droplet volumes, while both researchers varied frequency. Rezk claimed that shear-induced migration caused concentration within the poloidal vortex (*see* Fig. 16). Destgeer found that particles were only concentrated when a parameter representing the balance of radiation force to drag force, $\kappa = \pi d_p f_{LW}/c_f$, was greater than unity (*see* Fig. 15(a)). Here d_p is the particle diameter, f_{LW} is the frequency of the Lamb waves, and c_f is the speed of sound in the fluid. They were able to accurately predict which combinations of particle size and frequency would result in concentrated rings (*see* Fig. 15(b)). However, Destgeer *et al.*[161] failed to take shear migration into account, important in forming such a ring. It may be that poloidal flow is a necessary, but not sufficient condition for concentration in a ring shape, which requires radiation force. The studies agreed that increasing the frequency, and thus reducing the attenuation length in the substrate, moved the concentrated ring towards the perimeter of the drop. Regardless of the precise mechanism, these studies show that particles can be reliably concentrated to a narrow ring at a tunable radius in a sessile drop without the need for microfabricated IDTs.

Other researchers have also played with this balance between flow forces induced by streaming and direct radiation force in order to separate particles. Wood *et al.*[162] were able to efficiently separate and align different sized particles within a drop using SSAW. They fabricated two opposing IDTs with different resonance frequencies on a 128° YX LN substrate in order to set up a periodic distribution of pressure nodes. Rogers *et al.*[163] demonstrated using a 20 MHz device that relatively small particles (2 μm) for which drag force dominates were concentrated in the bulk of the drop, while large particles (30 μm) for which radiation force dominates were driven to the periphery. In their

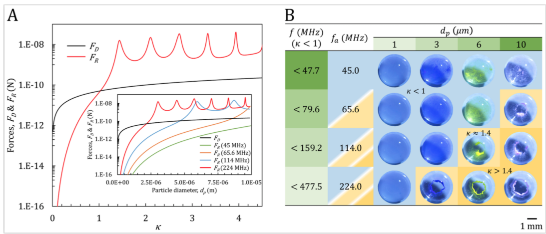

Fig. 15 A) Force vs κ, where F_D is the drag force and F_R is the radiation force. Notice that F_R overtakes F_D at $\kappa = 1$. The inset shows the similar Force vs drop size relationship for various frequencies. B) Each image corresponds to a frequency, drop size pair and the values of κ for each pair are indicated to show that ring formation occurs for $\kappa > 1$, where radiation force dominates drag. Reprinted (adapted) with permission from G. Destgeer, B. Ha, J. Park and H. J. Sung, *Analytical Chemistry*, 2016, **88**, 3976–3981. Copyright 2016 American Chemical Society.

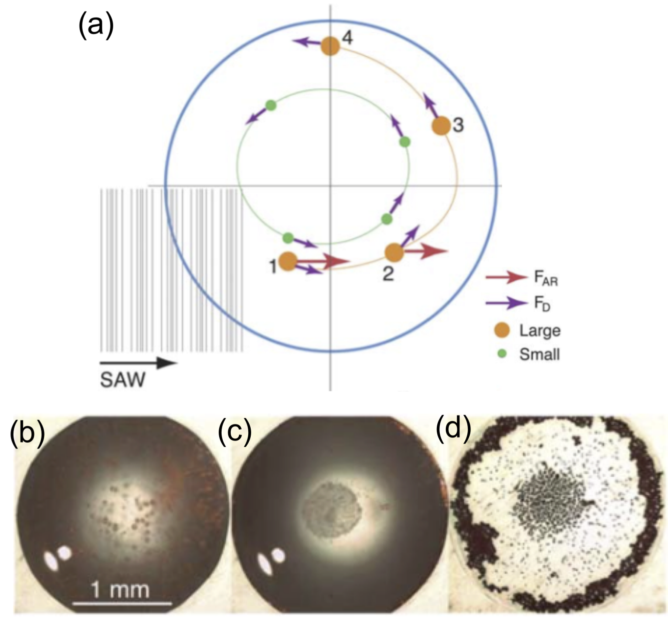

Fig. 17 (a) Larger particles (the size of which are frequency dependent) are dominated by radiation force with the drag force playing a smaller role on the overall particle trajectory. The larger particles in position 1 are driven toward the free surface of the droplet. The effect of acoustic streaming at positions 1-4, however, causes the particles to circulate within a portion of the droplet before they reach the periphery near position 4. The smaller particles recirculate within the droplet until they concentrate in the center under the influence of drag. From experiment: (b) Initially the pollen and synthetic particles were suspended homogeneously throughout the entire droplet. (c) After 3 s, the pollen particles concentrated in the center of the droplet, and are hence separated from the synthetic particles, which concentrated along the periphery of the droplet. (d) The two species remain separated even after the droplet is fully evaporated after 1 min. Printed with permission [163] from The Royal Society of Chemistry.

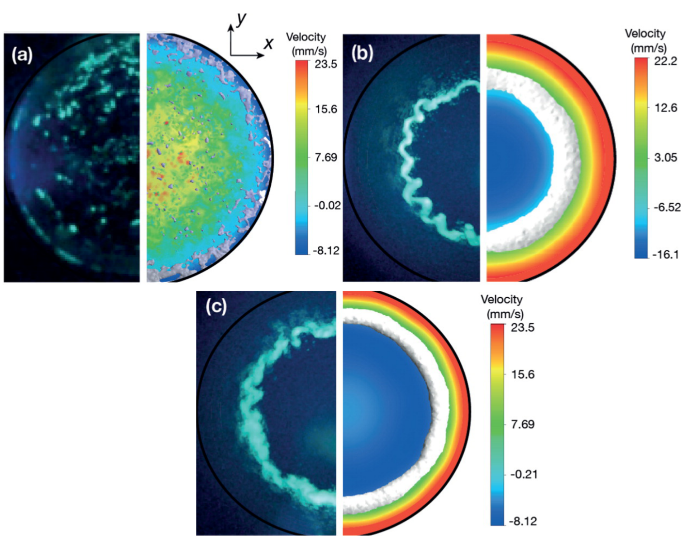

Fig. 16 Experimental images (left) compared to finite element analysis predictions of fluid velocity (right) for a sessile drop actuated by Lamb waves. a) At 25 MHz no vortex is formed. b) At 157 MHz a clear vortex is formed and the particles collect at the lowest shear area. c) At 225 MHz the vortex and particle ring shift towards the perimeter due to a shortened attenuation length. Adapted with permission from A. R. Rezk, L. Y. Yeo and J. R. Friend, *Langmuir*, 2014, **30**, 11243–11247. Copyright 2014 American Chemical Society.

experiments, the large particles were concentrated to the free surface of the droplet within 3 seconds under 400 mW of power (*see* Fig. 17). Bourquin *et al.* [164] used slanted IDTs to generate SAW at multiple frequencies from a single device, which allowed them to separate particles according to their size due to the dependence of radiation force on both frequency and particle size. Bourquin *et al.* [165] later demonstrated particle separation by density using TSAW to generate acoustic streaming inside a droplet. Drag, buoyancy, and gravity forces effect particles to varying degrees based on their density relative to the carrier fluid. As a consequence, when the density of the fluid was between that of the two particles, the high density particles (red beads) were accumulated in the center of the droplet while the low density particles (green beads) were enriched at the periphery. The separation shown was achieved in 3 seconds using 200 mW of power.

The coffee-ring effect is used extensively in stationary sessile drop platforms. [166] Mampallil *et al.* [167] combined this technique with low frequency SSAW to control evaporative self-assembly of particles from a drop placed on a variety of superstrates. Under uncontrolled circumstances, particles in evaporating drops are pulled towards the contact line by convection. They showed that SAW actuation could trap particles within capillary wave nodal

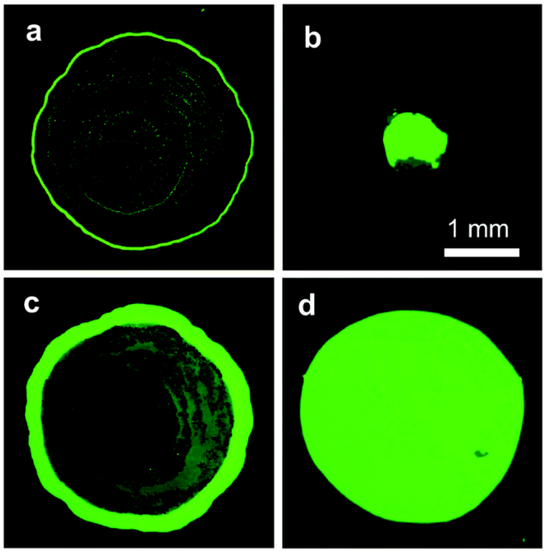

Fig. 18 The coffee-ring effect is suppressed in a sessile drop containing 2 μm particles when actuated with SSAW. a) An undisturbed drop with 0.1% volume fraction of particles. b) A similar drop actuated by 9.7 MHz SSAW. c) An undisturbed drop with 2.5% volume fraction. d) A similar drop actuated by 20 MHz SSAW. All images are post-evaporation. Printed with permission [167] from The Royal Society of Chemistry.

circles and/or SSAW nodal lines and thus prevent this so called "coffee-ring effect." This technique does not require modification of the fluid, particles, or surface involved (unlike other methods). However, in light of the above paragraph on Destgeer's work, it must be noted that their technique does require compatibility between frequency and drop size in order to set-up standing wave nodes. Fig. 18 shows how particles were uniformly deposited in a disc rather than concentrated in a ring near the contact line when SAW were used.

Many other biological assay processes can be enhanced by the use of SAW. Cellular spheroids are useful in diagnostics and drug testing since they resemble the structure and functional performance of *in vivo* tissue. [168] A SAW-driven centrifugation approach was reported to enhance the assembly of cellular spheroids in a micro well plate by Alhasan *et al.* [169]. Acoustic radiation was coupled through a fluid on a LN substrate into the micro well plate placed on top of the SAW device. Centrifugation was driven via acoustic streaming generated by SAW. In this technique microcentrifugal flow in the micro wells—a result of geometric asymmetry—aggregates the cells as a precursor to spheroid formation. Kurashina *et al.* also used ultrasound-generated vortices in well plates in a simple setup to agglomerate cells and reported that spheroids formed by ultrasound were fifteen times larger than without the ultrasound in low cell binding plates. [170]

The influence of flow on particle uptake rates of cells has been studied using SAW-generated acoustic streaming. [171] Acoustic streaming was used to mimic blood flow conditions for cell culturing and the results show that in relatively high shear conditions, particle uptake rates of cells are much lower.

Sivanantha *et al.* [172] studied the influence of 132 MHz focused SAW on the adhesive properties of red blood cells that had been affected by malaria and treated with glutaraldehyde (a common disinfectant used in hospitals) but were nonetheless healthy. The detachment behavior of cells initially adhered to the piezoelectric substrate were observed during exposure to acoustic streaming at various values of input power. The results show that healthy red blood cell membranes translate across the substrate before detachment. Rolling and flipping behaviors are observed for treated and malaria-infected cells. Malaria-infected cells also strongly reattached to the surface in the process. Detachment rates for healthy red blood cells were larger than the modified cells. Adhesive properties of cells have also been utilized to sort cells (HEK293 and A7r5 for example) using acoustic streaming flow. [173]

In addition to cell manipulation, SAW has been used to manipulate smaller bio-particles. Taller *et al.* [174] reported a method to sense micro-RNA, which have potential applications in the early detection of cancer, with greatly reduced sample volumes by lysing exosomes with SAW. Exosomes are much smaller than most cells and the acoustic radiation force and electric field produced by SAW is uniquely suited to their lysis.

4.2.3 Translation

The primary application for sessile drop translation is planar microfluidic lab-on-a-chip platforms. Transport in microfluidics is conventionally achieved by pumping in continuously filled channels, but it can also be achieved with sessile drops using SAW. With this approach, drops are isolated from their surroundings and require smaller volumes, though evaporation can become an issue. [175] The SAW input power must exceed a threshold that arises due to contact line pinning and contact angle hysteresis, which must be overcome in order to translate the drop. These concepts are well explained in a review of surface science by Gao *et al.* [176]

Wixforth *et al.* [177] first demonstrated drop translation using a combination of TSAW and patterning of the surface wettability. Renaudin *et al.* then explored the effects of surface wettability treatments on the power necessary to translate a 2 μL drop. [178] It is important to point out that they used X-cut LN rather than the more common 128° YX LN, which have different coupling coefficients. On bare LN, which is hydrophilic, the drop required 1.6 W and after a hydrophobic treatment it required only 0.56 W. They found that predictable movement required a surface patterned path, but bare LN paths lead to inefficient movement and clearly, hydrophobic paths would lose drops to the surrounding area. In 2007, Tan approached the problem in a slightly different way using elevated teflon strips (10 μm thin) on bare LN [121] (*see* Fig. 19). This technique regained the translation efficiency while avoiding the predictable movement problems encountered by Renaudin *et al.* by using a slightly raised surface to isolate the intended path rather than surface treatment.

Because the acoustic and hydrodynamic response time-scales are radically different, input signal modulation can be used to improve translation efficiency. Both Renaudin *et al.* [178] and Tan *et al.* [121] employed duty cycles in their signals. Renaudin *et al.* found that, at a certain pulse duration, the displacement per pulse was constant with respect to increases in drop volume so that greater efficiency is possible with short pulse width modulation. Baudoin

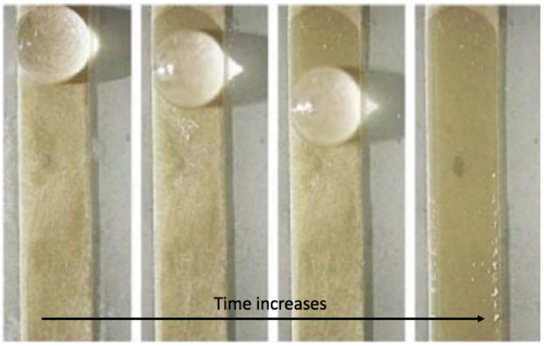

Fig. 19 A water droplet being translated on a 10 μm thick hydrophilic Teflon path atop a LN substrate via a TSAW. Adapted with permission[121] from The Royal Society of Chemistry.

et al.[179] presented a modulation of the SAW by Rayleigh-Lamb inertial-capillary frequencies that reduces the power required for translation by a factor of two. Modulation may also be useful for mixing, jetting, and atomization.

In 2010, Brunet *et al.*[180] numerically and experimentally explored the effects of surface displacement amplitude, drop volume, and viscosity on drop translation. The drop experienced internal flow, asymmetric deformation at the Rayleigh angle, vertical, free-surface oscillations and translation. They observed, as expected, that a minimum amplitude was required for translation, but this minimum did not seem to depend at all on drop volume. In the same set of experiments, varying the amplitude at a fixed volume revealed an asymptotic drop velocity maximum whose value depended on the choice of volume.

There was also a velocity maximum as the volume was varied at fixed amplitude, but this maximum occurred at the same volume regardless of which amplitude was chosen. We can understand this by noting that attenuation of SAW in the substrate indicates how much energy is absorbed by the drop. Maximum velocity occurs when the drop/surface interface is at least as long as α^{-1}. Drops larger than this do not absorb more energy, but gain excess mass and thus move slower.

This study highlights the importance of considering both radiation pressure and streaming. Radiation pressure becomes important when the acoustic beam reaches the drop's free surface before being attenuated. Thus, the size of the drop relative to β^{-1} determines in part the effect of radiation pressure. Brunet observed vertical oscillations in the drops at frequencies and amplitudes (referring to the fluid oscillation not the solid displacement) that correspond to inertial-capillary vibration modes (similar to Rayleigh-Lamb as exploited by Baudoin above). In their interpretation, the free-surface deforms upward due to radiation pressure, but this deformation simultaneously reduces the effect of radiation pressure so that capillary forces pull the drop back down and the cycle repeats. Viscosity had the obvious effect of decreasing the translation speed, but it also reduced oscillations. Since viscosity increases attenuation it reduces radiation pressure and increases streaming. Clearly radiation pressure is critical for translation and for deformation of the free surface.

A drop can also spread as a thin film towards a SAW source

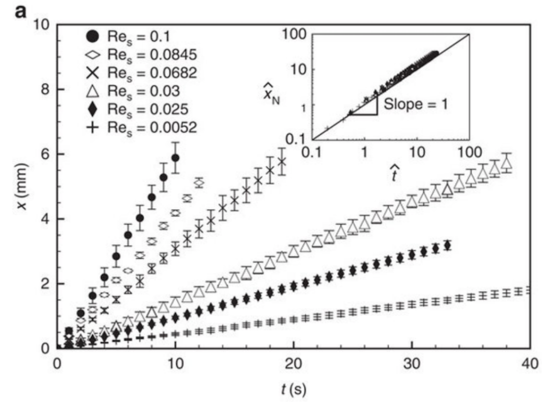

Fig. 20 Experimental results of film front displacement, X, versus time, t, indicating constant velocity for various values of Re_s. The inset shows the same data with X and t normalized based on the derived film evolution equation showing agreement between theory and experiment. Adapted by permission from Macmillan Publishers, Ltd.,[181] copyright 2012.

as shown by Rezk *et al.*[181] (and recently explored by Morozov *et al.*[182]). This phenomena was observed (regardless of fluid type) when the contact angle was small enough (requiring surface treatment in some cases) to produce a region at the edge of the drop where Rayleigh streaming dominated over Eckart streaming. They derived a constant velocity film front by neglecting Eckart streaming and applying appropriate boundary conditions for the region near the contact line. Their derivation matched with experiment across various frequencies, viscosities, and substrate velocities without employing an empirical fitting parameter as shown in Fig. 20. The data is separated by streaming Reynolds number $\mathrm{Re}_s = \rho_f U \lambda_{\mathrm{SAW}}/4\pi\mu$, where ρ_f is the fluid density and U is the particle velocity of the surface. This thin film phenomena was utilized by Collins *et al.* for atomization, which will be covered in Section 4.2.5.

Additional functionality is required if planar SAW microfluidics are to live up to their promise as a lab-on-a-chip platform. The ability to stop, merge, and split drops as well as increased speed are valuable for future devices.

In 2012, Travagliati *et al.*[183] introduced a new tool to effectively detect when a drop has reached its desired location. They drove a drop via SAW towards a cavity with a certain resonance. When the drop entered the cavity, the resonance of the cavity shifted, causing the SAW to be reflected and thus halting the drop.

In the same year, Ai *et al.*[184] applied the concept of focused SAW to translation. They showed that a circular FIDT was able to translate a drop placed just outside its focal distance approximately 5 times faster than a straight IDT under the same power, frequency, and drop size. Though not in strict contradiction, this calls into question the maximum volume-dependent velocity of drops as amplitude is increased described by Riaud *et al.*[154]. Within the focal distance the speed was still 3 times faster and all drops, regardless of location, moved toward the focal point. They suggested that this phenomena may be useful in merging drops.

Indeed, Collignon *et al.*[185] achieved merging by this phenomena, but splitting required a more complex mechanism. A two-part signal (*see* Fig. 21(a)) was produced that first initiated internal rotation and then elongated the drop towards a necking event. Rotational flow due to the first part was critical to suppress jetting behavior allowing sufficient injection of momentum without ejecting the drop. From there a balance of capillary force and drainage due to necking causes the drop to split as seen in Fig. 21(c). Collignon *et al.* performed the task with a range of fluids and obtained a non-dimensional number to predict the capillary bridge effect that ultimately splits the drop; the Ohnesorge number, $\mathrm{Oh} = \mu/\sqrt{\rho_f \gamma R_0}$ describes the balance of inertial and viscous stresses, where R_0 is the radius of curvature of the neck. In Fig. 21(b) we see that splitting occurs in a narrow band at a critical Oh value. We will return to this concept of capillary bridge hydrodynamics in the next section describing the application of jetting to extensional rheometry.

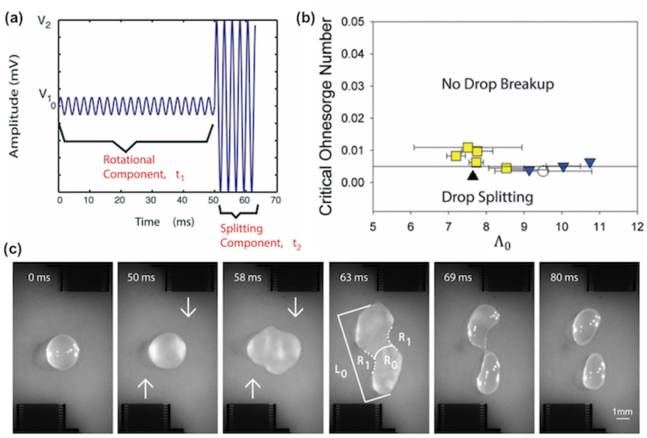

Fig. 21 (a) The waveform of a single pulse used to split a sessile drop via counter-propagating offset SAW. The low-amplitude phase, applied over a period t_1, provides the initial energy for stretching the drop while avoiding jetting. The second, high-amplitude phase is applied over a much shorter duration t_2 comparable to the inertial time scale to rapidly elongate the drop. (b) The relationship between Oh and a dimensionless aspect ratio (Λ_0), showing the collapse of data points representing successful splitting events to a critical value of Oh. (c) A sequence of photographs depicting a successful splitting event with counter-propagating SAW indicated by arrows. Reproduced [185] with permission from The Royal Society of Chemistry.

Though many practical milestones have been reached with regards to sessile drop translation, much of the underlying physics has not been completely explained. Bussonniere *et al.* recently illuminated some of the physics by studying the oscillation, displacement, and contact line dynamics via a high speed camera. [186] They found that displacement of the rear and front contact lines alternately occur during each cycle as seen in Fig. 22. This revelation builds on the work of Brunet and fits intuitively within the context of regimes. The vertical oscillation could reasonably transition to jetting when inertia overcomes the capillary forces. They suggest an explanation for the maximum speed observed by Brunet (when varying amplitude). The speed is given by the product of the net drop displacement per oscillation cycle and the frequency of these oscillations. And, while the displacement is linear with the amplitude of drop deformation, the frequency is nonlinear with the amplitude due to hydrodynamic effects. We will encounter a similar concept in the atomization section. It is currently unclear how this explanation could account for increased speed under focused SAW.

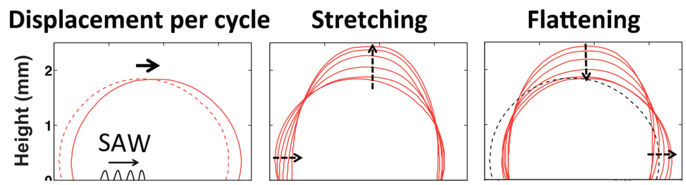

Fig. 22 Oscillation of a sessile drop causing displacement of the rear contact line during stretching followed by displacement of the front contact line during flattening. The pair constitutes one cycle. Reprint permis. Bussonniere (2016). [186]

Droplet transportation using SAW helps to integrate different reaction processes on the same chip. For example, polymerase chain reaction (PCR), which is a DNA segment amplification process developed in the 1980s. [187] This method is critical for DNA sequencing (*see* Section 2 of Yeo and Friend's review for more on this topic [188]). Three main reactions happen at different temperatures in the PCR process: denaturation, annealing, and elongation. After the DNA is amplified, the solution must be hybridized to check the results. Guttenberg *et al.* [175] developed a microfluidic device to direct the reaction of DNA, a primer, and the necessary nucleotides within a sessile drop. Surface treatments define the paths of the drops and resistance heaters are integrated into the surface to promote reaction. They demonstrated successful PCR with only 200 nL drops. With the precise control of droplet translation, PCR and hybridization can be done with the same device.

SAW generated droplet translation also provides a promising, efficient way to seed cells in an external matrix with uniform distribution, an important step in tissue engineering. Cells seeded in bio-compatible, bio-degradable scaffolds have been used to recover defective tissue. [189,190] Li *et al.* [191] reported the use of SAW to seed cells into a scaffold made of polycaprolactone (PCL) in 2007. A droplet containing cells was placed between the scaffold and the SAW source so that the droplet was driven into the scaffold in 10 s. Later, Bok *et al.* [192] studied cells seeded in a scaffold using micro-computed tomography and found it possible to ensure a homogeneous distribution of infused cells. They also observed proliferation of the seeded cells during a fourteen-day continuous culturing study, confirming their viability after exposure to SAW radiation.

4.2.4 Jetting

In general, jetting occurs at a fluid-fluid interface when inertial pressure overcomes surface tension, which tends to maintain the interfacial shape. The well-known Weber number, We is a good metric for this balance; $\mathrm{We} = \rho_f u^2 L_c/\gamma$, where L_c is the characteristic length, u is the fluid velocity, and γ is the surface tension. Viscosity, which intuitively should factor into this balance, is not present in We, but is indirectly expressed via the fluid velocity. More viscous fluids will derive less inertia from a given stimulus. Fluid velocities high enough to overcome surface tension, which increases for smaller fluid geometry, typically require a nozzle so that sufficient inertia can be generated. SAW is capable of producing very large surface accelerations, which translate into fluid velocity for a drop placed directly on the surface, thus eliminating the need for a nozzle.

The interaction between acoustic waves, elastic solids, and liquid drops to produce jets and satellite droplets is very complex.[193] Tan *et al.* attempted to elucidate the phenomenon by focusing SAW from two counter-propagating, FIDTs into various sized drops sitting upon Teflon coated LN.[194] This setup provided a stable drop location and high intensity, which promote jetting over other sessile drop phenomena such as internal flow and translation. Standing wave actuation produced an axisymmetric jet, which was assumed cylindrical. Vertical inertia generated by the focused SAW lead to elongation of the drop and eventually to a break-up event once a threshold input power was exceeded. Below this size dependent threshold, only vibration of the drop was observed (similar to that observed by Bussonniere *et al.*[186]) and above the threshold a Rayleigh-Plateau instability resulted in multiple droplets per jet.

They showed that the various jetting regimes corresponded to a modified jetting We as seen in Fig. 23, where u was replaced by the jet velocity (U_j) and L_c was replaced by the jet radius. They were also able to predict experimental values of U_j for various fluids, graphed in Fig. 24, by modifying the momentum balance derived by Eggers *et al.*[193] for the case of acoustic streaming. It is critical to note that jetting only seems to occur during a pulse of SAW energy, either at the onset of the signal or during a pulsed signal. This was convincingly shown by Wang *et al.*[195] in a detailed, high speed video study of a sessile drop.

Though largely unrecognized in the field, the jetting of fluids using SAW has been applied to extensional rheometry to great effect. Much of rheometry relies on the generation of shear flow in order to observe the diffusion of stress through layers of fluid as one or more fluid layers are caused to slide relative to each other. Another approach is to employ shear-free extensional flows in which normal stresses develop from contraction in two spatial dimensions and stretching in the third. Unlike shear flows, extensional flows are irrotational, implying that any fluid parcels of appreciable aspect ratio will be aligned but will not be caused to rotate, thus fluid parcel alignment will remain constant at steady state. Therefore, measurements in extensional flows qualitatively reveal information regarding fluid behavior down to the molecular-scale.

Creating valid and controlled extensional flow has always been a challenge for rheologists. Filament-stretching extensional rheometry[196] (FiSER) and capillary break-up extensional rheometry[197] (CaBER) are previously developed extensional rheometry techniques; both involve creating thin filaments from sample drops. In FiSER, a liquid sample is placed between two end-plates and the plates are then moved apart at a controlled rate. In CaBER, on the other hand, the plates are rapidly separated to a fixed distance and then held stationary forming a liquid bridge that is allowed to neck and break-up under capillary forces. In either case, the tendency of the cylindrical column of liquid to neck due to capillary stresses is resisted by viscous, and in the case of viscoelastic fluids, elastic stresses. The evolution of the profile of the thinning filament with time is governed by these forces. The flow and the local strain rate at the middle of a thin filament in uniaxial extension can be related to the change in the filament's radius.

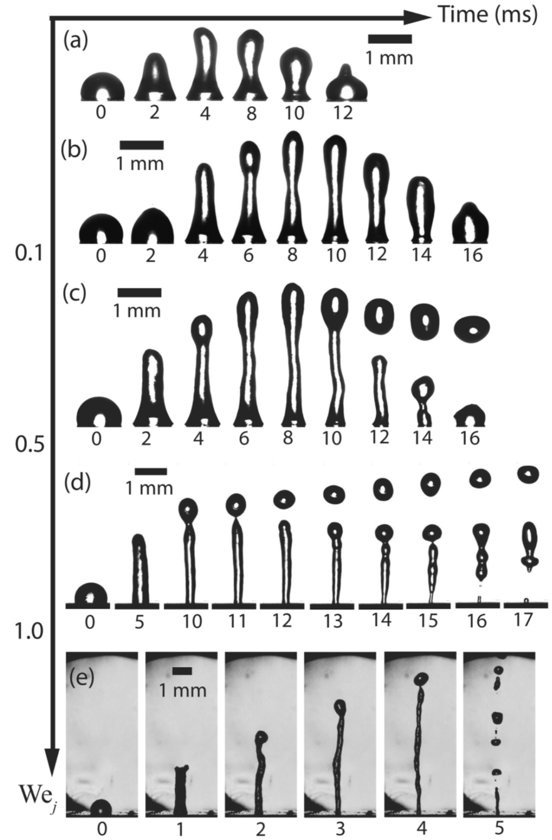

Fig. 23 Jetting behavior according to We$_j$ (on the vertical axis) from an investigation by Tan in 2009. Regimes involving (a) & (b) drop elongation, (c) pinch-off of a single droplet, and (d) & (e) jet breakup to form multiple droplets are depicted. Reprinted figure with permission.[194] Copyright (2009) by the American Physical Society.

Both FiSER and CaBER have been successfully applied to Newtonian and non-Newtonian fluids alike, but it is difficult to test fluids with viscosities less than 100 mPa·s, thus notably excluding aqueous solutions.[197] CaBER requires the initial end-plate opening time to be as short as possible, but typical apparatus require more than 50 ms to open the gap and form the filament. The primary difficulty is that mechanical operation can induce perturbations that seed inertio-capillary instabilities and thus hasten break-up. As a result low viscosity fluids tend to break-up before the filament is formed. Furthermore, relatively large sample sizes are required for both techniques (D=6 mm). Large sample sizes increase the relative effects of gravity on the filament causing it to sag towards the bottom. This produces asymmetric fluid flow around the mid-filament region.

SAW burst extensional rheometry (SAWBER) addresses the above issues in order to make low viscosity fluids accessible to stress and strain measurement in extensional flow.[198] It combines the concept of CaBER with the novel idea of using a burst of SAW energy to create the liquid bridge. This improvement reduces the

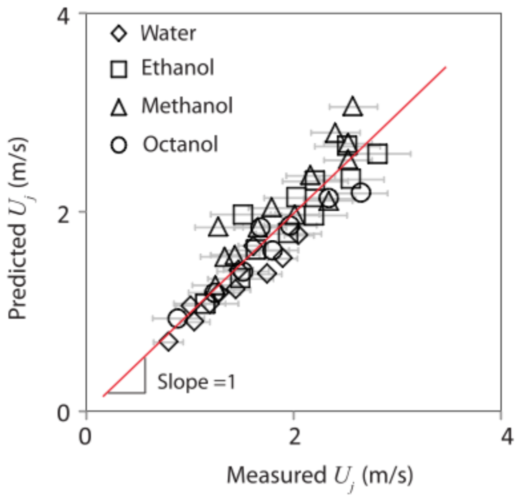

Fig. 24 Comparison of the jet velocities, U_j, predicted by a momentum balance for acoustic streaming with measured values for various liquids. Proximity to the red line with unit slope indicates good agreement between measurement and prediction. Reprinted figure with permission.[194] Copyright (2009) by the American Physical Society.

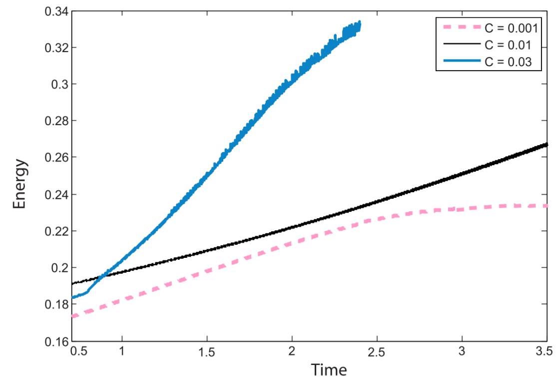

Fig. 25 Interfacial energy vs time for 3 values of C_a (written as C in the figure) from a numerical study of atomization. There is an inflection near $C_a = 0.01$, which is close to the critical value predicted for the onset of atomization. Reprinted[207] with the permission of AIP Publishing.

time required to create a liquid bridge by an order of magnitude (1.5 ms as opposed to 50 ms) and reduces the necessary sample sizes by a factor of two (diameter of 3 mm as opposed to 6 mm). These qualities allow reliable data collection from extensional flows of fluids at viscosities close to that of water. As an added benefit, the use of SAW eliminates the need for mechanical components, which require more maintenance and are less reliable.

The technique involves an arrangement similar to that used by Tan *et al.*[194] (as described above). Energy from a pair of FIDTs generates momentum flux calibrated to elongate a drop of fluid that bridges a gap between the LN substrate and an opposing parallel surface. The SAW burst enables creation of stable liquid bridges which then thin under the action of capillary forces, generating extensional flow at the necking plane. Using high speed videography and image processing, the dynamics of the break-up can then be analyzed. The use of SAWBER was extended for two distinct studies, one involving suspensions of motile microbes[199] and the second for copper nanowire suspensions in aqueous polymer solutions.[200] In the later, viscosities between 3 mPa·s and 37.2 Pa·s were used thus demonstrating that the technique extends the viable range to much lower viscosities while maintaining the high range. In the former, McDonnell *et al.* was able to show that microbes that move by pulling tend to increase the effective viscosity of a fluid while microbes that push tend to decrease it. These studies form the tip of the iceberg in terms of complex low viscosity fluid behavior that could be illuminated using SAWBER.

4.2.5 Atomization

Atomization has received abundant attention in recent years due both to its interesting physics and many important applications. In SAW devices, it tends to occur at higher power inputs than do the phenomena discussed so far. Atomization produces a continuous flow of many small droplets in a tight size distribution and much of the research is undertaken to optimize and predict the relevant parameters. The underlying mechanism of SAW atomization is still not completely clear, but several studies on the effects of viscosity, input frequency, fluid geometry, and acoustic amplitude have been recently completed. There have also been advances made in the engineering of devices necessary to reliably produce SAW atomization at lower input powers.

It was posited early on that the mechanism of droplet production was somehow linked to capillary waves on the free surface of the fluid. In 1962, Lang used a piezoelectric transducer to induce acoustic waves in thin films and bulk, contained fluids.[201] He was able to show a link between capillary wavelength, λ_c and droplet size by varying the applied piezoelectric excitation frequency, f. In Kelvin's equation $\lambda_c^3 = 2\pi\gamma/\rho_f f_c$, λ_c is dependent on the capillary wave frequency, f_c. Lang assumed that f_c was equal to $f/2$ based on work by Faraday and others[202–204] and found that the capillary waves followed this modified Kelvin's equation and that the median drop diameter was a constant factor, 0.34, of λ_c when f was between 10–800 kHz. It is important to note that these experiments were not done using SAW and sessile drops and that the capillary wave observation was done at a different acoustic amplitude than the droplet production and sizing.

Kurosawa *et al.* created the first SAW atomization devices much later[205,206] but used the same modification of Kelvin's equation to predict the resulting droplet size—they used $f/2$ in place of f_c and allowed for an empirical fitting constant. However, the fitting constant they found was 3.8 rather than 0.34. They suggested that the difference was due to the large surface vibration amplitudes in their study compared to those in Lang *et al.* but another important consideration is that they used 10–40 MHz acoustic waves as opposed to 10–800 kHz. Many ideas later investigated more rigorously were mentioned by Kurosawa *et al.* They noticed that atomization occurred more readily from a thin film than from a drop, the atomization rate increased linearly with input power above an initial threshold and then reached a maximum, and the resulting droplet size distribution had multiple peaks.

More than 10 years later, Qi *et al.*[207] confirmed the involvement of capillary waves in mechanisms of atomization. Qi used LDV to determine the frequencies of both acoustic waves in the substrate and capillary waves in the free surface of the drop. The size of the resulting droplets was measured using an aerodynamic particle spectrometer. The authors showed that the correct frequency to use in Kelvin's equation for droplet size prediction is in fact f_c and they defined equations for this frequency dependent on the the mechanism at play. If internal viscous damping dominates then Eqn. 8 holds, but if inertial forcing dominates then Eqn. 9 holds.

$$f_c \sim \frac{\gamma}{\mu R} \tag{8}$$

$$f_c \sim \left(\frac{\gamma}{\rho_f R^3}\right)^{1/2} \tag{9}$$

They determined experimentally and numerically that Eqn. 8 applies in drops while Eqn. 9 applies in thin films near the viscous boundary layer thickness, $\delta = (\mu/\rho_f 2\pi f)^{1/2}$. They were able to predict the droplet size to reasonable accuracy in both glycerol and water in both the drop and thin film geometries. In drops, they observed at least two distinct mechanisms of droplet production corresponding to two distinct sizes. The drop deformed asymmetrically about the Rayleigh angle (as observed in translation studies by Brunet and others in the field) forming a wave crest that pinched off during a whipping motion producing a large droplet. Smaller droplets were produced from axi-symmetric, roughly cylindrical jets with diameter $\sim \lambda_c$.

In their numerical work they defined an acoustic capillary number,

$$C_a = \frac{\rho_f (2\pi f)^2 A^2 L \cos^2(\theta_R)}{\varepsilon\gamma}, \tag{10}$$

that describes the ratio of applied acoustic stress to capillary stress, where A is the SAW amplitude, and ε is the aspect ratio (height over length (H/L), which is assumed to be small for thin films). They predicted a critical acoustic capillary number, through fluid dynamic numerical simulation, above which the surface will destabilize and produce atomized droplets. Their critical number was close to the value at which an inflection in the interfacial energy vs time graph occurs (*see* Fig. 25). It seems clear that the droplet size depends on the capillary wave frequency while the onset of atomization that produces said droplets may be predicted by the capillary number. Much more work is needed to test this and other methods of predicting the onset of atomization.

Qi *et al.*[207] observed a broadband low-frequency response in the free surface of the fluid, but did not investigate the effect of substrate displacement amplitude on this response. Tan *et al.*[208] explored this topic by performing similar experiments at multiple amplitudes and performing a more complex numerical simulation. They introduced an acoustic Reynolds number,

$$\mathrm{Re}_a = \frac{\rho_f u_1 \lambda_f}{2\pi(\mu' + 4\mu/3)}, \tag{11}$$

to distinguish between the fast streaming, high amplitude regime ($\mathrm{Re}_a > 1$) and the slow streaming, low amplitude regime ($\mathrm{Re}_a <$ 1). In Eqn. 11, u_1 is the first order fluid velocity and λ_f is the wavelength of sound in the fluid. They used the successive approximation method, which limited their numerical results to the low amplitude regime where nonlinear effects are small. However, they were able to show that, in this regime, the capillary wave response has a fundamental resonance frequency equal to f plus additional superharmonics. The amplitude of the free surface vibrations also was comparable to that of SAW in the substrate. They were able to investigate the high amplitude regime with experiments and found that the f_c response was broadband and reached orders of magnitude lower frequencies than f. No hint of the $f/2$ subharmonic Faraday response was found. They also determined that in thin films irradiated by TSAW the capillary wavelength is related to λ_{SAW}, but in drops irradiated by SSAW it corresponds to λ_f.

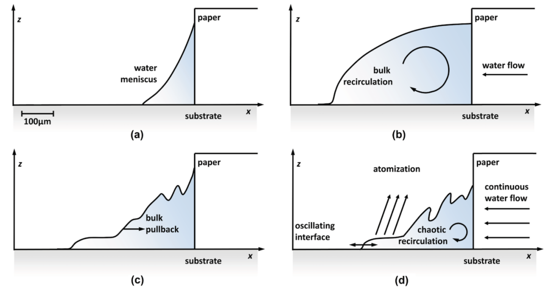

Fig. 26 Dynamic behavior of fluid supplied via a paper wick to a TSAW source. (a) Before application of TSAW. (b)Bulk liquid is drawn out by initial surface vibrations. (c) After a transient, the bulk retreats back into the wick leaving a thin film of quasisteady geometry estimated by Collins. (d) Atomization occurs from the thin film, which competes with and is periodically obscured by the bulk. Reprinted figure with permission.[209] Copyright (2012) by the American Physical Society.

Building on both the thin-film transport work described in Section 4.2.3 and the advances in droplet size prediction just described, a paper by Collins *et al.*[209] further strengthened the case for atomization from thin films. They investigated the dynamics of thin-films of water drawn from a paper wick onto a LN substrate (their observations are illustrated in Fig. 26). They theorized that the height of the thin-film produced during TSAW actuation depends on acoustic resonance modes and can be estimated by a balance between acoustic radiation intensity and capillary stress. Local energy minima occur at $h = n\lambda_f \cos(\theta_R)/8$ ($n = 1, 3, 5...$) according to this theory and they found the experimental value in this case to be $h = 7\lambda_f \cos(\theta_R)/8$. They also produced numerical results predicting the length and height of the films based on including radiation pressure and streaming in the Navier-Stokes equations. These results showed a dependence of the film length on an acoustic Weber number $\mathrm{We}_a = \rho A^2 \omega^2 L/\varepsilon\gamma$. This lead to an adjustment to the droplet size prediction based on the instability wavelength established by Qi *et al.* in 2008[207] yielding,

$$D \sim \frac{\gamma H^2}{\mu L^2} \frac{We_a^{2/3}}{f}, \tag{12}$$

where L is the lateral dimension of the fluid volume (parallel with the substrate) and H is the vertical dimension of the fluid volume.

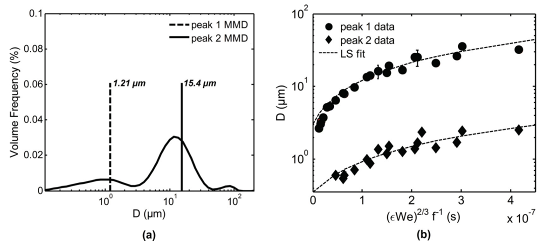

Fig. 27 (a) Distribution of drop sizes during atomization from a thin film in an experiment using 22 MHz SAW at 5.2 W. The two highlighted peaks represent drops that were observed to originate from the thin film, while the third peak at the far right originated in the bulk fluid. Distributions at other frequencies and powers were qualitatively similar. (b) A graph of the drop diameter vs $(\varepsilon \mathrm{We}_a^{1/3})^2 f^{-1}$ for the two thin film peaks highlighted in (a). Noting that the y-axis is a log scale, this agreement verifies the validity of eqn. (12). Reprinted figure with permission.[209] Copyright (2012) by the American Physical Society.

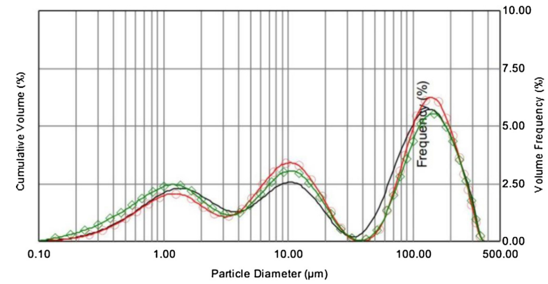

Fig. 28 Trimodal distribution of droplet sizes during atomization from a sessile drop at 4.2 W and 20 MHz (each curve represents a separate trial). Notice which peak dominates in this distribution from Wang compared to the distribution from Collins in Fig. 27. Reprinted[195] with permission from Elsevier.

They confirmed the validity of Equ. 12 in experiments at a range of SAW power and frequency (*see* Fig. 27b) and obtained the well-known trimodal distribution as seen in Fig. 27a.

Recently, Wang *et al.*[195] confirmed that droplet size is more correctly predicted by the mechanism dependent capillary stress balance put forth by Qi *et al.* leading to eqn. (12), than by the modification of Kelvin's equation put forth by Lang. Similar to Tan *et al.*,[208] they experimented with a single 20 MHz device while varying the applied power, which is proportional to the substrate displacement amplitude. At high power they observed the trimodal distribution, but in this study of sessile drops, the largest volume contribution was from the largest droplets (*see* Fig. 28) whereas the middle mode was largest in the above study of thin films.

The authors were able to record the atomization process over time with high speed video. This further revealed that the largest drops occur first followed by the medium drops and finally, after most of the original drop volume was removed, the smallest droplets. Qi *et al.*, they emphasize that the fluid geometry and length scale largely determine the atomization mechanism. Their paper claims that each peak in the size distribution corresponds to a distinct mechanism, which in turn corresponds to a distinct geometry/scale. Large drops are produced from acoustic radiation pressure on the fluid interface leading to extension, whipping, and pinch off, medium drops from capillary waves due to Eckart streaming in the bulk, and small drops from capillary waves due to Schlichting streaming in the viscous boundary layer. However, no evidence is offered beyond video observation that these are the specific mechanisms at play. They conclude that drops cannot be atomized without jetting occurring first to decrease the height of the fluid geometry, but we have already seen that the distribution in droplet size can be shifted towards the smaller modes in thin films. Further control of fluid geometry may allow even better mode selection.

Relatively high power is required for atomization, but (as was common with translation) modulation of the input signal can reduce the power requirement. In a 2014 paper by Rajapaksa *et al.*[210], amplitude modulation, rather than pulse width modulation as used by Kurosawa *et al.*[205], was demonstrated to reduce the input power while maintaining relatively high atomization rate, small droplets, and a narrow size distribution. This concept takes advantage of the difference in time scale between the hydrodynamic fluid response and the acoustic forcing. The modulation frequency was chosen to avoid damage to biological particles, which they also demonstrated in the paper, so that it could be used in applications. Droplet size was seen to increase with input power as expected based on eqn. (12). However, size also changed based on the frequency of modulation with a peak at 1 kHz. More work is needed to clearly explain this dependence. At the power demonstrated, 1.5 W, devices could be powered by small batteries so that they can be miniaturized as has been desired for SAW microfluidics for some time.

Another path to more efficient atomization has been suggested in a recent paper by Rezk *et al.*[211] Hybrid acoustic waves with bulk and surface components may prove to be synergistic in contrast to the current understanding of Lamb waves as spurious in SAW devices. However, this concept has not yet been convincingly demonstrated.

It is known that the excitation frequency of a SAW device, f_{SAW}, does not change the substrate particle velocity, but recently f_{SAW} has been shown to affect other aspects of sessile drop manipulation. In a paper by Dentry *et al.*, the authors modify Lighthill's turbulent jet model to allow its successful application to low excitation powers and explain the effects of frequency variation between 20–946 MHz on acoustic streaming velocity and distribution.[98] Their modification[126] included a finite source of acoustic energy and replaced turbulent dissipation with viscous dissipation. Experimentation with SAW devices fabricated with a range of resonant frequencies agreed well with this theoretical model. The maximum streaming velocity as well as the distance from the source at which this maximum occurred were recorded with the aid of fluorescent particles as the input power was varied. The maximum velocity increased with power, but the beam shape was independent of power. They emphasized the importance of the attenuation length of the acoustic beam in the fluid, β^{-1}, on streaming. They found that β^{-1} decreased with increasing frequency, thus increasing the power density within the beam. From this the authors deduced that the streaming velocity is proportional

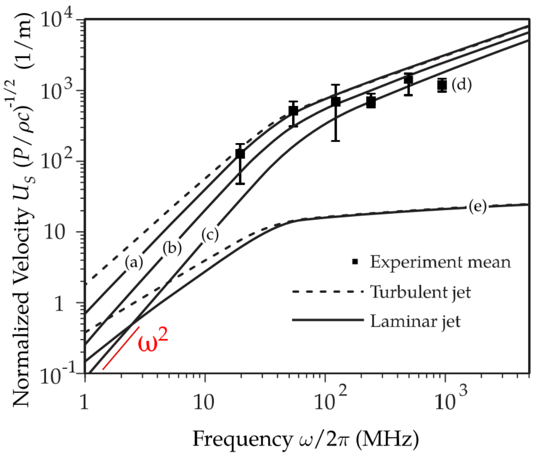

Fig. 29 Streaming velocity versus applied frequency. In Dentry's laminar jet model (solid curve): at low frequency, streaming velocity increases with the square of the frequency, but at high frequency, it increases with the square root. As beam power is decreased at a fixed frequency ((a) 10 mW, (b) 1 mW, (c) 0.1 mW) the streaming velocity is reduced. Experimental values (square dots) agreed fairly well with both models (Lighhill's turbulent jet model in dashed curve). (d) Indicates a lower than expected experimental data point at 936 MHz due to practical limitations (velocity could not be measured at its peak location). (e) Indicates an alternate normalization of the 10 mW data incorporating the frequency-dependent source area. Reprinted figure with permission.[98] Copyright (2014) by the American Physical Society.

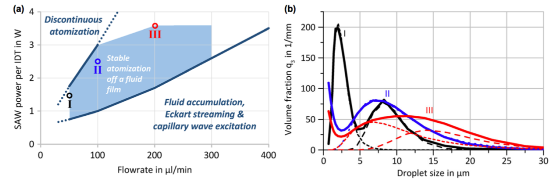

Fig. 30 (a) An experimentally determined stability graph where a high power to flow-rate ratio leads to occasional dry-out and a low ratio leads to accumulation of fluid. (b) Droplet size distributions corresponding to points indicated on the stability graph show that droplet size can be tuned by changing the power and flow-rate while maintaining their ratio within the stable region. Reprinted from Winkler *et al.*[95]

to frequency squared. They pointed out that when normalized for the frequency-dependent source area (dependent on attenuation of SAW in the substrate), there were two distinct regimes(*see* Fig. 29). At low frequency, streaming velocity increases with the square of the frequency as they originally deduced, but at high frequency, it increases with the square root. The practical upshot of this finding is that, above 100 MHz, increased frequency gives diminishing returns in streaming velocity and thus must be balanced with the fabrication costs of such devices.

The delivery of fluid to the substrate is vital to produce continuous atomization. Also, in light of the above work showing the dependence of droplet size, distribution, and the onset of atomization on the geometry of the sessile drop, fluid delivery becomes even more important. In a 2015 paper, Winkler *et al.*[212] suggested that the best way to produce reliable atomization devices at manufacturing scale was to supply the fluid to the SAW in the form of a thin film at the periphery of the acoustic beam. This strategy avoids the complexities of Eckart streaming in favor of Schlichting streaming within the boundary layer, which as described above produces more reliable atomization. It also removes potentially damping structures from the acoustic beam path as the film is drawn into the path by the mechanism explained earlier by Rezk *et al.*[181] However, we note that the damping issue can be mitigated by using more rigid structures bonded with a UV-epoxy as demonstrated by Langelier *et al.*[125]

Winkler claims that this fluid supply approach avoids the jetting regime before the onset of atomization. It is accomplished by fabricating a microchannel from SU-8, a common photoresist used in microfabrication, adjacent to the beam. This avoids the uncertainty of a wick or capillary, which imposes non-thin-film fluid boundary conditions (as was observed by Collins and evident in Fig. 26). It is an improvement upon the idea of a capillary slit originally used by Kurosawa.[58,205]

In experiments with SSAW from 65 MHz IDTs, Winkler *et al.* showed that droplet size increased with fluid supply rate, since it is related to the height of the film, in agreement with eqn. (12). In these devices, as opposed to those used by Wang *et al.*[195], they found that large drops only weakly contributed to volume removal. This indicates that they successfully avoided jetting in favor of atomization. The middle peak of the three mode droplet size distribution dominated the volume removal and increasingly so at higher supply rates. This agrees with the claim that Eckart streaming produces the medium size droplets while Schlichting streaming produces the smallest droplets. Peak locations were at the same order of magnitude between distributions obtained by Collins,[209] Winkler,[212] and Wang.[195] This agreement suggests that there is some consistent set of mechanisms at play in SAW atomization.

Building on the 2015 paper describing an SU-8 microchannel fluid supply system, Winkler *et al.*[95] studied the effect of various placements of the channel outlet as well as the flow rate in SSAW devices. The best atomization behavior was observed when the fluid was supplied just outside the aperture of the SSAW region. Any closer and the effect of the microchannel's presence within the acoustic beam becomes large and farther away the fluid geometry is less controllable. They determined that the stability of continuous atomization is critically dependent on the ratio of power to flow-rate (*see* Fig. 30). On the other hand, they showed that the resulting drop size could be tuned within a single device by choosing the power, which corresponds with the work by Collins to incorporate We_a into the equation for drop size prediction. Importantly, they were able to achieve atomization without initial oscillation and jetting due to the precise nature of the fluid supply system.

Viscosity is another important parameter that has recently been investigated in more detail. In a 2015 paper, Guo *et al.*[64] varied the glycerol content in droplets atomized from ZnO/Si SSAW devices designed for frequencies 12–65 MHz. Though ZnO requires higher powers, the effect of viscosity should be analogous in LN devices. They observed the same sequence of stages leading to atomization and the three mode droplet size distribution described in many of the above experiments. They also note that droplet size decreased with increasing excitation frequency, but at the cost of increased power required for onset of atomization. The highest frequency devices, requiring the highest power, also tended to produce more jetting before the onset of atomization. Unsurprisingly an increase in viscosity required a large increase in input power to achieve atomization at a given frequency. Additionally, at a certain viscosity, atomization could not be achieved even with increased power. As the frequency was increased the maximum atomizable viscosity decreased.

The authors pointed to increased viscous damping of acoustic energy leading to reduced streaming velocity, but offered no detailed explanation of the observed behavior. Curiously, the authors retained a fudge factor and used the excitation frequency as opposed to f_c in calculating droplet size though they sited Qi *et al.*[207] However, the measured values agreed reasonably well with calculated values leading to the conclusion that their fudge factor was appropriate for this frequency range.

A similar study was done by Winkler *et al.* more recently with LN SSAW devices in the 40–120 MHz range.[213] Fluid was supplied at the edge of the acoustic beam path of a SSAW by a capillary tube and syringe pump. They found the standard trimodal droplet size distribution at low viscosity, while as viscosity is increased the distribution accumulates to a single peak. They suggested that this effect was due to the limited ability for secondary and tertiary vibration modes to generate droplets at high fluid viscosity. They also observed that the dominant peak moved to smaller droplet sizes and itself became narrower (more monodisperse) as viscosity was increased. Additionally they found that increased viscosity reduced the range of frequencies at which the fluid could be atomized, as well as the atomization rate, and the height reached by the resulting mist. Again, no detailed mechanistic explanation was offered for the observed phenomena suggesting that more work is needed.

Some critical advances in applications have been enabled due to the above progress in acoustofluidic atomization.

Evaporation-induced self-assembly (EISA) is an important nanofabrication technique first introduced by Brinker *et al.* in 1999.[214] Friend *et al.* demonstrated that SAW atomization could be used to produce nanoparticles (from a PCL acetone solution in this case) by EISA.[215] Particle aggregates of 150–200 nm were formed in each droplet atomized from the fluid/air interface and were collected in a container filled with surfactant solution. The size of particle aggregates was largely determined by the volume of PCL contained in each droplet. Transmission electron microscopy (TEM) images revealed that each aggregate was composed of many 5–10 nm particles. Friend *et al.* suggested that these formed due to spatial non-uniformities at the evaporation surface leading to phase separation and nucleation (similar processes have been demonstrated[216,217]). The particle size was correctly predicted via Gibbs free energy minimization thus validating this suggestion. The advantage of using SAW for this application is that the particle aggregate size can be tunned by the frequency of the device since frequency controls droplet size in SAW atomization. Additionally many other solvent-solute combinations can be used to create other kinds of nanoparticles. Large molecules or other compounds could also be encapsulated within the particles.

SAW in conjunction with electrostatic deposition has been developed to fabricate thin films and coatings, but this technology requires high frequency and power to atomize high density solutions or those with strong inter-particle bonding. A recent paper by Choi *et al.* integrated electrohydrodynamic atomization (EHDA) with SAW to accomplish atomization of these solutions at lower frequency and power.[218] The authors were able to produce sub-micron size droplets that were unprecedented with EDHA alone without exceeding the operating frequency that would be required for atomization of these fluids by SAW alone (20 MHz). The reduction in frequency of the SAW device was made possible because fluid was supplied to the SAW as small droplets (on the order of 1 μm) rather than as large 1 mm order drops. The authors confirmed the usefulness of the technique by depositing high quality ZnO and two conductive polymers as well as fabricating a high performance humidity sensor.

Solution deposition of lanthanum and zirconium on nickel tungsten substrates is a common method of producing superconducting thin films, but current mechanisms of spraying the solutions require mechanical parts and nozzles and lack a tight size distribution with small droplet sizes. A recent paper by Kirchner *et al.* proposed to replace these methods with SAW atomization.[219] One of two buffer solutions (either water or propionic acid based) was applied using SAW atomization followed by a typical heat treatment to produce the desired superconducting thin film layer. The resulting films were highly crystalline, homogeneous, and dense, but suffered discontinuities due to poor surface wetting and/or uneven evaporation. This application is therefore promising but requires further work.

Vuong *et al.* presented a possible replacement technology for pipette tips.[220] Pipettes are often inaccurate due to the adhesive forces between the liquid and the tip, especially in the case of depositing liquid onto superhydrophobic surfaces. In this paper, the fluid was instead atomized into a container with a hydrophobic internal surface. The amount of dispensed fluid was precisely weighed before being perturbed in the container to form it into a single drop. The volume of the resulting drops was linear with the operation time of the atomization device.

SAW atomization can also be used to cool a surface by distributing sub-micron size droplets of an evaporative fluid as demonstrated by Ang *et al.*[221] SAW technology is well suited to compact electronic device cooling since it can be miniaturized and provides enhanced heat flux removal due to smaller droplets and thus quicker vaporization. This nozzleless technique also limits the chance of device failure due to clogging, which is common in various nozzle based atomizers. In this paper, cooling was also enhanced by an optimized concentration of copper oxide nanopowder, which lead to increased surface area once deposited on the surface to be cooled thereby allowing greater outward heat flux.

Nebulization provides a quick, non-invasive method for drug delivery with mild, limited side effects. Alvarez, Friend, and Yeo first described a method of generating monodisperse aerosols via SAW atomization for drug delivery.[222] They demonstrated insulin aerosols of 3 μm diameter, within the size range known to be optimal for absorption into the lungs. The technique was shown to be effective (80% delivery efficiency) in delivering a model asthma drug to a twin-stage impinger lung model.[223] SAW nebulization has also been shown to be compatible with an antibody treatment[224] and a plasmid DNA vaccine.[225] Paper represented a cheap and generic carrier for such bio-fluids and SAW atomization has been shown to work well with fluid laden paper samples.[226]

The detection of bio-molecules can be enhanced by the integration of SAW nebulization. Heron *et al.*[227] used SAW to nebulize peptide solutions and demonstrated that mass spectroscopy (MS) performed on the resulting ions provided similar results to matrix assisted laser desorption ionization (MALDI) and electrospray ionization (ESI) depending on the mode of operation of the SAW device. Yet, this device still required a high voltage between the substrate and the MS inlet. Ho *et al.*[228] developed a device without this requirement by utilizing the surface electric field present on all SAW devices. Huang showed that SAW nebulization produces ions with lower internal energy (vital for MS) than does ESI[229] and later improved the performance (higher ion intensity) of a mass spectrometer by incorporating two SAW IDTs to produce smaller, more monodisperse droplets at a higher volumetric flow rate than their previous design.[230] The ion intensity produced by ESI is still typically higher than that produced by this double-IDT SAW device, but there are fewer limits on the samples and no high-voltage source as is required for electrospray.

4.2.6 Bio-sensors

In the last thirty years, SAW devices have been widely used to develop fast and sensitive bio-sensors for detecting pathogens, cells, and bio-molecules. Similar to devices used for communication, SAW sensors are comprised of a pair of IDTs. One generates a SAW while the other identifies changes in the SAW signal produced in the intervening space. The target under investigation is immobilized between output and input IDTs and this area is called the interaction region. Differences in the frequency, velocity, phase, and amplitude between the input and output SAW reveal the density and mechanical properties of the target.

The primary metric of bio-sensor performance is sensitivity so the large attenuation that occurs when Rayleigh SAW encounter a fluid initially precluded SAW bio-sensors. Other modes that are more compatible with a fluid environment, which is often required for biological samples, have been explored. Among them are: shear horizontal surface waves (SH-SAW), surface transverse waves (STW), and Love waves (LW). This topic and other early work in biosensing has already been well covered in reviews by Lange and Rapp[231] and by Rocha-Gaso *et al.*[232] Here we will introduce some representative applications that are related to SAW bio-sensors.

Pathogens and cells can be bonded to the interaction region directly for detection. Howe and Harding studied *Escherichia coli* (*E. coli*) and *Legionella* by attaching specimens directly onto the surface of a SAW device.[233] The bacteria were exposed to an antibody at pH 4.0, which is close to their isoelectric point. After that, antibodies for *E. coli* or a combination of antibodies for both *E. coli* and *Legoinella* were added and bound to the bacteria on the surface. Significant differences in frequency were observed confirming the ability to detect (*E. coli*) and *Legoinella* with sensitivity of 10^6 cells per milliliter. Compared to other bacterial detection techniques, the use of SAW is both sensitive and fast–the process can be completed within 3 hours. Instead of Love waves adopted in Howe and Harding's work, SH-SAW is used by Berkenpas to detect bacteria bonded to the surface of the SH-SAW device.[234] Both measurement setups with pathogens immersed in flow and a "dip-and-dry" method are used in the experiments.

Baca *et al.*[235] reported a method to rapidly detect the Ebola virus in 2015. Antibodies were functionalized on the surface of a SAW biosensor with Ebola antibodies in the test lane and a control group of antibodies in the preference lane. The phase signal was recorded and compared between these lanes. A phase shift was observed caused by bioagents immobilized on the antibody.

Other than detection of mass increase caused by bonding between cells and specific antibodies on the surface, mechanical properties are also used as biomarkers in SAW bio-sensors for cell detection and analysis. In 2016, Senveli *et al.*[236] found that stiffness measured at high frequency was a potential biomarker for tumor cells. They reported a method for sensing tumor cells via microcavity coupled SAW devices. Cells were trapped in microcavities fabricated on the substrate of the SAW device. Based on the difference of ultrasound velocity between cells and substrate, the phase changes of SAW were measured thus revealing the elastic modulus of the cells. They were able to differentiate between certain types of tumor cells based on these measurements of elastic modulus. This technique and others like it may be beneficial for cancer diagnosis and possibly for future rapid cancer screening assays.

In addition to the organisms themselves, bio-molecules such as protein, sugar and DNA from target cells and pathogens can also be trapped on the surface of the sensors and detected. Take DNA detection as an example, many of the DNA detection approaches need DNA segments to be amplified (PCR for example) which requires long time while SAW bio-sensors provide a possible way to detect DNA target with high sensitivity. In 2007, Sakong *et al.*[237] developed a SH-SAW-based sensor system with micro-fluidic channels to detect oligonucleotide DNA. DNA with a thiol group was used as a probe and immobilized on a gold coated interaction region. A frequency shift was observed when the target DNA was continuously flowed over the probe DNA layer. They showed that this method has sensitivity up to 135 pg/(mℓ·Hz). In 2015, Cai *et al.*[238] proposed a method to detect DNA using a third-order harmonic mode (6.4 GHz) upon a SAW device fabricated on LN substrate. This higher order mode achieves atomic resolution and makes it possible to sense a single DNA base with a SAW bio-sensor.

Biosensor signals can also be amplified by bonding biomolecules to larger particles. Lee *et al.*[239] presented a SH-SAW immunosensor that was able to simultaneously detect multiple cardiac makers (cardiac troponin (cTnI), creatine kinase (CK)-MB, and myoglobin) with high sensitivity in human serum. Antibodies were conjugated with gold nanoparticles (AuNPs) in advance to enhance the signal and then used to capture analytes. Finally the antibodies were immobilized on the sensing area between two IDTs. The SAW signal was observed to change with the concentration of conjugated antibodies that were bounded to the surface. Minimum detectable concentrations of cardiac markers were reported as 20 pg/mL, 1.1 ng/mL, and 16.0 ng/mL for cTnI, CK-MB, and myoglobin, respectively with a 200 MHz device. The author also verified that higher mass sensitivity could be achieved by increasing the operating frequency of the SAW device.

4.3 Fluid Manipulation in Closed Channels

We have discussed fluid manipulation in sessile drops, but, at the time of this writing, microfluidic processes necessary for lab-on-chip applications are more commonly accomplished in channels. This is likely due to the relative ease of fabrication of microfluidic chips based on channels and the lack of evaporation. Continuous flow in a microchannel can provide rapid and high-throughput flow manipulation and analysis of a variety of samples. Closed channels also reduce contamination from the surrounding environment during the analysis.

PDMS is widely used to form microfluidic channels. However, there are two major, well-known issues with this material in the context of acoustic waves: heating [240] and attenuation, [241] though each can be controlled and mitigated. In what follows, some researchers choose to accept these drawbacks due to the ease of fabrication, but alternatives like glass or milling directly into LN are available.

4.3.1 Fluid mixing

Mixing is essential for chemical reactions and the promise of miniaturized bio-chemical processes requires chemical reactions. However, at the scales of channel based microfluidics and nanofluidics, extremely low Reynolds numbers make the flow laminar and difficult to effectively mix. In the absence of turbulence, diffusion-based mixing cannot meet the requirements for most chemical mixing in microfluidic applications. In acoustofluidic systems, the nonlinear average effects of acoustics such as acoustic streaming are able to create a net streaming flow in the fluid, and thus will cause rapid and effective mixing. In light of this advantage, applications of rapid and active mixing have recently been developed and demonstrated in acoustofluidic research.

Following the progress made by the rest of the Wixforth group in drop translation, Sritharan *et al.* [242] also demonstrated SAW-induced mixing in a simple Y-shaped microfluidic chip with two inlets for dissimilar fluids, which were mixed in the third channel. An acoustic wave generated by a SAW device was coupled through the bottom of the chip and was diffracted based on the chip material (silicon, glass, polymer, etc). This is a prime example of an extra capability provided by acoustofluidics beyond those available to conventional microfluidics, powered by external pumps. In very similar devices, Tseng *et al.* [243] compared the mixing efficiency between channels oriented parallel to wave propagation (parallel-type) and those oriented perpendicular to wave propagation (transverse-type). They showed that the parallel-type mixer was more effective and that higher voltages were associated with better mixing. Jo and Guldiken [244] showed that, in the specific case of transverse-type micro-mixers, SSAW was more efficient for mixing than TSAW. Furthermore, Luong *et al.* [245] reported that, as in sessile drop translation and particle concentration, FIDTs offered greater efficiency than straight IDTs.

The effect of the channel geometry on acoustic mixing has also been investigated. In parallel-type microchannel mixers, Tan *et al.* [246] noted that a uniform channel flow became a mixing flow when the channel width was larger than the wavelength of the sound in the fluid. This finding suggests the possibility of dynamically choosing between flow and mixing in a single device by controlling the input frequency of the SAW device. Conversely, Miansari and Friend [75] presented active mixing via SAW in nanoslits (nanoscale channel height but width $> 100\ \mu$m). Mixing tended to occur with vortices aligned in the plane of the transducer rather than the typical vortices perpendicular to this plane. The authors suggest that sound waves cannot travel in the fluid due to it's nanoscale height and thus the typical acoustic streaming that causes mixing does not occur. More work is needed to understand nanoscale confinement in the context of fluid/acoustic wave interaction. We will present other aspects of this paper and others dealing with nanofluidics later in this review.

Acoustic mixing not only occurs in channels and sessile drops, but Rezk *et al.* [247] also presented a uniform mixing method in a simple paper-based microfluidic device using SAW, offering a low-cost and disposable alternative to microchannel mixing. This technique could be especially relevant to diagnostics and other biological testing.

Other modes of acoustic vibration besides SAW have been used for mixing. Piezoelectric elements can produce a large variety of fluid motions in channels and chambers because they can be driven in several different vibrational modes. Among them, the thickness-mode is widely used for active mixing due to large amplitude substrate displacements in this mode. Thickness-mode devices have been used at a range of frequencies in the literature. Rife *et al.* presented mixing in an isolated PMMA chamber (a thin square box) via 50 MHz actuation of two $BaTiO_3$ transducers, but suggested improvements in mixing through larger frequencies and more or larger transducers. [248] Yang *et al.* investigated a very similar glass mixing chamber, but included inlet and outlet ports and chose PZT transducers. [249] Their device proved the concept, but was slow (2 seconds to reach stable mixing), high power (operated at 50-90V), and unsuitable for many applications due to the use of PZT (driving frequencies of 15-100kHz caused fluid heating and cavitation, which are each harmful to many bio-medically relevant fluids). Yaralioglu *et al.* applied a similar idea to perpendicular mixing in a PDMS microchannel using zinc oxide transducers at 450 MHz [250] (*see* Fig. 31). They were able to produce turbulent flow across a 300 μm channel at up to 60 μL/min and while using a much lower voltage than Yang, 1.2 V (30mW of power). They experienced minimal heating partly due to low power actuation and partly due to the continuous flow carrying away heat. Up to this point the location of the mixing was determined by the transducers, but Oberti *et al.* [251] used a large transducer at a much lower frequency (100 Hz) to vibrate the entire device while selecting the location of mixing via a T-junction. The authors did a careful and detailed analysis and determined that the sharp edges of the T-junction caused vortices in the flow that lead to mixing. Phan *et al.* also utilized geomet-

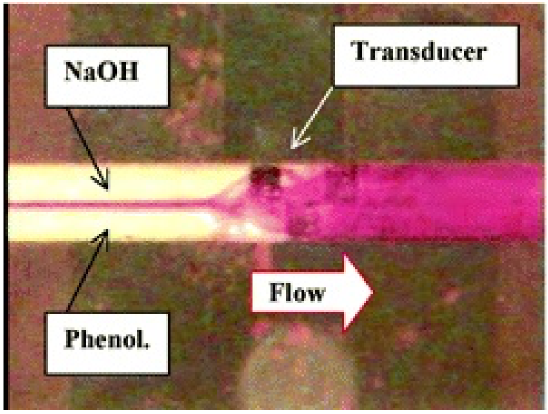

Fig. 31 Laminar flow before the transducer (left side) and mixing flow after the transducer (right side) with an embedded piezoelectric transducer. A strong acoustic streaming effect is produced for more active and rapid mixing. Reprinted with permission from Yaralioglu *et al.* [250]. Copyright (2004) American Chemical Society.

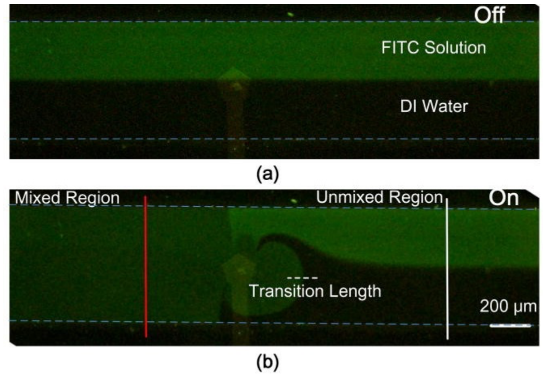

Fig. 32 (a) Laminar flow and no mixing effect in the absence of acoustic waves. (b) Fast and uniform mixing of water and fluorescent dye in the presence of high frequency SAW within 1 ms. Reprint permis. Cui (2016). [253]

ric features in a channel to change the boundary conditions of the flow in order to produce turbulent flow. [252] They fabricated a microscale silicon nitride membrane with a hole etched through it, which was bonded to the bottom of a Y-channel, that generated strong streaming vortices for fast and homogeneous mixing. At the opposite end of the frequency spectrum, 1.54 GHz was utilized by Cui *et al.* [253] to achieve rapid (within 1 ms) and homogeneous mixing in a y-channel without geometric features (*see* Fig. 32).

Catarino *et al.* compared experimental mixing performance in a T-junction microchannel during flow with numerical analysis on an equivalent system. [254] The distance long the channel required to achieve mixing was measured for pure diffusion and then with acoustic assistance under various flow rates. Their results revealed a moderate reduction in this distance with acoustic assistance from a β-poly(vinylidene fluoride) transducer operated at 40 MHz and 24 V. Their numerical results mirrored the moderate improvement seen in experiment though the absolute value of the mixing distance was only within an order of magnitude. Similar simulations could be used to gauge the impact of adding acoustofluidic mixers to other microfluidic systems (the authors emphasized diagnostic applications).

The mixing performance of acoustic-based micromixers has been further improved via acoustically driven bubbles. The vibration of a bubble membrane induced by acoustic waves can cause acoustic streaming [255,256] and results in a more prominent perturbation of the surrounding fluids than streaming from direct interaction with the substrate. This method can perform effective and rapid mixing at relatively low frequencies, which greatly alleviates the temperature rise in the system during acoustic-based mixing. We will not cover acoustic cavitation in microchannels as this topic has been systematically reviewed by Ohl. [257]

Liu *et al.* [258,259] used a piezoelectric PZT disk to excite air bubbles trapped in the top layer of a chamber. This resulted in complete mixing within 6 seconds using a 40 V_{pp} (peak-to-peak voltage) excitation. Tovar *et al.* [260] and Ahmed *et al.* [261] both designed lateral cavity acoustic transducers (LCATs), microchannels with perpendicular cavities patterned along two sides of the channels (*see* Fig. 33 for Tovar's design). Air bubbles are trapped automatically in the cavities when liquid flows through the channel. As a result, these devices are capable of mixing fluids by induced vibration of the fluid/air interface. Wang *et al.*, [262] Ahmed *et al.*, [263] Ozcelik *et al.*, [264] and Bertin *et al.* [265] each trapped air bubbles in a microchannel either by designing the channel geometry or by adding structures in the channel to perform oscillating bubble-induced mixing. The work by Ahmed *et al.* appears in Fig. 34. In order to reduce the common problem of bubble leakage, which results in shrinking and poor vibration efficiency, [266] continuously pumped nitrogen into a microchannel thereby refilling or replacing leaky bubbles.

Combriat *et al.* [267] investigated the flow generated from the pulsating bubbles submitted to an external flow in microfluidic channel. Bubbles with radii between 20 and 50 μm were generated and squeezed in the observation channel (2 mm wide, 25 μm high) and micropits were designed on the upper wall of the channel to trap the bubbles. A high speed camera was used to record the flows visualized by tracer particles for quantification. Closed recirculation zones that isolate a part of the flow around bubbles were observed in the experiments. These zones can be used to enhance mixing in the fluid, and the position and size of these zones can be changed to manipulate the mixing condition. It was found that closed recirculation zones are upstream when external flow is applied along the bubble pair direction and downstream when bubbles are perpendicular to the external flow. The size of the closed recirculation zones can be changed by adjusting the external flow rate.

Although bubble-based micromixers are capable of rapid and homogeneous mixing, their disadvantages include bubble instability [263,269] and inconvenient bubble-trapping processes. As an alternative, Huang *et al.* [268] designed sidewall microstructures known as *sharp edges*. The oscillation of these sharp edges induced by PZT transducers causes acoustic streaming, facilitating rapid and homogeneous micromixing (*see* Fig. 35). Numerical studies of the acoustic streaming that occurs near these sharp edges have been presented by Ovchinnikov *et al.* [270] and Nama *et al.* [271]

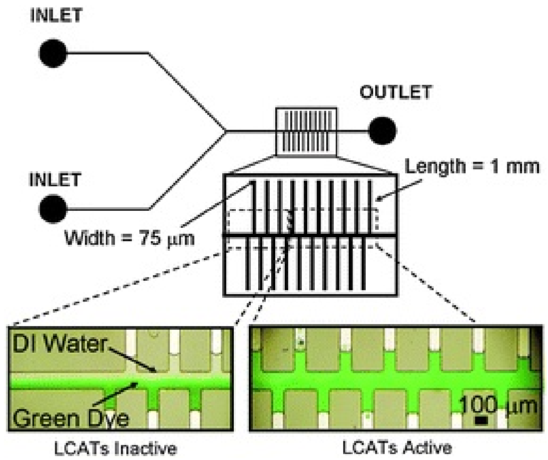

Fig. 33 Lateral cavity acoustic transducer (LCATs) induced fluid mixing in a channel. The vibration of air-liquid interface caused acoustic streaming in the channel and performed uniform and rapid mixing. Reproduced[260] with permission from The Royal Society of Chemistry.

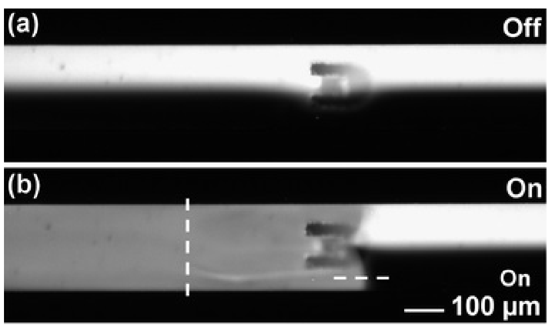

Fig. 34 (a) No mixing effect in absence of acoustic waves. (b) uniform mixing of water and fluorescent dye in presence of acoustic waves. Reproduced[263] with permission from The Royal Society of Chemistry.

4.3.2 Fluid pumping

One of the key problems in lab-on-a-chip devices is the ability to provide effective fluid flow against a resistance in a chip-sized device. We now examine several approaches to this problem using acoustic waves.

Acoustic counterflow occurs when fluid in a channel is drawn opposite the direction of SAW propagation due to atomization at the fluid/air interface and coalescence upstream[272] (*see* Fig. 36). Masini *et al.* showed that fluid can be turned at right angles and split at an intersection in a 2D array of PDMS channels by this method.[273] Recently Shilton *et al.* performed mechanistic investigations of this technique.[274] The authors showed that the input power required for atomization in a channel did not increase over the frequency range 50–750 MHz. They also observed optimal SAW transmission through the channel when its width, W, was greater than $10\lambda_{SAW}$. This allowed them to produce optimal counter-flow in very small channels by increasing the SAW excitation frequency. They found that flow vortices in the channel scaled with the size of the channel if the frequency was adjusted to match $W = 10\lambda_{SAW}$ (unsurprising since β^{-1} decreases with increasing f). Similar to Shilton's work on sessile drops in 2014, these findings could allow further miniaturization of SAW microfluidic devices. As an interesting side note: we have seen that viscosity also plays a role in acoustic attenuation (the cause of streaming vortices) and an earlier study[275] showed that channel vortices were reduced in length with increasing viscosity, which again demonstrates the similar effects of viscosity and acoustic actuation frequency.

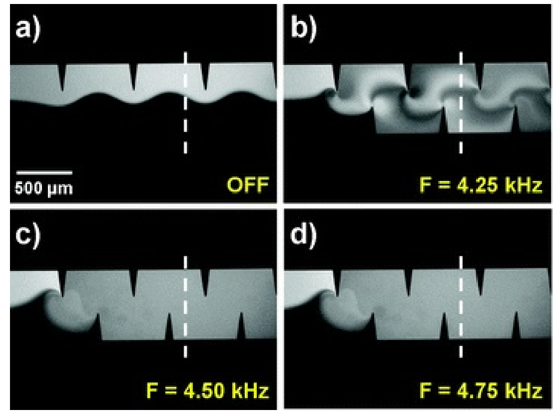

Fig. 35 Sharp-edge oscillation induced by PZT transducer produced acoustic streaming and performed mixing in the microchannel. With different applied frequencies, the mixing performance differs, as shown in (b), (c), and (d). Reproduced[268] with permission from The Royal Society of Chemistry.

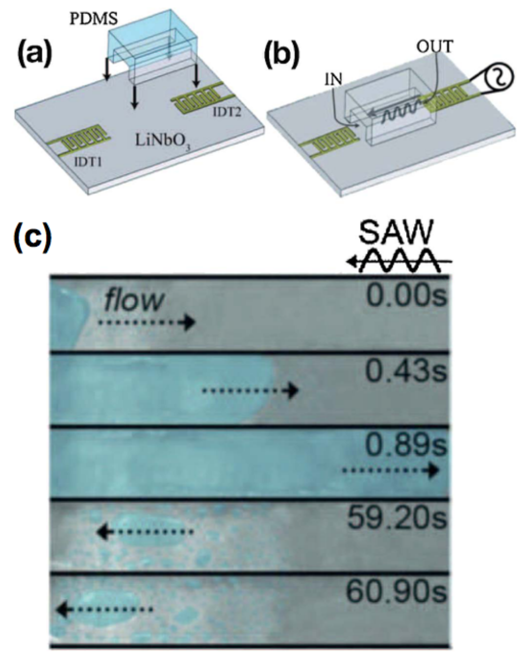

Fig. 36 A PDMS channel was bonded onto a LN substrate with two straight IDTs at two ends of the channel, as shown in (a), (b). The liquid performed counterflow relative to SAW propagation due to atomization at liquid-air interface and coalescence upstream, as shown in (c).

Acoustic counter flow cannot be used for closed channel systems where no free air/liquid interface exists. However, conventional pumping (rather than counter-flow) is difficult using SAW since the maximum amplitude of a travelling SAW on a LN substrate is ~10 nm, which produces negligible peristaltic effect in a

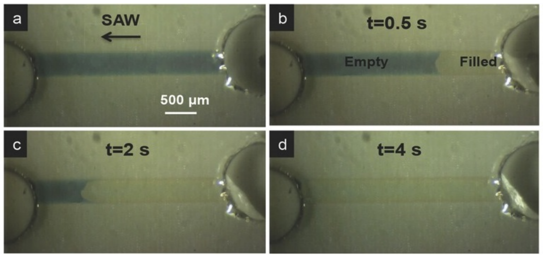

Fig. 37 LN nanoslit filling with water induced by SAW propagation from the right end of the nanoslit. The capillary filling rate of the hydrophilic LN nanoslit can be increased by 2–5 times when SAW is applied in the same direction. The magnitude of SAW is in the same order as the channel height so that it has a unique pumping mechanism different from SAW-induced pumping in microchannel, which needs to be further investigated. Reprint permis. Miansari (2016).[75]

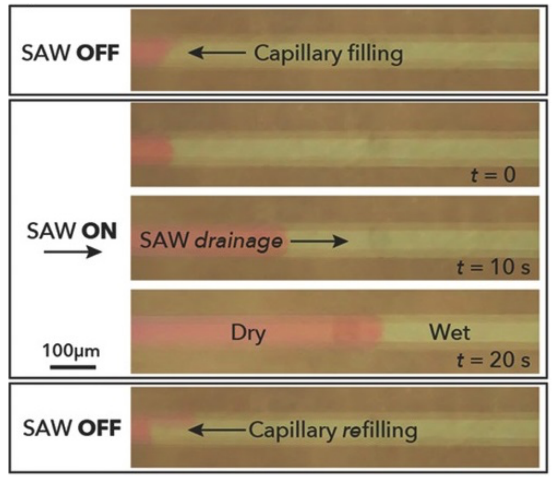

Fig. 38 Water drainage in LN nanoslit induced by SAW. SAW drained the nanoslit against 1 MPa capillary pressure when SAW was applied in the opposite direction of capillary filling. It showed powerful SAW-induced pumping effect in a nanoscale channel. Reprint permis. Miansari (2016).[75]

microscale channel. Instead fluid flow is due to acoustic streaming that tends to promote vortices, which in turn lead to circulation rather than unidirectional flow across the channels entire cross section. A possible solution to this problem was presented by Tan, *et al.*[246,276] They changed the width of the channel relative to the wavelength of sound in the fluid and observed uniform pumping of fluid flow when $W < \lambda_f$. This first demonstration of SAW-based uniform pumping was accomplished in a short, isolated channel segment with no inlet or outlet. Subsequently, Schmid *et al.*[277] demonstrated a continuous, closed-loop SAW-driven PDMS microchannel pump. Lossy interaction between SAW and PDMS was avoided by elevating the PDMS on water and glass coupling layers. They used a high frequency device (142 MHz) and a wide channel (1 by 0.75 mm) so that λ_f was much greater than W, which would seem to contradict Tan's conclusions. This inconsistency has not been explained and further work is required. A different type of SAW-driven pump device using an open-circuit channel constructed from glass (bonded directly to LN) was presented around the same time by Langelier *et al.*[125] ($W > \lambda_f$ again in this device). The elimination of extra coupling layers from the system greatly increased the pumping efficiency due to increased SAW transmission. It remains unclear how acoustic streaming creates unidirectional flow overall in these channels despite the presence of vortices in the path of the SAW.

In addition to mixing, the nanoslit demonstrated by Miansari and Friend[75] was shown to perform SAW-driven pumping at a remarkably large 1 MPa of pressure. The capillary filling rate of the hydrophilic LN nanoslit was increased by 2–5 times when SAW radiation was applied in the same direction as capillary filling, while the nanoslit could be drained against 1 MPa capillary pressure when SAW radiation was applied in the opposite direction (*see* Figures 37 & 38). Miansari was also able to pump an isolated droplet back and forth within the nanoslit using the same mechanisms. The reduction of channel dimensions to the nanoscale may remove previously unknown limitations of microchannel pumping.

Closed channel fluid pumping can also be accomplished via induced bubble oscillation[278–280] or via air/liquid interface vibration in LCATs.[281–283] The pumping mechanism is acoustic streaming in each case. Fang and Lee[284] demonstrated the potential consistency and stability of membrane-induced microchannel pumps by creating an LCAT-based oil/water droplet generator (*see* Fig. 39). In addition, Huang *et al.*[285] presented a programmable acoustofluidic pump based on the acoustic streaming effects due to the oscillation of tilted PDMS sharp-edge structures activated by a piezoelectric transducer. A stable and reliable pumping effect with 8 $\mu\ell$ min^{-1} pumping rate has been achieved.

4.4 Particle Manipulation in Closed Channels

SAW-based particle, droplet, and cell manipulation has been a popular topic of investigation in recent years, prompting several reviews on the subject.[12,14,286–288] Here, we will review the latest SAW-based manipulation results in four main areas: concentration and focusing, separation and sorting, patterning and manipulation, and droplet production and splitting. We will then cover the use of glass capillary tubes as an alternative to other ways of forming channels.

4.4.1 Concentration and Focusing

Particles and cells that have been focused within a flow cross section can then be easily detected by various methods. This process, cytometry, is a major capability required in biological assays and future lab-on-a-chip devices. Many focusing techniques have been investigated, including hydrodynamic, electrokinetic, and dielectrophoresis (DEP) methods. However, the SAW method is simple, highly efficient, contact-free, and can be applied to focus a wide variety of microparticles. Furthermore, the transparency of LN makes it feasible to integrate with most optical techniques.

Shi *et al.*[289] demonstrated particle focusing in a microchannel by depositing two IDTs on each side of the channel. The channel width and the wavelength of SAW were specified so that a SSAW formed across the channel width with a single pressure node located at the channel center, collecting particles at this node (*see* Fig. 40). Zeng *et al.*[290] then integrated Bragg reflec-

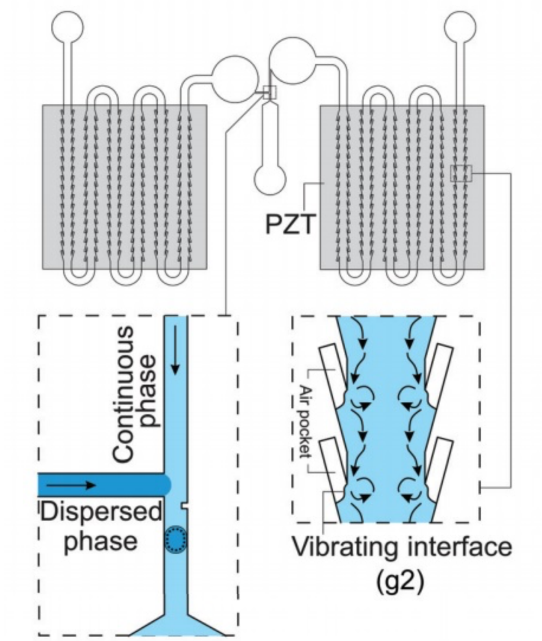

Fig. 39 Air cavities were trapped when the fluid was pumped into the channel. The vibration of air-liquid membrane produced the acoustic streaming and caused the pumping mechanism in the closed channel. Membrane-induced acoustic streaming instead of SAW-induced acoustic streaming showed better uniformity and effectivity for closed channel pumping in microscale. Droplet generation based on pumping in oil and water phases were demonstrated.

tors (BR) with the focusing device to enhance SSAW formation. Air cavities were also introduced on both sides of the microchannel and SSAW propagation area in order to reduce absorption by the PDMS walls. Jo and Guldiken[291] utilized these focusing capabilities to perform density-based particle separation.

To perform SSAW-based on-chip flow cytometry, 3D focusing capabilities are desired in order to maintain constant focal depth during cell detection. Shi *et al.*[292] discovered that the acoustic radiation force in the z-direction (perpendicular to the device plane) is also non-uniform. Through theoretical and numerical calculations, they showed that this non-uniformity could be used to force particles toward the plane of maximum acoustic kinetic energy which had a constant height with respect to the substrate. Experimental results agreed with these calculations and they were able to perform SSAW-based 3D continuous particle focusing in a microchannel.

TSAW can also be used for particle focusing, as demonstrated by Tan *et al.*[276] A single IDT generates a SAW that is subsequently reflected from the opposite channel wall that generates a standing acoustic node within the channel if conditions are engineered correctly. Relatively weak SAW was used in Tan's work to focus particles in an initially homogeneous suspension into equally spaced nodal lines parallel to the channel with a separation of one-half the wavelength (*see* Fig. 41). The dependence on wavelength allowed particles to be focused to different locations based on the applied frequency (using a slanted IDT). Witte *et al.* produced a similar device, but added a glass superstrate.[293] A slanted IDT allowed for small differences between superstrates to be compensated for by tuning the resonant frequency. This kind of technique will allow cytometry within disposable inserts, which could allow for quick, clean processing of many samples in sequence on a single device.

Tan *et al.* presented a unique way of performing cytometric functions using TSAW streaming and non-nodal radiation.[294] A double-aperture FIDT enabled asymmetric actuation so that particles could be directed to the left or right as they are propelled along the channel. They also milled the channel cross section into a trapezoidal shape that greatly reduced the formation of standing waves (similar to the effect of an anechoic chamber) so that particles would not be trapped along nodal lines.

4.4.2 Separation and Sorting

The goal of particle separation and sorting is to lead specific particles from their original streamlines to targeted streamlines which finally flow into a sorted outlet. Related SAW techniques can be divided into two general categories: TSAW-based and SSAW-based. Franke *et al.*[295] first presented continuous droplet sorting in a PDMS microchannel using TSAW. Droplets flowed passively into one channel, but were pushed into the path of a second channel by acoustic streaming when actuated. However, this technique cannot inherently differentiate between particles and thus can only temporally sort. Destgeer *et al.*[296] were able to continuously isolate particles of a single size from an assortment of particles by utilizing the acoustic radiation force of TSAW. As mentioned earlier, detachable superstrates are potentially useful for applications where biological samples are processed. Ma *et al.*[297] developed a device similar to Destgeer *et al.*, but with a PDMS superstrate that contained the microfluidic channels. They

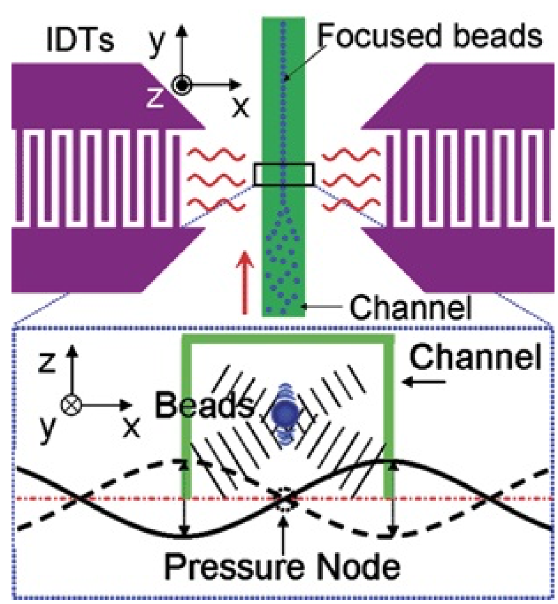

Fig. 40 Schematic and working mechanism of the SSAW-based focusing device. The IDTs were on the opposite side of the channel. The width of the channel was matched with the wavelength of SAW to generate single pressure node at the center of the channel. The acoustic radiation force led beads into pressure nodes to perform particles focusing. Reproduced[289] with permission from The Royal Society of Chemistry.

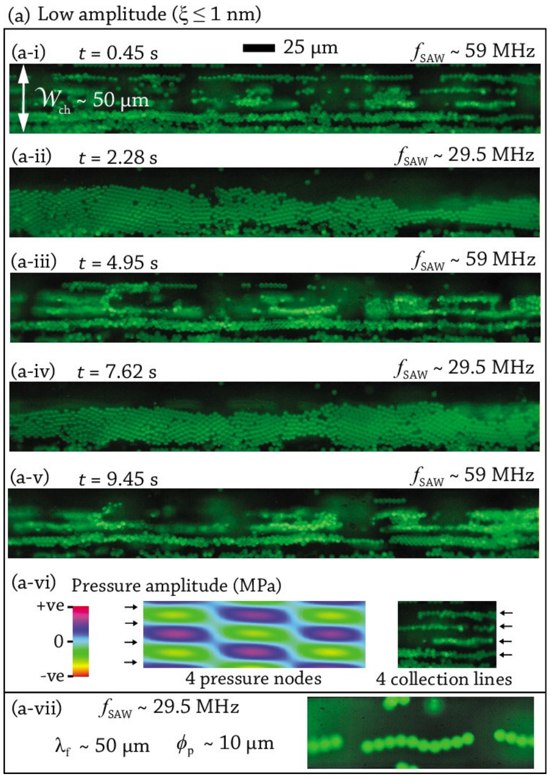

Fig. 41 Time lapse images of TSAW focusing in a microchannel at amplitudes below 1 nm. Specific lines of focus could be selected by applied frequency and were quickly and easily switched, in this case between 29.5 MHz and 59 MHz. Reprint permis. Tan (2010).[276]

also developed a platform for separating particles of similar sizes but with different densities using TSAW of carefully selected frequency.[298]

TSAW methods displace particles from their original laminar flow path, but SSAW methods sort particles into one or more nodal paths regardless of their original path. Also, recall that the acoustic radiation forces due to TSAW and SSAW differ strongly in their dependence on particle size (*see* Eqns. (5) and (6)). Size-based[299–302] and density-based[291] particle separation have been demonstrated. Numerical studies on SSAW in microchannels has further explained the mechanism of particle separation. A two-dimensional model helped reveal the effect of boundary vibrations and channel properties on particle aggregation near PDMS channel walls.[303]

Wu *et al.*[304] further scaled down the particle separation technique to submicron scale. Tilted-angle SSAW was utilized to separate 500 nm and 110 nm particles, showing a finer resolution for particle separation than the standard SSAW configuration. Next, Kishor *et al.*[305] demonstrated integration of tilted-angle SSAW with a photoacoustic detection technique into an integrated microfluidic platform capable of size-based separation, concentration, and quantitative detection of microparticles. Such integrated platforms show promise for future lab-on-a-chip systems that utilize the functionality described in this review.

The ability to separate microscale particles has also been shown using SFITs. Destgeer *et al.*[296] was able to separate particles into three size groups by placing SFITs with two distinct frequency ranges on either side of a microchannel. Thus, TSAW could be generated at desired frequencies and locations. Recently, Park *et al.*[306] demonstrated bidirectional, multichannel droplet sorting using SFITs. They also added a new functionality: dynamic formation of temperature gradients in the channel.

In a more biologically relevant proof of concept, Nam *et al.*[307] demonstrated a device to separate blood cells from platelets using SSAW. Pressure nodes were set up near the two side walls and blood cells experienced larger acoustic radiation forces, since they are larger than platelets, and moved to the sides of the channel while platelets remained at the center. The authors reported platelet purity up to 98% using this method. They were also able to separate beads of polymer encapsulated cells based on their density.

Using focused SAW of higher frequency (up to 636 MHz), Collins and Ma[308,309] recently demonstrated size-selective particle concentration—as small as 300 nm—via acoustic streaming. In one arrangement, streaming and radiation concentrate particles to one edge of a flow (*see* Fig. 42). Note that size selective concentration in sessile drops has been demonstrated down to 200 nm.[161] Concentration generally refers to separating many particles at once into two or more groups, while sorting considers one particle at a time.

Depending on the position and design of the acoustic source, both SSAW[289,310] and TSAW[311] devices can be used for cell sorting, as the acoustic actuation area in the fluid can be well controlled. A high-throughput acoustic cell sorter using focused SAW was introduced by Ren *et al.*[312] An FIDT allowed them to generate SSAW with higher energy intensity and a narrower beam width resulting in a larger actuation force and a higher sorting resolution (*see* Fig. 43). According to their data, the FIDT exerted 4–9 times larger acoustic radiation force than did the straight IDT, indicating that to attain the same sorting effect an FIDT would require only 10–20% of the input power of a straight IDT. Collins *et al.*[313] demonstrated a very similar system only they used TSAW rather than SSAW and used a higher frequency, 386 MHz, to achieved even finer resolution particle sorting (similar to Fig. 43), but with only one FIDT). They shrunk the actuation area to a few tens of micrometers with highly focused SAW that produced large acoustic gradients. With pulse durations of $\sim$100 μs, they were able to nudge particles as small as 2 μm from their path without altering the path of the next particle in sequence.

4.4.3 Patterning and Manipulation

The ability to arrange cells and microparticles into desired patterns is important for many biological applications, for example in tissue engineering.[314] Patterning of particles in one and two dimensions using SAW has been recently demonstrated. Wood *et al.*[162] first performed 1D patterning (also known as alignment) of particles using SSAW in microfluidic systems. As a next step, they performed 2D patterning using two pairs of counter propagating IDTs in orthogonal directions.[315] They used a liquid coupling film similar to that used by Schmid,[311] which cannot support continuous operation due to a lack of inlet and outlet ports. Shi *et al.*[316] enabled continuous 1D and 2D patterning by bonding PDMS directly to the substrate to form a closed channel.

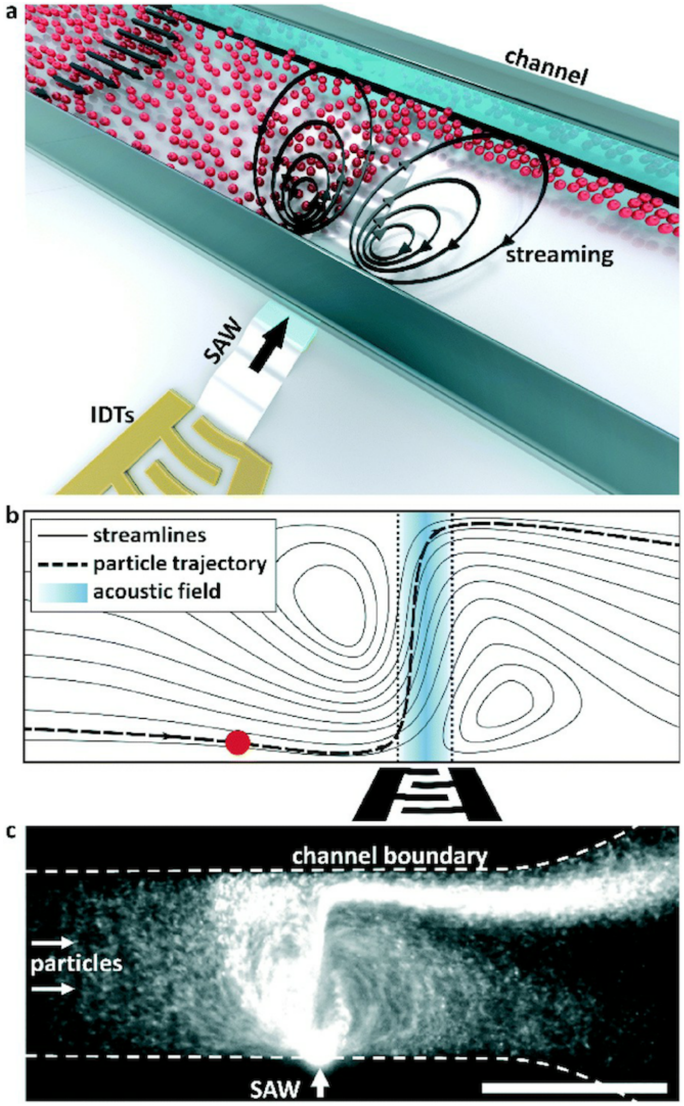

Fig. 42 Principle of SAW based nanoparticle focusing of using SAW. (a) A conceptual diagram: the combined streaming field and acoustic radiation forces resulting from the coupling of substrate vibrations produced by an IDT on a piezoelectric substrate results in focused particle displacements. (b) A particle (red) is displaced relative to the fluid streamlines by the acoustic radiation force as it passes through a focused SAW beam. The streaming serves to direct the particle laterally to the acoustic beam and maximize its exposure to the acoustic gradients in its periphery. (c) A continuous influx of 300 nm particles is focused in a low velocity flow. Adapted[309] with permission from The Royal Society of Chemistry.

Building on this concept, O'Rorke *et al.* [317] achieved translation of a patterned array of particles by modulating the frequency of the SAW. The pattern could be translated laterally by up to one wavelength (∼118 μm in this case—a standard, straight ∼30 MHz device) by changing the frequency in small increments across the bandwidth of the IDT.

In the last five years, other forms of patterning using SAW have been presented. Ding *et al.* [318] performed tunable 1D and 2D patterning of microparticles using slanted-finger IDTs (SFITs), which offer a much larger resonant frequency bandwidth than the standard IDTs used for translation. They showed that, by tuning the

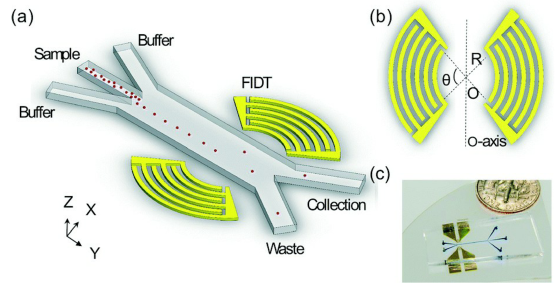

Fig. 43 (a) Schematic of the SSAW-based sorter excited by FIDT. (b) The concentric geometry of the FIDTs. O is the focal point and the two sets of FIDTs is O-axis symmetric. (c) An optical image of the high-throughput SSAW sorter. Adapted[312] with permission from The Royal Society of Chemistry.

frequency applied to the SFITs, they could vary the line spacing of a 2D pattern, for example, from 141 μm to 250 μm. Another novel patterning capability was added by Collins *et al.* [319] who produced patterning in only a desired section rather than over the entire area between two transducers. They engineered nanosecond pulse signals whose duration was less than the time-of-flight between transducers so that standing waves were only set up in a central region of tunable width. Yet another degree of freedom was demonstrated by Tian *et al.* [320] who could control both the spatial patterning and the shape of microdroplets themselves, which compose the pattern.

Particle patterning into defined nodal positions is useful, but in addition, some applications require the movement of particles to arbitrary locations. This has been accomplished with a technique known as acoustic tweezers, an old concept[321,322] receiving renewed interest. Compared to optical tweezers, acoustic tweezers require lower power density, are bio-compatible, and are amenable to miniaturization. The nodal position can be tuned by either phase shift[323] or frequency modulation[324,325] (*see* Fig. 44). More recently, Devendran *et al.* [65] used an acoustic field combining both traveling and standing wave components along with a swept excitation frequency to collect and isolate particles of different sizes in a static fluid volume. The varied tools created through more and more complex acoustic field control are bound to be useful in other fields where small particles need to be manipulated. One such example is the work by Chen *et al.* [326] who used acoustic tweezers to trap cells in a micro-channel for cell enrichment. The cells accumulated at SSAW nodes as more and more fluid was passed through the channel. They reported an increase in concentration of originally dilute red blood cell samples (10^5, 10^4 and 10^3 cells per mL) by a factor of 100–1000. Especially exciting is the ability to independently manipulate individual particles amid others via localization of the acoustic energy flow as described by Baresh *et al.* [327,328] In the context of the work by Riaud *et al.*, [118] it is likely that we will soon see far more powerful particle manipulation devices for lab-on-a-chip applications in the near future.

We point the interested reader to a more detailed review of dynamic ultrasonic field control presented by Drinkwater.[329] It includes in-plane manipulators, beam manipulators, and planar

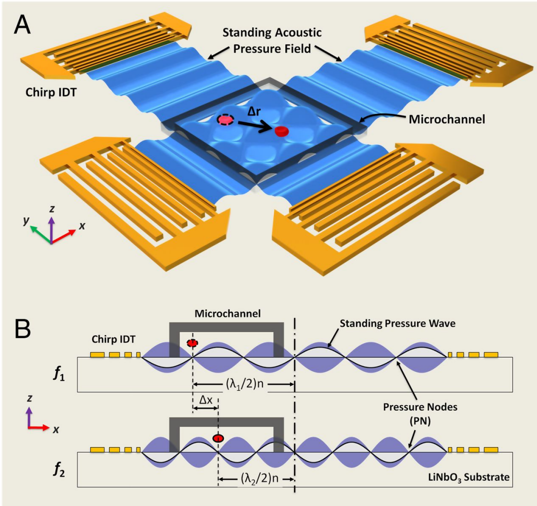

Fig. 44 Two-dimensional particle manipulation with frequency-control using chirped IDTs. A microchannel was bonded near one side of chirped IDTs. Particles in the pressure nodes were forced to move by changing the location of pressure nodes, which were dependent on the frequencies of SAW .[324]

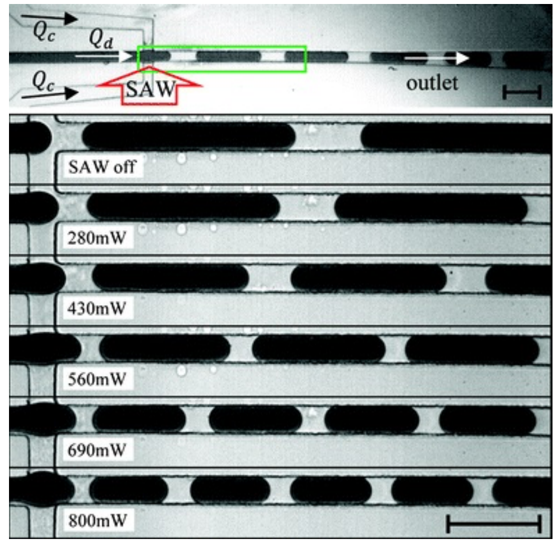

Fig. 45 SAW was applied at the flow-focusing droplet/plug generation region and regulated the plug size by different SAW power. Stronger SAW power reduced pinch off time due to increased interface pressure, which in turn reduced the size of plugs. Reproduced[330] with permission from The Royal Society of Chemistry.

array manipulators used for transportation and rotation of individual particles as well as biosensing and microscale assembly in channel-less microfluidic devices.

4.4.4 Droplet Production and Splitting

SAW actuation has become a promising tool for droplet generation, droplet splitting, and droplet manipulation because it is inherently robust and contamination-free. The general idea is to apply acoustic streaming or acoustic radiation force induced by SAW near a fluid-fluid interface in order to produce drops of a dispersed phase within a continuous phase (*see* for example the bottom left of Fig. 39).

Schmid and Franke[330] integrated an IDT at the junction of flow-focusing channels as seen in Fig. 45. The magnitude of SAW power—rather than channel geometry or flow speed—was used to regulate droplet size. This method relies on increased pressure at the lower inlet due to acoustic streaming. Collins *et al.*[6] used an FIDT to demonstrate droplet generation from a T-junction in order to encapsulate concentrated particle suspensions. A low-power SAW was activated to move and concentrate particles at the interface, then a high-power pulse was used to deform the interface and generate a water-in-oil droplet with encapsulated particles. Based on a similar device configuration, Brenker *et al.*[331] experimentally and numerically explored the working mechanism of the FIDT-induced T-junction droplet generator. They identified three distinct droplet production regimes depending on the relative speeds of the continuous and dispersed fluid flows.

SAW-induced drop splitting in microchannels has also been recently demonstrated. Sesen *et al.*[332] performed water-in-oil plug steering and real-time on-demand plug splitting using an FIDT-integrated Y-junction microfluidic device. Two FIDTs (one on each side) were pointed directly at the junction from the direction perpendicular to the inlet channel. Precise acoustic radiation pressure on the oil/water interface allowed the plug to be steered entirely into one outlet or the other, or to be split into desired proportions (without actuation the plug would naturally split in half). Jung *et al.*[333] used SFITs instead of FIDTs to direct acoustic radiation pressure to a specific region for droplet splitting based on the input frequency. Sesen *et al.*[334] applied pulsed acoustic streaming in a branched channel to suck a portion of fluid into it thus splitting droplets as they passed (*see* Fig. 46).

Sesen *et al.*[335] also reported on-demand droplet merging using focused SAW. Acoustic radiation forces generated from an FIDT were used to stop the progress of a selected droplet such that successive droplets merged until a certain volume was reached

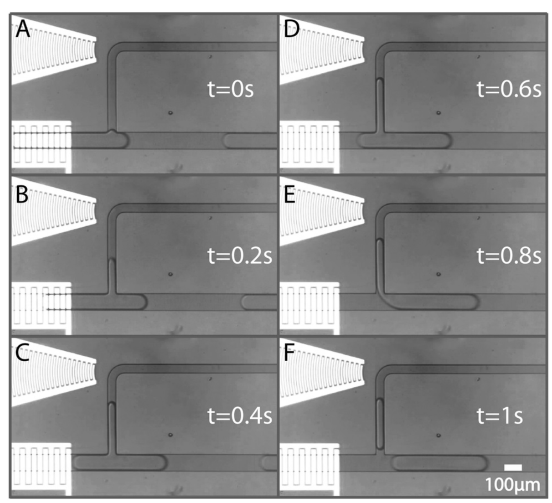

Fig. 46 Droplet splitting in closed branched microchannel induced by SAW. FIDT-induced acoustic streaming produced a pressure offset between the main channel and the branched channel, and performed as a micropipette in the closed channel. Reproduced[334] with permission from The Royal Society of Chemistry.

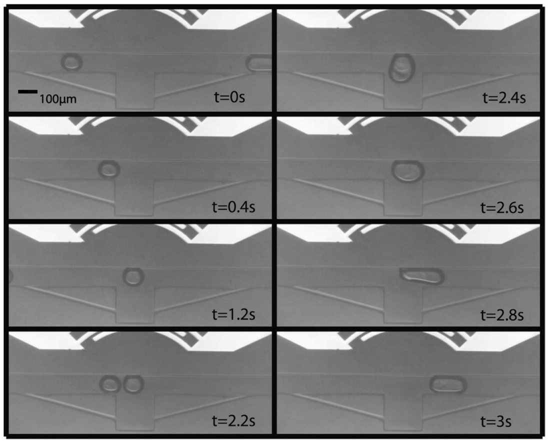

Fig. 47 Time lapse images of the droplet merging experiment. The first droplet is immobilized across the FIDTs while the next droplet comes and merges with the stationary one. The merged droplet travels downstream because the acoustic energy in the system is not enough to hold a bigger volume droplet. The FIDTs is placed at the right-side while the oil flow is from left to right. Reproduced[335] with permission from The Royal Society of Chemistry.

(*see* Fig. 47).

Jung *et al.*[336] demonstrated on-demand droplet capture and release at specific microwells using SFITs. At different frequencies, different parts of the SFITs resonated corresponding to the designed wavelength at that location. Thus the location of a particular microwell could be selected and droplets could be pushed into or out of it as desired.

4.4.5 Particle Manipulation in Capillary Tubes

We have already covered the phenomena where by nodes and anti-nodes form in acoustic resonant cavities which we have called channels. Capillary tubes can also be used as resonant cavities. They can be bonded to a piezoelectric substrate often more easily than a channel can be fabricated in the substrate or in some superstrate. Being widely used in other industries capillary tubes are easily obtained in many sizes and shapes as ready to use parts that both have well known properties and are disposable.

A review by Lenshof *et al.* presents a useful summary of the work done in this area.[337] They cover the focusing and trapping of particles and the use of these techniques in bio-chemical assays. Another good example, not found in the above review, is the work of Grundy *et al.*[338]. They applied this technology to rapid diagnostics and were able to reduce, for example, the agglutination time of bacteria from four hours to only five minutes by encapsulating samples within droplets within a capillary tube. Work by Araz *et al.*[339] is also valuable due to the simplicity of the design in which particles are separated based on size and/or density along the length of the capillary due to bending modes produce by actuation of a C-shaped PZT plate.

We also wish to highlight two works that have been published since the review by Lenshof. Gralinski *et al.*[340] have performed numerical simulations of particle trapping in capillaries with circular cross sections. They vary several design parameters and discuss the advantages of a design containing four PZT transducers for particle focusing in the center. A follow up paper[341] presents experimental results and also includes patterning along the length of the capillary tube. Recently, Mao *et al.*[342] published work on coupling SAW into a capillary tube bonded to a LN substrate. They showed that in this case not only are nodes established due to acoustic radiation, but also acoustic streaming establishes a single vortex which allowed them to focus particles in the nanometer size range. We cover this work further in the following section.

4.5 Reorientation of Nanoscale Objects

Acoustic waves are widely used for in-situ manipulation of nano-objects because they are simple to produce, highly biocompatible, contact-free, and capable of rapid actuation. Carbon nanotubes (CNTs) have aroused the interest of researchers in recent decades due to their mechanical strength and electrical conductivity,[343,344] but they also show promise in nanoscale fluid transport.[345–347] However, in order to be utilized in these applications, CNTs must be properly oriented. For example, CNTs can be used to reinforce polymer composites, that perform better when the nanotubes are aligned using acoustofluidics.[348]

Strobl *et al.*[349] utilized SAW to align multi-walled carbon nanotubes (MWNTs) with an angle of 25°–45° on LN with respect to the wave propagation direction. They explained that the MWNT alignment resulted from the piezoelectric field and SAW propagation, thus the acoustic streaming generated by SAW actually shifted the MWNTs from being directly aligned with the piezoelectric field. Ma *et al.*[350] further discussed the acoustic radiation effect and the dielectrophoretic effect (due to the piezoelectric field) on the patterning mechanism of CNTs. Numerical simulation and corresponding experiments showed that the dielectrophoretic effect dominates over the acoustic radiation effect when patterning CNTs because of their high conductivity and high aspect ratio. Conversely, the acoustic radiation effect dominates when patterning low aspect ratio and less conductive objects. Besides carbon nanotubes, metallic microtubes[351] and nanowires[352] can also be patterned using SAW while dispersed in a liquid via the dielectrophoretic effect since they are also highly conductive and have high aspect ratios. Seemann *et al.*[353] then demonstrated that SWNTs and MWNTs can be deposited and aligned between pre-structured metal contact pads on silicon using SAW. The use of silicon makes this technique more compatible with microelectronics applications.

Recently, Miansari *et al.*[354] also presented deagglomeration and alignment of MWNT bundles on a dry surface via SAW. The absence of fluid on the surface eliminated the influence of streaming so that acoustic radiation forces could deagglomerate the nanotube bundles. The alignment mechanism relied on van der Waals interactions between the nanotubes and a glass slide, which was placed on top of them to constrain out of plane movement.

In some pioneering work on concentrating nanoparticles, Mao *et al.*[342] demonstrated use of a single vortex generated using SAW for focusing 80–500 nm diameter silica and polystyrene particles. These were used to capture fluorescent biomarkers to enrich the emitted signal. By way of extension, Wu *et al.*[355] separated exosomes from whole blood. This was conducted in two stages, first separating larger blood components before the second stage which targets the exosomes. Both these studies potentially lay the foundation for applications such as health monitoring and medical diagnosis among others that would benefit from nanoparticle separation.

5 Nanofluidics

When we zoom into the nanometer scale, several interesting and fundamental physical and chemical phenomena become accessible, including nonlinear electrokinetic flow and ion focusing,[356,357] nanocapillarity,[358] mass transport in nanoscale spaces,[359,360] and electrical double layer (EDL) overlap effects.[361–363] DNA stretching,[364] detection of single DNA molecules,[365] water purification,[366] and many other practical applications have been demonstrated using these effects.

Several review papers have been published about nanoscale fluid transport[360,367–369] and flow in CNTs[345–347] in the last ten years. Extremely high aspect ratio, nanoscale inner diameter, and molecularly smooth hydrophobic graphitic walls make CNTs an ideal applicable material and platform for investigating nanofluidics. Numerical molecular dynamics simulations of nanopumping through CNTs has been presented by Insepov *et al.*,[370] Longhurst *et al.*,[371] and Rinne *et al.*,[372] showing that the nanopumping phenomena can be driven by temperature, AC electric fields, and the friction between gas particles and nanotube walls induced by SAW.

In addition to CNTs, inorganic nanotubes have been synthesized for use as a novel platform for nanofluidics.[373] Their advantages included a controllable inner diameter from 1 to 100 nm, facile functionalization of the inner and outer surfaces, and tunable compositions and aspect ratio. These features effectively provide the ability to mediate the ionic and electrostatic environment, both spatially and temporally. These forces are dominant at the femtoliter scale, which makes inorganic nanotube synthesis a powerful tool for femtoliter biological and chemical analyses.

Acoustic *nano*fluidics exhibits significant differences from acoustic *micro*fluidics and has not yet been as well developed.[374] However, early results are promising. Insepov *et al.*[370] used molecular dynamics simulation to predict a new nanopumping effect where SAW at the surface of a CNT cause gas flow within. The SAW-induced peristaltic motion along the CNT surface was predicted to pump the gas at 30 km/s. At these small scales, light can be used to create sound. Lin *et al.*[375] showed optical generation and spatial manipulation of nanoacoustic waves with nanoscale spot sizes. Pezeril *et al.*[376] was able to optically generate GHz-frequency shear acoustic waves in liquid glycerol. Van van Capel *et al.*[377] generalized nonlinear ultrafast acoustics at the nanoscale, reviewing both main properties of nonlinear ultrafast acoustic propagation and recent results. These initial investigations have set the stage for further practical applications.

The fabrication of nanoslits and nanochannels,[369] fluidic devices with nanometer scale in one or two dimensions, respectively, has been demonstrated[378–380] and applied to a number of applications such as DNA stretching[364,381,382] and single DNA molecule dynamics,[383,384] due to their flexibility of channel shape and surface properties. More specifically for acoustic nanofluidics, room-temperature bonding of LN to silicon wafers was demonstrated by Takagi *et al.*[385] and has been widely used to achieve enclosed nanochannels for the acoustic propagation of fluid.

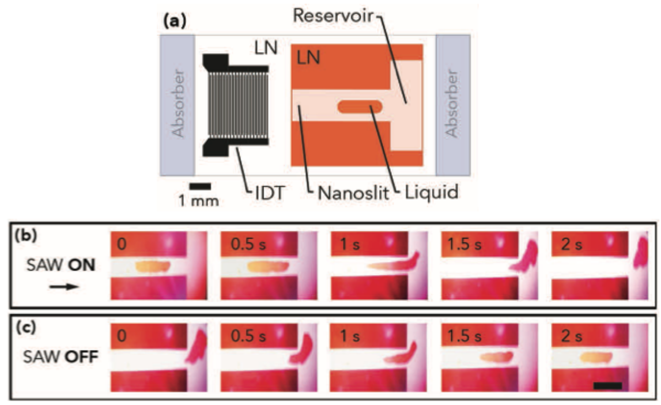

Fig. 48 Manipulation of a liquid drop within the nanoslit based on SAW-driven acoustic streaming and capillary forces. When SAW was on, the SAW-driven acoustic streaming overcame the capillary force in the T-shape channel and pushed the liquid drop into the reservoir. When SAW was off, the capillary force led the liquid drop into the targeted nanoslit. Reprint permis. Minasari (2016).[75]

Recently, Miansari and Friend[75] developed a novel room temperature LN/LN bonding technique and demonstrated a SAW-induced nanoslit platform for pumping nanoscale flows at up to 1 MPa (*see* Fig. 37), manipulating 10 fL drops (*see* Fig. 48), and separating nanoscale particles by size. The mechanisms responsible for these results need to be further investigated and explained in the future.

6 Conclusions

Acoustic waves can be generated at the surface of a piezoelectric material by passing an electrical signal through electrodes deposited on the surface. The crystal structure, propagation direction, and wave mode are important considerations when choosing a substrate and electrode system for the fabrication of new acoustofluidic devices. The combination of interdigital transducers on lithium niobate has become most popular in the field due to relatively high coupling coefficients, transparency, biological and microfabrication compatibility, and the ability to produce efficient, predictable surface acoustic waves at high frequency. Acoustic energy couples into a fluid placed on the surface of such devices producing both acoustic streaming and an acoustic radiation force. The wave at the interface between fluid and substrate is attenuated over a characteristic length and the wave in the fluid attenuates over another distinct characteristic length.

We discussed how these phenomena have been used to actuate sessile drops in four ways: mixing, translation, jetting, and atomization. Flow can be generated in the altitudinal or azimuthal plane and can be manipulated to achieve poloidal and other more complicated flows by the choice of fluid properties and the design of IDTs. These flows, in addition to acoustic radiation and other forces, can be used to manipulate particles in sessile drops in order to perform a wide range of processes necessary for lab-on-a-chip applications. Selective concentration, separation by size or density, and convective mixing can all be achieved rapidly on very similar if not identical platforms at low power and, furthermore, the drops can then be controllably translated, combined, and separated on the same surface. The combination of these capabilities makes SAW microfluidics very attractive for biological assays, and especially so since SAW has been proven harmless to many bio-particles and organisms in the necessary power and frequency ranges.

The mechanism of flow is acoustic streaming via viscous attenuation, but the mechanism of translation is very likely a combination of streaming and radiation pressure on the free-surface that deforms the drop so that it oscillates vertically and moves in an inchworm-like fashion. At increased power, these oscillations can be extended to form liquid jets with predictable break-up events. This phenomena has been successfully applied to extensional rheology, but there is a lack of other jetting applications in the literature though the potential exists (e.g. ink-jet printing). The mechanism underlying atomization is much less clear. The prediction of droplet size has improved, but not to the point of confirming the mechanism on which the theory is based. It is clear, however, that the mechanism and droplet size is critically dependent on the geometry of the fluid. Atomization has applications outside of biological assays like pulmonary drug delivery, materials fabrication, surface cooling, and others and this list will certainly grow in the future as control over atomized mists via acoustic actuation continues to improve. Both internal flow and translation of drops—as well as jetting and atomization—can be enhanced by the use of specialized IDT designs (e.g. FIDTs) and signal modulation. These two parameter spaces have not been fully explored and future work in this vein could reveal new and improved microfluidic capabilities.

We also evaluated acoustofluidics in closed channels—the platform where most traditional microfluidics occurs. Mixing in traditional microfluidics is difficult due to low Reynolds numbers, but SAW and BAWs are used to easily mix fluids. Bubbles and sharp edges can be incorporated to enhance and expand this capability. Fluid pumping can be achieved via acoustic counterflow or via tightly confined acoustic streaming, and has been demonstrated in closed circuits in both glass and PDMS. Particles have been manipulated in many ways including: concentration, separation, focusing, sorting, and patterning. Techniques based on both standing and traveling SAW were presented and most techniques are easily tunable based on the frequency of the acoustic waves. In addition, drops of a second, immiscible fluid can be formed, split, and merged within channels. This type of lab-on-a-chip platform combines the small volumes and discrete nature of planar sessile drop microfluidics and the simple, evaporation-free operation of continuous channel microfluidics. Acoustofluidcs also offers particle motion control along the length of a channel and capture and release of particles from micro-wells. Clearly there is a large and expanding set of capabilities related to acoustic actuation in closed channels, which again makes SAW microfluidics attractive for biological assays.

Finally we presented the relatively less developed, but exciting field of acoustically actuated nanofluidics. Carbon nanotubes can be oriented with SAW and they have also been presented as an ideal platform for nanoscale fluid flow. Early work has shown that very fast pumping rates, mixing, femtoliter drop manipulation, and nanoparticle separation are possible. The underlying mechanisms and potential applications remain to be explored.

Micro-scale acoustofluidics retain all the features of traditional microfluidics with many added benefits. The resulting devices are inherently simple to operate since they rely on electrical signals. And they have low power requirements that allow the possibility of self-contained, hand-held devices. This field also offers novel functionality beyond mimicking existing lab scale processes, which increases incentive for further development and eventual commercial adoption.

However, it is also important to recognize the limitations of this technology. There are a few examples of integrated systems that incorporate acoustofluidics in academia, and even fewer examples in industry despite the fundamental and proof of concept progress outlined in this review. We believe this is due to a lack of interdisciplinary groups that contain both microfluidics experts and acoustics experts. Similarly, there have not been enough resources dedicated to developing the circuit design knowledge necessary to drive acoustofluidic devices, which have a unique set of circuit requirements. Devices typically operate between 50–3000 mW and 5–200 MHz and tunable frequency and power output is often desired. We expect these challenges to be overcome in the near future, but there a several inherent limitations of which the reader should be aware. In many of the applications given in this review, other technologies can produce superior performance in ideal situations. For example, electrospray produces smaller more monodisperse droplets than does acoustic atomization, which leads to higher performance in mass spectrometers, but the acoustofluidic devices are easier to use. Similarly, optical tweezers can manipulate particles at a smaller length scale than acoustic tweezers, but require more expensive equipment and restrict the application space due to heating. Many acoustofluidic devices rely at least in part on streaming which only occurs when acoustic waves are attenuated. Thus acoustofluidic devices are inherently limited by attenuation, and exceedingly low frequencies and high power are necessary to deliver sufficient energy to manipulate large volumes of fluid. Indeed, the capabilities of acoustics appears to be ideally suited for small-scale lab-on-a-chip applications in micro to nanofluidics once the many complexities are addressed with further research.

We hope that the information assembled here inspires those within and outside the field to consider integrating acoustofluidics into their own research and development, providing a fresh perspective on the discipline to benefit both experts and newcomers to the field.

7 Index

α^{-1} length along the surface of the solid over which a Rayleigh wave decays by a factor of e due to the emission of leaky SAW into the fluid

β^{-1}	distance that the longitudinal sound wave travels in the fluid before decaying by a factor of e
β_c	compressibility of particles
β_w	compressibility of fluid
δ	viscous boundary layer thickness
Δ_f	width of the resonant peak
ε	aspect ratio
ε_∞	capacitance per period of a unit-aperture, single electrode transducer
γ	surface tension
λ_{SAW}	wavelength of the SAW
λ_c	capillary wavelength
λ_f	wavelength of sound in the fluid
$\mathscr{R}$	recirculation length
μ	shear viscosity of the fluid
μ'	bulk viscosity of the fluid
ω	angular frequency
ρ_0	density of the fluid
ρ_p	particle density
ρ_s	density of the solid
θ	contact angle between a liquid and a solid
θ_R	Rayleigh angle
$2\Delta v/v$	coupling coefficient of the substrate
a	aperture width
A	amplitude of SAW
b	anisotropy of the substrate material
$B(\omega)$	susceptance
C_t	capacitance
Ca	capillary number
D	instability wavelength
D_F	distance from the IDT edge
d_s	effective focal spot size of an FIDT
f	applied piezoelectric excitation frequency
F_{rs}	SAW radiation force under a standing wave
F_{rt}	SAW radiation force under a traveling wave
f_{SAW}	frequency of the SAW
F_B	Bjerknes force
f_c	capillary wave frequency
F_D	Stokes drag force
f_r	resonance frequency
$G_a(\omega)$	conductance
H	vertical dimension (height)
$j(\omega)$	imaginary part of ω, angular frequency
k	wavenumber of SAW
k_0	propagating wave vector
L	lateral dimension (length)
L_c	characteristic length
N_p	number of finger pairs
Oh	Ohnesorge number
p_0	acoustic pressure
P_a	power that is absorbed
P_s	power that is produced
Q	quality factor
r	particle radius
R	drop radius
R_f	radius of the finger curvature
Re_a	acoustic Reynolds number
Re_s	streaming Reynolds number
t	time
U	amplitude of particle velocity
u	fluid velocity
u_1	first order fluid velocity
V	voltage
V_{pp}	peak-to-peak voltage
v_D	velocity difference between the surrounding fluid and the particle
v_l	speed of sound in the liquid
v_R	phase velocity for Rayleigh wave in solid
W	width of the channel
w	equivalent aperture of FIDT
W_b	-3 dB transverse bandwidth
We	Weber number
We_j	jet Weber number
x	position along the IDT fingers
X	film front displacement
y	position along the channel width
$Y_t(\omega)$	electrical admittance
z	effective focal length shifts

References

1 G. M. Whitesides, *Nature*, 2006, **442**, 368.
2 E. K. Sackmann, A. L. Fulton and D. J. Beebe, *Nature*, 2014, **507**, 181.
3 H. Becker, *Lab on a Chip*, 2009, **9**, 2119–2122.
4 H. Becker and C. Gärtner, *Microchip Diagnostics: Methods and Protocols*, 2017, 3–21.
5 C.-Y. Lee, W.-T. Wang, C.-C. Liu and L.-M. Fu, *Chemical Engineering Journal*, 2016, **288**, 146–160.
6 D. J. Collins, T. Alan, K. Helmerson and A. Neild, *Lab on a Chip*, 2013, **13**, 3225–3231.
7 L. Van Valen, *Evol Theory*, 1973, **1**, 1–30.
8 E. F. F. Chladni, *Discoveries on the theory of sound*, Weidmanns, Erben und Reich, 1787.
9 M. Faraday, *Philos. Trans. R. Soc. London*, 1831, **121**, 1831.
10 A. Kundt, *Annals of Physics*, 1866, **203**, 497–523.
11 J. Friend and L. Y. Yeo, *Reviews of Modern Physics*, 2011, **83**, 647.
12 X. Ding, P. Li, S.-C. S. Lin, Z. S. Stratton, N. Nama, F. Guo, D. Slotcavage, X. Mao, J. Shi, F. Costanzo *et al.*, *Lab on a Chip*, 2013, **13**, 3626–3649.
13 L. Y. Yeo and J. R. Friend, *Annual Review of Fluid Mechanics*, 2014, **46**, 379–406.
14 G. Destgeer and H. J. Sung, *Lab on a Chip*, 2015, **15**, 2722–2738.

15 C. Eckart, *Physical Review*, 1948, **73**, 68.
16 L. Rayleigh, *Proceedings of the London Mathematical Society*, 1885, **1**, 4–11.
17 R. White and F. Voltmer, *Applied Physics Letters*, 1965, **7**, 314–316.
18 B. Jaffe, *Piezoelectric ceramics*, Elsevier, 2012, vol. 3.
19 H. Birol, D. Damjanovic and N. Setter, *Journal of the European Ceramic Society*, 2006, **26**, 861–866.
20 X. Y. Kong and Z. L. Wang, *Nano Letters*, 2003, **3**, 1625–1631.
21 A. J. Lovinger, *Science*, 1983, **220**, 1115–1121.
22 S. M. Nakhmanson, M. B. Nardelli and J. Bernholc, *Physical Review B*, 2005, **72**, 115210.
23 J. Curie and P. Curie, *Compt. Makes*, 1881, **93**, 1137–1140.
24 X.-h. Du, J. Zheng, U. Belegundu and K. Uchino, *Applied Physics Letters*, 1998, **72**, 2421–2423.
25 S. Huang, J. Chang, L. Lu, F. Liu, Z. Ye and X. Cheng, *Materials Research Bulletin*, 2006, **41**, 291–297.
26 M. Ozgul, K. Takemura, S. Trolier-McKinstry and C. A. Randall, *Journal of Applied Physics*, 2001, **89**, 5100–5106.
27 W. P. Mason, *The Journal of the Acoustical Society of America*, 1981, **70**, 1561–1566.
28 I. Donald, *Ultrasound in medicine & biology*, 1974, **1**, 109–117.
29 A. Manbachi and R. S. Cobbold, *Ultrasound*, 2011, **19**, 187–196.
30 W. B. Robertson, *J. Chem. Educ*, 1967, **44**, 460.
31 L. Rozenberg, *Physical Principles of Ultrasonic Technology*, Springer, 1973, pp. 270–318.
32 N. Dam, *Non-contact ultrasonic micromeasurement system*, 1999, US Patent 5,880,364.
33 D. Yang, *Ultrasonic range finder*, 2008, US Patent 7,330,398.
34 S. Saadon and O. Sidek, *Energy Conversion and Management*, 2011, **52**, 500–504.
35 M. K. Kurosawa, O. Kodaira, Y. Tsuchitoi and T. Higuchi, *IEEE Transactions on Ultrasonics, Ferroelectrics, and Frequency Control*, 1998, **45**, 1188–1195.
36 B. Watson, J. Friend and L. Yeo, *Sensors and Actuators A: Physical*, 2009, **152**, 219–233.
37 J. Friend, K. Nakamura and S. Ueha, *IEEE/ASME Transactions on Mechatronics*, 2004, **9**, 467–473.
38 S. Tonami, A. Nishikata and Y. Shimizu, *Japanese Journal of Applied Physics*, 1995, **34**, 2664.
39 Y. V. Gulyaev, *IEEE Transactions on Ultrasonics, Ferroelectrics, and Frequency Control*, 1998, **45**, 935–938.
40 F. Martin, *Electronics Letters*, 2002, **38**, 941–942.
41 V. L. Strashilov and V. M. Yantchev, *IEEE Transactions on Ultrasonics, Ferroelectrics, and Frequency Control*, 2005, **52**, 812–821.
42 S. Collingon, O. Manor and J. Friend, *Advanced Functional Materials*, 2017, 1704359.
43 B. Jaffe, R. Roth and S. Marzullo, *Journal of Applied Physics*, 1954, **25**, 809–810.
44 I. Bretos, R. Jiménez, J. Garcïa-López, L. Pardo and M. L. Calzada, *Chemistry of Materials*, 2008, **20**, 5731–5733.
45 *95/EC of the European Parliament and of the Council of 27 January 2003 on the restriction of the use of certain hazardous substances in electrical and electronic equipment*, Directive, EU, 2002.
46 Y. Saito, H. Takao, T. Tani, T. Nonoyama, K. Takatori, T. Homma, T. Nagaya and M. Nakamura, *Nature*, 2004, **432**, 84–87.
47 K. Uchino and S. Hirose, *IEEE Transactions on Ultrasonics, ferroelectrics, and frequency control*, 2001, **48**, 307–321.
48 S. Jyomura, K. Nagatsuma and H. Takeuchi, *Journal of Applied Physics*, 1981, **52**, 4472–4478.
49 R. N. Thurston, A. D. Pierce and E. P. Papadakis, *Reference for Modern Instrumentation, Techniques, and Technology: Ultrasonic Instruments and Devices I: Ultrasonic Instruments and Devices I*, Academic Press, 1998, vol. 23.
50 R. Williamson, Ultrasonics Symposium, 1977, 1977, pp. 460–468.
51 C. Hartmann, *Rayleigh-Wave Theory and Application*, Springer, 1985, pp. 238–253.
52 I. M. Mason and E. A. Ash, *Journal of Applied Physics*, 1971, **42**, 5343–5351.
53 A. Takayanagi, K. Yamanouchi and K. Shibayama, *Applied Physics Letters*, 1970, **17**, 225–227.
54 A. Slobodnik and E. Conway, *Electronics Letters*, 1970, **6**, 171–173.
55 K. Shibayama, K. Yamanouchi, H. Sato and T. Meguro, *Proceedings of the IEEE*, 1976, **64**, 595–597.
56 C. K. Campbell, *Proceedings of the IEEE*, 1989, **77**, 1453–1484.
57 D. Ciplys and R. Rimeika, *Ultrasound*, 2014, **33**, 14–20.
58 V. Soluch and M. Lysakowska, *IEEE Transactions on Ultrasonics, Ferroelectrics, and Frequency Control*, 2005, **52**, 145–147.
59 F. S. Hickernell, *Physical Acoustics*, 1999, **24**, 135–207.
60 C. K. Campbell, *IEEE Transactions on Ultrasonics, Ferroelectrics, and Frequency Control*, 1995, **42**, 883–888.
61 J. Hechner and W. Soluch, *Sensors and Actuators B: Chemical*, 2005, **111**, 436–440.
62 A. Riaud, J.-L. Thomas, E. Charron, A. Bussonnière, O. B. Matar and M. Baudoin, *Physical Review Applied*, 2015, **4**, 034004.
63 M. Kurosawa, M. Takahashi and T. Higuchi, *IEEE Transactions on Ultrasonics, Ferroelectrics, and Frequency Control*, 1996, **43**, 901–906.
64 F. Guo, P. Li, J. B. French, Z. Mao, H. Zhao, S. Li, N. Nama, J. R. Fick, S. J. Benkovic and T. J. Huang, *Proceedings of the National Academy of Sciences*, 2015, **112**, 43–48.
65 C. Devendran, N. R. Gunasekara, D. J. Collins and A. Neild, *RSC Advances*, 2016, **6**, 5856–5864.
66 M. Gasparetti, G. M. Revel and E. P. Tomasini, Third International Conference on Vibration Measurements by Laser Techniques: Advances and Applications, 1998, pp. 317–327.
67 P. Castellini, M. Martarelli and E. Tomasini, *Mechanical Sys-*

tems and Signal Processing, 2006, **20**, 1265–1285.
68 S. Rothberg, M. Allen, P. Castellini, D. Di Maio, J. Dirckx, D. Ewins, B. J. Halkon, P. Muyshondt, N. Paone, T. Ryan *et al.*, *Optics and Lasers in Engineering*, 2016.
69 P. Castellini and C. Santolini, Second International Conference on Vibration Measurements by Laser Techniques: Advances and Applications, 1996, pp. 186–194.
70 A. Barker, P. Jaeger and D. E. Oliver, *Stress and Vibration: Recent Developments in Industrial Measurement and Analysis*, 1989, **1084**, 293–299.
71 L. Zhu, K. Hallamasek and D. Bogy, *IEEE Transactions on Magnetics*, 1988, **24**, 2739–2741.
72 J. M. Sabatier and N. Xiang, AeroSense'99, 1999, pp. 215–222.
73 R. White, *Journal of Physics E: Scientific Instruments*, 1985, **18**, 790.
74 R. Herdier, D. Jenkins, E. Dogheche, D. Rèmiens and M. Sulc, *Review of Scientific Instruments*, 2006, **77**, 093905.
75 M. Miansari and J. R. Friend, *Advanced Functional Materials*, 2016, **26**, 7861–7872.
76 J. E. Sader and J. R. Friend, *Review of Scientific Instruments*, 2014, **85**, 116101.
77 J. Friend and L. Yeo, *Biomicrofluidics*, 2010, **4**, 026501.
78 J. Vanherzeele, M. Brouns, P. Castellini, P. Guillaume, M. Martarelli, D. Ragni, E. P. Tomasini and S. Vanlanduit, *Optics and lasers in engineering*, 2007, **45**, 19–26.
79 J. Blamey, L. Y. Yeo and J. R. Friend, *Langmuir*, 2013, **29**, 3835–3845.
80 T. Tachizaki, T. Muroya, O. Matsuda, Y. Sugawara, D. H. Hurley and O. B. Wright, *Review of Scientific Instruments*, 2006, **77**, 043713.
81 G. Siegmund, Proc. SPIE, 2008, pp. 70980Y–1.
82 L. Yarovoi and G. Siegmund, *Measurement Science and Technology*, 2004, **15**, 2150.
83 B. J. Halkon and S. Rothberg, *Measurement science and technology*, 2003, **14**, 382.
84 J. Poittevin, F. Gautier, C. Pézerat and P. Picart, *Optical Engineering*, 2016, **55**, 121717–121717.
85 M. Leclercq, P. Picart, G. Penelet and V. Tournat, *Journal of Applied Physics*, 2017, **121**, 045112.
86 T. Cacace, M. Paturzo, P. Memmolo, M. Vassalli, P. Ferraro, M. Fraldi and G. Mensitieri, *Optics Express*, 2017, **25**, 17746–17752.
87 C. kai Luo, P. Gudem and J. Buckwalter, *IEEE Transactions on Microwave Theory and Techniques*, 2016, **64**, 1110–1121.
88 C. Campbell, *Surface acoustic wave devices for mobile and wireless communications*, Academic Press, New York, New York USA, 1998.
89 H. Nakahata, S. Fujii, K. Higaki, A. Hachigo, H. Kitabayashi, S. Shikata and N. Fujimori, *Semiconductor science and technology*, 2003, **18**, S96.
90 D. Morgan, *Surface acoustic wave filters: With applications to electronic communications and signal processing*, Academic Press, Amsterdam, the Netherlands, Second edition edn, 2010.
91 T. Nishihara, T. Yokoyama, T. Miyashita and Y. Satoh, Ultrasonics Symposium, Proceedings, 2002, pp. 969–972.
92 A. R. Rezk, J. R. Friend and L. Y. Yeo, *Lab on a Chip*, 2014, **14**, 1802–5.
93 J. Nam and C. S. Lim, *Lab on a Chip*, 2016, **16**, 3750–3755.
94 A. Winkler, P. Bergelt, L. Hillemann and S. Menzel, *Open Journal of Acoustics*, 2016, **6**, 23–33.
95 A. Winkler, S. Harazim, D. Collins, R. Brünig, H. Schmidt and S. Menzel, *Biomedical Microdevices*, 2017, **19**, 9.
96 R. J. Shilton, V. Mattoli, M. Travagliati, M. Agostini, A. Desii, F. Beltram and M. Cecchini, *Advanced Functional Materials*, 2015, **25**, 5895–5901.
97 M. J. Madou, *Fundamentals of microfabrication: the science of miniaturization*, CRC press, 2002.
98 M. B. Dentry, L. Y. Yeo and J. R. Friend, *Physical Review E*, 2014, **89**, 013203.
99 M. Pekarcikova, M. Hofmann, S. Menzel, H. Schrnidt, T. Gemming and K. Wetzig, *IEEE Transactions on Ultrasonics, Ferroelectrics, and Frequency Control*, 2005, **52**, 911–917.
100 H. Wohltjen, *Sensors and Actuators*, 1984, **5**, 307–325.
101 Z. Ma, A. J. Teo, S. H. Tan, Y. Ai and N.-T. Nguyen, *Micromachines*, 2016, **7**, 216.
102 D. Morgan, *Surface acoustic wave filters*, Elsevier, Amsterdam, the Netherlands, 2007.
103 J. Green and G. Kino, *IEEE Transactions on Sonics and Ultrasonics*, 1983, **30**, 43–50.
104 Y. Nakagawa, Ultrasonics Symposium, 1991. Proceedings., IEEE 1991, 1991, pp. 255–258.
105 T. Marynowski, Ultrasonics Symposium, 1982, pp. 160–165.
106 J. Green, G. Kino and B. Khuri-Yakub, Ultrasonics Symposium, 1980, pp. 69–73.
107 J. Z. Wilcox and R. E. Brooks, *Journal of Applied Physics*, 1985, **58**, 1148–1159.
108 M. de Lima Jr, R. Hey, J. Stotz and P. Santos, *Applied Physics Letters*, 2004, **84**, 2569–2571.
109 M. S. Kharusi and G. W. Farnell, *Proceedings of the IEEE*, 1972, **60**, 945–956.
110 M. Cohen, *Journal of Applied Physics*, 1967, **38**, 3821–3828.
111 S. R. Fang, S. Zhang and Z. F. Lu, *IEEE Transactions on Ultrasonics, Ferroelectrics, and Frequency Control*, 1989, **36**, 178–184.
112 T.-T. Wu, H.-T. Tang and Y.-Y. Chen, *Journal of Physics D: Applied Physics*, 2005, **38**, 2986.
113 T.-T. Wu, H.-T. Tang, Y.-Y. Chen and P.-L. Liu, *IEEE Transactions on Ultrasonics, Ferroelectrics, and Frequency Control*, 2005, **52**, 1384–1392.
114 R. Shilton, M. K. Tan, L. Y. Yeo and J. R. Friend, *Journal of Applied Physics*, 2008, **104**, 014910.
115 V. Laude, D. Gérard, N. Khelfaoui, C. F. Jerez-Hanckes, S. Benchabane and A. Khelif, *Applied Physics Letters*, 2008, **92**, 094104.
116 A. Riaud, M. Baudoin, J.-L. Thomas and O. B. Matar, *IEEE*

Transactions on Ultrasonics, Ferroelectrics, and Frequency Control, 2016, **63**, 1601–1607.
117 M. Tanter, J.-L. Thomas and M. Fink, *The Journal of the Acoustical Society of America*, 2000, **108**, 223–234.
118 A. Riaud, M. Baudoin, O. B. Matar, L. Becerra and J.-L. Thomas, *Physical Review Applied*, 2017, **7**, 024007.
119 M. K. Tan, J. R. Friend and L. Y. Yeo, *Applied Physics Letters*, 2007, **91**, 224101.
120 R. Rambach, J. Taiber, C. Scheck, C. Meyer, J. Reboud, J. Cooper and T. Franke, *Scientific Reports*, 2016, **6**, year.
121 M. K. Tan, J. R. Friend and L. Y. Yeo, *Lab on a Chip*, 2007, **7**, 618.
122 H. Li, J. R. Friend and L. Y. Yeo, *Biomedical Microdevices*, 2007, **9**, 647–656.
123 R. Arzt, E. Salzmann and K. Dransfeld, *Applied Physics Letters*, 1967, **10**, 165–167.
124 R. P. Hodgson, M. Tan, L. Yeo and J. Friend, *Applied Physics Letters*, 2009, **94**, 024102.
125 S. M. Langelier, L. Y. Yeo and J. Friend, *Lab on a Chip*, 2012, **12**, 2970–2976.
126 J. Lighthill, *Journal of sound and vibration*, 1978, **61**, 391–418.
127 S. Shiokawa, Y. Matsui and T. Moriizumi, *Japanese Journal of Applied Physics*, 1989, **28**, 126.
128 H. Schlichting, *Phys. Z*, 1932, **33**, 327–335.
129 A. R. Rezk, O. Manor, L. Y. Yeo and J. R. Friend, Proc. R. Soc. A, 2014, p. 20130765.
130 L. V. King, Proceedings of the Royal Society of London A: Mathematical, Physical and Engineering Sciences, 1934, pp. 212–240.
131 K. Yosioka and Y. Kawasima, *Acta Acustica united with Acustica*, 1955, **5**, 167–173.
132 H. Bruus, *Lab on a Chip*, 2012, **12**, 1014–1021.
133 F. Nadal and E. Lauga, *Physics of Fluids*, 2014, **26**, 082001.
134 P. L. Marston, *The Journal of the Acoustical Society of America*, 2017, **142**, 3358–3361.
135 B.-T. Chu and R. E. Apfel, *The Journal of the Acoustical Society of America*, 1982, **72**, 1673–1687.
136 L. A. Crum, *The Journal of the Acoustical Society of America*, 1975, **57**, 1363–1370.
137 M. Weiser, R. Apfel and E. Neppiras, *Acta Acustica united with Acustica*, 1984, **56**, 114–119.
138 B. Hammarström, T. Laurell and J. Nilsson, *Lab on a Chip*, 2012, **12**, 4296–4304.
139 P. Rogers and A. Neild, *Lab on a Chip*, 2011, **11**, 3710–3715.
140 A. Huang, M. Miansari and J. Friend, *Applied Physics Letters*, in review.
141 G. Kwon, D. Panchanathan, S. R. Mahmoudi, M. A. Gondal, G. H. McKinley and K. K. Varanasi, *Nature Communications*, 2017, **8**, year.
142 Y.-H. Lin and G.-B. Lee, *Biosensors and Bioelectronics*, 2008, **24**, 572–578.
143 S.-B. Huang, M.-H. Wu, Y.-H. Lin, C.-H. Hsieh, C.-L. Yang, H.-C. Lin, C.-P. Tseng and G.-B. Lee, *Lab on a Chip*, 2013, **13**, 1371–1383.
144 S. Haeberle and R. Zengerle, *Lab on a Chip*, 2007, **7**, 1094–1110.
145 A. Wixforth, C. Strobl, C. Gauer, A. Toegl, J. Scriba and Z. v. Guttenberg, *Analytical and bioanalytical chemistry*, 2004, **379**, 982–991.
146 R. Raghavan, J. R. Friend and L. Y. Yeo, *Microfluidics and Nanofluidics*, 2010, **8**, 73–84.
147 W. Nyborg, in *Physical Acoustics*, ed. W. P. Mason, Academic Press, New York, NY, 1965, vol. 2B, ch. Acoustic Streaming, pp. 265–331.
148 S. Shiokawa, Y. Matsui and T. Ueda, *Japanese Journal of Applied Physics*, 1990, **29**, 137.
149 M. Alghane, B. Chen, Y. Q. Fu, Y. Li, J. Luo and A. Walton, *Journal of micromechanics and Microengineering*, 2010, **21**, 015005.
150 J. Vanneste and O. Bühler, Proceedings of the Royal Society of London A: Mathematical, Physical and Engineering Sciences, 2010, p. rspa20100457.
151 A. R. Rezk, L. Y. Yeo and J. R. Friend, *Langmuir*, 2014, **30**, 11243–11247.
152 A. Riaud, M. Baudoin, J.-L. Thomas and O. Bou Matar, *Physical Review*, 2014, **90**, 8.
153 R. Shilton, M. Tan, L. Yeo and J. Friend, *Proceedings - IEEE Ultrasonics Symposium*, 2008, 930–933.
154 A. Riaud, M. Baudoin, O. Bou Matar, J.-L. Thomas and P. Brunet, *Journal of Fluid Mechanics*, 2017.
155 R. J. Shilton, L. Y. Yeo and J. R. Friend, *Sensors and Actuators B: Chemical*, 2011, **160**, 1565–1572.
156 R. J. Shilton, M. Travagliati, F. Beltram and M. Cecchini, *Advanced Materials*, 2014, **26**, 4941–4946.
157 C.-M. Ho, Micro Electro Mechanical Systems, 2001 (MEMS 2001). The 14th IEEE International Conference on, 2001, pp. 375–384.
158 A. Kundt and O. Lehmann, *Annalen der Physik*, 1874, **229**, 1–12.
159 G. Destgeer, H. Cho, B. H. Ha, J. H. Jung, J. Park and H. J. Sung, *Lab on a Chip*, 2016, **16**, 660–667.
160 R. Wilson, J. Reboud, Y. Bourquin, S. L. Neale, Y. Zhang and J. M. Cooper, *Lab on a Chip*, 2011, **11**, 323–328.
161 G. Destgeer, B. Ha, J. Park and H. J. Sung, *Analytical Chemistry*, 2016, **88**, 3976–3981.
162 C. Wood, S. Evans, J. Cunningham, R. O'Rorke, C. Wälti and A. Davies, *Applied Physics Letters*, 2008, **92**, 044104.
163 P. R. Rogers, J. R. Friend and L. Y. Yeo, *Lab on a Chip*, 2010, **10**, 2979–2985.
164 Y. Bourquin, J. Reboud, R. Wilson and J. M. Cooper, *Lab on a Chip*, 2010, **10**, 1898–1901.
165 Y. Bourquin, A. Syed, J. Reboud, L. C. Ranford-Cartwright, M. P. Barrett and J. M. Cooper, *Angewandte Chemie*, 2014, **126**, 5693–5696.
166 J. L. Garcia-Cordero and Z. H. Fan, *Lab on a Chip*, 2017, **17**, 2150–2166.

167 D. Mampallil, J. Reboud, R. Wilson, D. Wylie, D. R. Klug and J. M. Cooper, *Soft Matter*, 2015, **11**, 7207–7213.

168 R.-Z. Lin and H.-Y. Chang, *Biotechnology Journal*, 2008, **3**, 1172–1184.

169 L. Alhasan, A. Qi, A. Al-Abboodi, A. Rezk, P. P. Chan, C. Iliescu and L. Y. Yeo, *ACS Biomaterials Science & Engineering*, 2016, **2**, 1013–1022.

170 Y. Kurashina, K. Takemura and J. Friend, *Lab on a Chip*, 2017, **17**, 876–886.

171 F. G. Strobl, D. Breyer, P. Link, A. A. Torrano, C. Bräuchle, M. F. Schneider and A. Wixforth, *Beilstein Journal of Nanotechnology*, 2015, **6**, 414–419.

172 N. Sivanantha, C. Ma, D. J. Collins, M. Sesen, J. Brenker, R. L. Coppel, A. Neild and T. Alan, *Applied Physics Letters*, 2014, **105**, 103704.

173 A. Bussonnière, Y. Miron, M. Baudoin, O. B. Matar, M. Grandbois, P. Charette and A. Renaudin, *Lab on a Chip*, 2014, **14**, 3556–3563.

174 D. Taller, K. Richards, Z. Slouka, S. Senapati, R. Hill, D. B. Go and H.-C. Chang, *Lab on a Chip*, 2015, **15**, 1656–1666.

175 Z. Guttenberg, H. Müller, H. Habermüller, A. Geisbauer, J. Pipper, J. Felbel, M. Kielpinski, J. Scriba and A. Wixforth, *Lab on a Chip*, 2005, **5**, 308–317.

176 L. Gao and T. J. McCarthy, *Langmuir*, 2009, **25**, 14105–14115.

177 A. Wixforth, *Superlattices and Microstructures*, 2003, **33**, 389–396.

178 A. Renaudin, P. Tabourier, V. Zhang, J. C. Camart and C. Druon, *Sensors and Actuators, B: Chemical*, 2006, **113**, 389–397.

179 M. Baudoin, P. Brunet, O. Bou Matar and E. Herth, *Applied Physics Letters*, 2012, **100**, 154102.

180 P. Brunet, M. Baudoin, O. B. Matar and F. Zoueshtiagh, *Physical Review E - Statistical, Nonlinear, and Soft Matter Physics*, 2010, **81**, 1–8.

181 A. R. Rezk, O. Manor, J. R. Friend and L. Y. Yeo, *Nature communications*, 2012, **3**, 1167.

182 M. Morozov and O. Manor, *Journal of fluid mechanics*, 2017, **810**, 307–322.

183 M. Travagliati, G. D. Simoni, M. Lazzarini and V. Piazza, *Lab on a Chip*, 2012, **12**, 2621–2624.

184 Y. Ai and B. L. Marrone, *Microfluidics and Nanofluidics*, 2012, **13**, 715–722.

185 S. Collignon, J. Friend and L. Yeo, *Lab on a Chip*, 2015, **15**, 1942–1951.

186 A. Bussonniere, M. Baudoin, P. Brunet and O. B. Matar, *Physical Review E*, 2016, **93**, 053106.

187 K. Mullis, F. Faloona, S. Scharf, R. Saiki, G. Horn and H. Erlich, Cold Spring Harbor Symposia on Quantitative Biology, 1986, pp. 263–273.

188 L. Y. Yeo, H.-C. Chang, P. P. Chan and J. R. Friend, *small*, 2011, **7**, 12–48.

189 J. Dong, T. Uemura, Y. Shirasaki and T. Tateishi, *Biomaterials*, 2002, **23**, 4493–4502.

190 V. Maquet, D. Martin, B. Malgrange, R. Franzen, J. Schoenen, G. Moonen and R. Jérôme, *Journal of Biomedical Materials Research Part A*, 2000, **52**, 639–651.

191 H. Li, J. R. Friend and L. Y. Yeo, *Biomaterials*, 2007, **28**, 4098–4104.

192 M. Bok, H. Li, L. Y. Yeo and J. R. Friend, *Biotechnology and Bioengineering*, 2009, **103**, 387–401.

193 J. Eggers, *Reviews of modern physics*, 1997, **69**, 865.

194 M. K. Tan, J. R. Friend and L. Y. Yeo, *Physical Review Letters*, 2009, **103**, year.

195 J. Wang, H. Hu, A. Ye, J. Chen and P. Zhang, *Sensors and Actuators, A: Physical*, 2016, **238**, 1–7.

196 T. Tuladhar and M. Mackley, *Journal of Non-Newtonian Fluid Mechanics*, 2008, **148**, 97–108.

197 L. E. Rodd, T. P. Scott, J. J. Cooper-White and G. H. McKinley, *Applied Rheology*, 2004.

198 P. Bhattacharjee, A. McDonnell, R. Prabhakar, L. Yeo and J. Friend, *New Journal of Physics*, 2011, **13**, 023005.

199 A. G. McDonnell, T. C. Gopesh, J. Lo, M. O'Bryan, L. Y. Yeo, J. R. Friend and R. Prabhakar, *Soft Matter*, 2015, **11**, 4658–4668.

200 A. G. McDonnell, N. N. Jason, L. Y. Yeo, J. R. Friend, W. Cheng and R. Prabhakar, *Soft matter*, 2015, **11**, 8076–8082.

201 R. J. Lang, *The Journal of the Acoustical Society of America*, 1962, **34**, 6–8.

202 W. Eisenmenger, *Acta Acustica united with Acustica*, 1959, **9**, 327–340.

203 T. B. Benjamin and F. Ursell, Proceedings of the Royal Society of London A: Mathematical, Physical and Engineering Sciences, 1954, pp. 505–515.

204 M. Faraday, *Philosophical Transactions of the Royal Society of London*, 1831, **121**, 299–340.

205 M. Kurosawa, T. Watanabe, A. Hutami and T. Higuchi, *IEEE*, 1995, 25–30.

206 M. Kurosawa, A. Futami and T. Higuchi, Solid State Sensors and Actuators, 1997. TRANSDUCERS'97 Chicago., 1997 International Conference on, 1997, pp. 801–804.

207 A. Qi, L. Y. Yeo and J. R. Friend, *Physics of Fluids*, 2008, **20**, 074103.

208 M. K. Tan, J. R. Friend, O. K. Matar and L. Y. Yeo, *Physics of Fluids*, 2010, **22**, 1–22.

209 D. J. Collins, O. Manor, A. Winkler, H. Schmidt, J. R. Friend and L. Y. Yeo, *Physical Review E - Statistical, Nonlinear, and Soft Matter Physics*, 2012, **86**, 1–9.

210 A. Rajapaksa, A. Qi, L. Y. Yeo, R. Coppel and J. R. Friend, *Lab Chip*, 2014, **14**, 1858–1865.

211 A. R. Rezk, J. K. Tan and L. Y. Yeo, *Advanced Materials Communication*, 2016, **28**, 1970–1975.

212 A. Winkler, S. Harazim, S. Menzel and H. Schmidt, *Lab on a Chip*, 2015, **15**, 3793–3799.

213 A. Winkler, R. Brünig, C. Faust, R. Weser and H. Schmidt, *Sensors & Actuators A*, 2016, **247**, 259–268.

214 C. J. Brinker, Y. Lu, A. Sellinger, H. Fan *et al.*, *Advanced ma-*

terials, 1999, **11**, 579–585.
215 J. R. Friend, L. Y. Yeo, D. R. Arifin and A. Mechler, *Nanotechnology*, 2008, **19**, 145301–6.
216 M. Bognitzki, W. Czado, T. Frese, A. Schaper, M. Hellwig, M. Steinhart, A. Greiner, J. H. Wendorff *et al.*, *Advanced Materials*, 2001, **13**, 70–72.
217 S. Megelski, J. S. Stephens, D. B. Chase and J. F. Rabolt, *Macromolecules*, 2002, **35**, 8456–8466.
218 K. H. Choi, H. B. Kim, K. Ali, M. Sajid, G. U. Siddiqui, D. E. Chang, H. C. Kim, J. B. Ko, H. W. Dang and Y. H. Doh, *Scientific Reports*, 2015, **5**, year.
219 A. Kirchner, A. Winkler, S. M. Menzel, B. Holzapfel and R. Huhne, *IEEE Transactions on Applied Superconductivity*, 2016, **26**, 1–4.
220 T. Vuong, A. Qi, M. Muradoglu, B.-P. Cheong, O. Liew, C. Ang, J. Fu, L. Yeo, J. Friend and T. Ng, *Soft Matter*, 2013, **9**, 3631–3639.
221 K. M. Ang, L. Y. Yeo, J. R. Friend, Y. M. Hung and M. K. Tan, *Journal of Aerosol Science*, 2015, **79**, 48–60.
222 M. Alvarez, J. Friend and L. Y. Yeo, *Nanotechnology*, 2008, **19**, 455103.
223 A. Qi, J. R. Friend, L. Y. Yeo, D. A. Morton, M. P. McIntosh and L. Spiccia, *Lab on a Chip*, 2009, **9**, 2184–2193.
224 C. Cortez-Jugo, A. Qi, A. Rajapaksa, J. R. Friend and L. Y. Yeo, *Biomicrofluidics*, 2015, **9**, 052603.
225 A. E. Rajapaksa, J. J. Ho, A. Qi, R. Bischof, T.-H. Nguyen, M. Tate, D. Piedrafita, M. P. McIntosh, L. Y. Yeo, E. Meeusen, C. L. Ross and J. R. Friend, *Respiratory Research*, 2014, **15**, 60.
226 A. Qi, L. Yeo, J. Friend and J. Ho, *Lab on a Chip*, 2010, **10**, 470–476.
227 S. R. Heron, R. Wilson, S. A. Shaffer, D. R. Goodlett and J. M. Cooper, *Analytical Chemistry*, 2010, **82**, 3985–3989.
228 J. Ho, M. K. Tan, D. B. Go, L. Y. Yeo, J. R. Friend and H.-C. Chang, *Analytical Chemistry*, 2011, **83**, 3260–3266.
229 Y. Huang, S. H. Yoon, S. R. Heron, C. D. Masselon, J. S. Edgar, F. Tureček and D. R. Goodlett, *Journal of The American Society for Mass Spectrometry*, 2012, **23**, 1062–1070.
230 Y. Huang, S. R. Heron, A. M. Clark, J. S. Edgar, S. H. Yoon, D. Kilgour, F. Turecek, A. Aliseda and D. R. Goodlett, *Journal of Mass Spectrometry*, 2016, **51**, 424–429.
231 K. Länge, B. E. Rapp and M. Rapp, *Analytical and bioanalytical chemistry*, 2008, **391**, 1509–1519.
232 M.-I. Rocha-Gaso, C. March-Iborra, Á. Montoya-Baides and A. Arnau-Vives, *Sensors*, 2009, **9**, 5740–5769.
233 E. Howe and G. Harding, *Biosensors and Bioelectronics*, 2000, **15**, 641–649.
234 E. Berkenpas, P. Millard and M. P. Da Cunha, *Biosensors and Bioelectronics*, 2006, **21**, 2255–2262.
235 J. T. Baca, V. Severns, D. Lovato, D. W. Branch and R. S. Larson, *Sensors*, 2015, **15**, 8605–8614.
236 S. U. Senveli, Z. Ao, S. Rawal, R. H. Datar, R. J. Cote and O. Tigli, *Lab on a Chip*, 2016, **16**, 163–171.
237 J. Sakong, H. Roh and Y. Roh, *Japanese Journal of Applied Physics*, 2007, **46**, 4729.
238 H.-L. Cai, Y. Yang, X. Chen, M. A. Mohammad, T.-X. Ye, C.-R. Guo, L.-T. Yi, C.-J. Zhou, J. Liu and T.-L. Ren, *Biosensors and Bioelectronics*, 2015, **71**, 261–268.
239 J. Lee, Y.-S. Choi, Y. Lee, H. J. Lee, J. N. Lee, S. K. Kim, K. Y. Han, E. C. Cho, J. C. Park and S. S. Lee, *Analytical Chemistry*, 2011, **83**, 8629–8635.
240 B. H. Ha, K. S. Lee, G. Destgeer, J. Park, J. S. Choung, J. H. Jung, J. H. Shin and H. J. Sung, *Scientific Reports*, 2015, **5**, year.
241 M. C. Jo and R. Guldiken, *Microelectronic Engineering*, 2014, **113**, 98–104.
242 K. Sritharan, C. J. Strobl, M. F. Schneider, A. Wixforth and Z. v. Guttenberg, *Applied Physics Letters*, 2006, **88**, 054102.
243 W.-K. Tseng, J.-L. Lin, W.-C. Sung, S.-H. Chen and G.-B. Lee, *Journal of Micromechanics and Microengineering*, 2006, **16**, 539.
244 M. C. Jo and R. Guldiken, *Sensors and Actuators A: Physical*, 2013, **196**, 1–7.
245 T.-D. Luong, V.-N. Phan and N.-T. Nguyen, *Microfluidics and nanofluidics*, 2011, **10**, 619–625.
246 M. Tan, L. Yeo and J. Friend, *EPL (Europhysics Letters)*, 2009, **87**, 47003.
247 A. R. Rezk, A. Qi, J. R. Friend, W. H. Li and L. Y. Yeo, *Lab on a Chip*, 2012, **12**, 773–779.
248 J. C. Rife, M. I. Bell, J. S. Horwitz, M. N. Kabler, R. Auyeung and W. J. Kim, *Sensors and Actuators A: Physical*, 2000, **86**, 135–140.
249 Z. Yang, S. Matsumoto, H. Goto, M. Matsumoto and R. Maeda, *Sensors and Actuators A: Physical*, 2001, **93**, 266–272.
250 G. G. Yaralioglu, I. O. Wygant, T. C. Marentis and B. T. Khuri-Yakub, *Analytical Chemistry*, 2004, **76**, 3694–3698.
251 S. Oberti, A. Neild and T. W. Ng, *Lab on a Chip*, 2009, **9**, 1435–1438.
252 H. Van Phan, M. B. Coşkun, M. Şeşen, G. Pandraud, A. Neild and T. Alan, *Lab on a Chip*, 2015, **15**, 4206–4216.
253 W. Cui, H. Zhang, H. Zhang, Y. Yang, M. He, H. Qu, W. Pang, D. Zhang and X. Duan, *Applied Physics Letters*, 2016, **109**, 253503.
254 S. O. Catarino, V. C. Pinto, P. J. Sousa, R. Lima, J. M. Miranda and G. Minas, Engineering in Medicine and Biology Society (EMBC), IEEE 38th Annual International Conference of the, 2016, pp. 5660–5663.
255 P. Marmottant and S. Hilgenfeldt, *Nature*, 2003, **423**, 153–156.
256 B. Rallabandi, C. Wang and S. Hilgenfeldt, *Journal of Fluid Mechanics*, 2014, **739**, 57–71.
257 S.-W. Ohl and C.-D. Ohl, *Handbook of Ultrasonics and Sonochemistry*, 2016, 99–135.
258 R. H. Liu, J. Yang, M. Z. Pindera, M. Athavale and P. Grodzinski, *Lab on a Chip*, 2002, **2**, 151–157.
259 R. H. Liu, R. Lenigk, R. L. Druyor-Sanchez, J. Yang and P. Grodzinski, *Analytical Chemistry*, 2003, **75**, 1911–1917.

260 A. R. Tovar and A. P. Lee, *Lab on a Chip*, 2009, **9**, 41–43.
261 D. Ahmed, X. Mao, B. K. Juluri and T. J. Huang, *Microfluidics and nanofluidics*, 2009, **7**, 727.
262 S. Wang, Z. Jiao, X. Huang, C. Yang and N.-T. Nguyen, *Microfluidics and nanofluidics*, 2009, **6**, 847–852.
263 D. Ahmed, X. Mao, J. Shi, B. K. Juluri and T. J. Huang, *Lab on a Chip*, 2009, **9**, 2738–2741.
264 A. Ozcelik, D. Ahmed, Y. Xie, N. Nama, Z. Qu, A. A. Nawaz and T. J. Huang, *Analytical Chemistry*, 2014, **86**, 5083.
265 N. Bertin, T. A. Spelman, T. Combriat, H. Hue, O. Stéphan, E. Lauga and P. Marmottant, *Lab on a Chip*, 2017, **17**, 1515–1528.
266 S. Orbay, A. Ozcelik, J. Lata, M. Kaynak, M. Wu and T. J. Huang, *Journal of Micromechanics and Microengineering*, 2016, **27**, 015008.
267 T. Combriat, F. Mekki-Berrada, P. Thibault and P. Marmottant, *Physical Review Fluids*, 2018, **3**, 013602.
268 P.-H. Huang, Y. Xie, D. Ahmed, J. Rufo, N. Nama, Y. Chen, C. Y. Chan and T. J. Huang, *Lab on a Chip*, 2013, **13**, 3847–3852.
269 P.-H. Huang, M. Ian Lapsley, D. Ahmed, Y. Chen, L. Wang and T. Jun Huang, *Applied Physics Letters*, 2012, **101**, 141101.
270 M. Ovchinnikov, J. Zhou and S. Yalamanchili, *The Journal of the Acoustical Society of America*, 2014, **136**, 22–29.
271 N. Nama, P.-H. Huang, T. J. Huang and F. Costanzo, *Biomicrofluidics*, 2016, **10**, 024124.
272 M. Cecchini, S. Girardo, D. Pisignano, R. Cingolani and F. Beltram, *Applied Physics Letters*, 2008, **92**, 104103.
273 L. Masini, M. Cecchini, S. Girardo, R. Cingolani, D. Pisignano and F. Beltram, *Lab on a Chip*, 2010, **10**, 1997–2000.
274 R. J. Shilton, M. Travagliati, F. Beltram and M. Cecchini, *Applied Physics Letters*, 2014, **105**, 074106.
275 S. Ito, M. Sugimoto, Y. Matsui and J. Kondoh, *Japanese Journal of Applied Physics*, 2007, **46**, 4718.
276 M. K. Tan, L. Y. Yeo and J. R. Friend, *Applied Physics Letters*, 2010, **97**, 234106.
277 L. Schmid, A. Wixforth, D. A. Weitz and T. Franke, *Microfluidics and Nanofluidics*, 2012, **12**, 229–235.
278 T. Hasegawa, J. Friend, K. Nakamura and S. Ueha, *Japanese Journal of Applied Physics*, 2005, **44**, 4658.
279 B. Ma, S. Liu, Z. Gan, G. Liu, X. Cai, H. Zhang and Z. Yang, *Microfluidics and Nanofluidics*, 2006, **2**, 417–423.
280 S. M. Langelier, D. S. Chang, R. I. Zeitoun and M. A. Burns, *Proceedings of the National Academy of Sciences*, 2009, **106**, 12617–12622.
281 A. Tovar, M. Patel and A. P. Lee, BiOS, 2010, pp. 757402–757402.
282 A. R. Tovar, M. V. Patel and A. P. Lee, *Microfluidics and Nanofluidics*, 2011, **10**, 1269–1278.
283 M. V. Patel, I. A. Nanayakkara, M. G. Simon and A. P. Lee, *Lab on a Chip*, 2014, **14**, 3860–3872.
284 W.-F. Fang and A. P. Lee, *Microfluidics and Nanofluidics*, 2015, **18**, 1265–1275.
285 P.-H. Huang, N. Nama, Z. Mao, P. Li, J. Rufo, Y. Chen, Y. Xie, C.-H. Wei, L. Wang and T. J. Huang, *Lab on a Chip*, 2014, **14**, 4319–4323.
286 Z. Wang and J. Zhe, *Lab on a Chip*, 2011, **11**, 1280–1285.
287 A. Barani, H. Paktinat, M. Janmaleki, A. Mohammadi, P. Mosaddegh, A. Fadaei-Tehrani and A. Sanati-Nezhad, *Biosensors and Bioelectronics*, 2016, **85**, 714–725.
288 M. Gedge and M. Hill, *Lab on a Chip*, 2012, **12**, 2998–3007.
289 J. Shi, X. Mao, D. Ahmed, A. Colletti and T. J. Huang, *Lab on a Chip*, 2008, **8**, 221–223.
290 Q. Zeng, H. Chan, X. Zhao and Y. Chen, *Microelectronic Engineering*, 2010, **87**, 1204–1206.
291 M. C. Jo and R. Guldiken, *Sensors and Actuators A: Physical*, 2012, **187**, 22–28.
292 J. Shi, S. Yazdi, S.-C. S. Lin, X. Ding, I.-K. Chiang, K. Sharp and T. J. Huang, *Lab on a Chip*, 2011, **11**, 2319–2324.
293 C. Witte, J. Reboud, R. Wilson, J. Cooper and S. Neale, *Lab on a Chip*, 2014, **14**, 4277–4283.
294 M. K. Tan, R. Tjeung, H. Ervin, L. Y. Yeo and J. Friend, *Applied Physics Letters*, 2009, **95**, 134101.
295 T. Franke, A. R. Abate, D. A. Weitz and A. Wixforth, *Lab on a Chip*, 2009, **9**, 2625–2627.
296 G. Destgeer, K. H. Lee, J. H. Jung, A. Alazzam and H. J. Sung, *Lab on a Chip*, 2013, **13**, 4210–4216.
297 Z. Ma, D. J. Collins and Y. Ai, *Analytical Chemistry*, 2016, **88**, 5316–5323.
298 Z. Ma, D. J. Collins, J. Guo and Y. Ai, *Analytical Chemistry*, 2016, **88**, 11844–11851.
299 S. Kapishnikov, V. Kantsler and V. Steinberg, *Journal of statistical mechanics: theory and experiment*, 2006, **2006**, P01012.
300 J. Shi, H. Huang, Z. Stratton, Y. Huang and T. J. Huang, *Lab on a Chip*, 2011, **9**, 317–326.
301 J. Nam, Y. Lee and S. Shin, *Microfluidics and nanofluidics*, 2011, **11**, 317–326.
302 G. Destgeer, B. H. Ha, J. Park, J. H. Jung, A. Alazzam and H. J. Sung, *Analytical Chemistry*, 2015, **87**, 4627–4632.
303 Z. Mao, Y. Xie, F. Guo, L. Ren, P.-H. Huang, Y. Chen, J. Rufo, F. Costanzo and T. J. Huang, *Lab on a Chip*, 2016, **16**, 515–524.
304 M. Wu, Z. Mao, K. Chen, H. Bachman, Y. Chen, J. Rufo, L. Ren, P. Li, L. Wang and T. J. Huang, *Advanced Functional Materials*, 2017, **27**, year.
305 R. Kishor, Z. Ma, S. Sreejith, Y. P. Seah, H. Wang, Y. Ai, Z. Wang, T.-T. Lim and Y. Zheng, *Sensors and Actuators B: Chemical*, 2017.
306 J. Park, J. H. Jung, G. Destgeer, H. Ahmed, K. Park and H. J. Sung, *Lab on a Chip*, 2017, **17**, 1031–1040.
307 J. Nam, H. Lim, D. Kim and S. Shin, *Lab on a Chip*, 2011, **11**, 3361–3364.
308 D. J. Collins, Z. Ma and Y. Ai, *Analytical Chemistry*, 2016, **88**, 5513–5522.
309 D. J. Collins, Z. Ma, J. Han and Y. Ai, *Lab on a Chip*, 2017, **17**, 91–103.
310 X. Ding, S.-C. S. Lin, M. I. Lapsley, S. Li, X. Guo, C. Y. Chan, I.-K. Chiang, L. Wang, J. P. McCoy and T. J. Huang, *Lab on a*

Chip, 2012, **12**, 4228–4231.
311 L. Schmid, D. A. Weitz and T. Franke, *Lab on a Chip*, 2014, **14**, 3710–3718.
312 L. Ren, Y. Chen, P. Li, Z. Mao, P.-H. Huang, J. Rufo, F. Guo, L. Wang, J. P. McCoy, S. J. Levine *et al.*, *Lab on a Chip*, 2015, **15**, 3870–3879.
313 D. J. Collins, A. Neild and Y. Ai, *Lab on a Chip*, 2016, **16**, 471–479.
314 J. P. Lata, F. Guo, J. Guo, P.-H. Huang, J. Yang and T. J. Huang, *Advanced Materials*, 2016, **28**, 8632–8638.
315 C. Wood, J. Cunningham, R. O'Rorke, C. Wälti, E. Linfield, A. Davies and S. Evans, *Applied Physics Letters*, 2009, **94**, 054101.
316 J. Shi, D. Ahmed, X. Mao, S.-C. S. Lin, A. Lawit and T. J. Huang, *Lab on a Chip*, 2009, **9**, 2890–2895.
317 R. O'Rorke, C. Wood, C. Wälti, S. Evans, A. Davies and J. Cunningham, *Journal of Applied Physics*, 2012, **111**, 094911.
318 X. Ding, J. Shi, S.-C. S. Lin, S. Yazdi, B. Kiraly and T. J. Huang, *Lab on a Chip*, 2012, **12**, 2491–2497.
319 D. J. Collins, C. Devendran, Z. Ma, J. W. Ng, A. Neild and Y. Ai, *Science Advances*, 2016, **2**, e1600089.
320 L. Tian, N. Martin, P. G. Bassindale, A. J. Patil, M. Li, A. Barnes, B. W. Drinkwater and S. Mann, *Nature communications*, 2016, **7**, year.
321 J. Hu and A. K. Santoso, *IEEE Transactions on Ultrasonics, Ferroelectrics, and Frequency Control*, 2004, **51**, 1499–1507.
322 J. Hu, J. Yang and J. Xu, *Applied Physics Letters*, 2004, **85**, 6042–6044.
323 N. D. Orloff, J. R. Dennis, M. Cecchini, E. Schonbrun, E. Rocas, Y. Wang, D. Novotny, R. W. Simmonds, J. Moreland, I. Takeuchi *et al.*, *Biomicrofluidics*, 2011, **5**, 044107.
324 X. Ding, S.-C. S. Lin, B. Kiraly, H. Yue, S. Li, I.-K. Chiang, J. Shi, S. J. Benkovic and T. J. Huang, *Proceedings of the National Academy of Sciences*, 2012, **109**, 11105–11109.
325 S. Tran, P. Marmottant and P. Thibault, *Applied Physics Letters*, 2012, **101**, 114103.
326 Y. Chen, S. Li, Y. Gu, P. Li, X. Ding, L. Wang, J. P. McCoy, S. J. Levine and T. J. Huang, *Lab on a Chip*, 2014, **14**, 924–930.
327 D. Baresch, J.-L. Thomas and R. Marchiano, *Phys. Rev. Lett.*, 2016, **116**, 024301.
328 D. Baresch, J.-L. Thomas and R. Marchiano, *Journal of Applied Physics*, 2013, **113**, 184901.
329 B. W. Drinkwater, *Lab on a Chip*, 2016, **16**, 2360–2375.
330 L. Schmid and T. Franke, *Lab on a Chip*, 2013, **13**, 1691–1694.
331 J. C. Brenker, D. J. Collins, H. Van Phan, T. Alan and A. Neild, *Lab on a Chip*, 2016, **16**, 1675–1683.
332 M. Sesen, T. Alan and A. Neild, *Lab on a Chip*, 2015, **15**, 3030–3038.
333 J. H. Jung, G. Destgeer, B. Ha, J. Park and H. J. Sung, *Lab on a Chip*, 2016, **16**, 3235–3243.
334 M. Sesen, C. Devendran, S. Malikides, T. Alan and A. Neild, *Lab on a Chip*, 2017, **17**, 438–447.
335 M. Sesen, T. Alan and A. Neild, *Lab on a Chip*, 2014, **14**, 3325–3333.
336 J. H. Jung, G. Destgeer, J. Park, H. Ahmed, K. Park and H. J. Sung, *Analytical Chemistry*, 2017, **89**, 2211–2215.
337 A. Lenshof, M. Evander, T. Laurell and J. Nilsson, *Lab on a Chip*, 2012, **12**, 684–695.
338 M. Grundy, W. Bolek, W. Coakley and E. Benes, *Journal of immunological methods*, 1993, **165**, 47–57.
339 M. K. Araz, C.-H. Lee and A. Lal, Ultrasonics, 2003 IEEE Symposium on, 2003, pp. 1111–1114.
340 I. Gralinski, T. Alan and A. Neild, *The Journal of the Acoustical Society of America*, 2012, **132**, 2978–2987.
341 I. Gralinski, S. Raymond, T. Alan and A. Neild, *Journal of Applied Physics*, 2014, **115**, 054505.
342 Z. Mao, P. Li, M. Wu, H. Bachman, N. Mesyngier, X. Guo, S. Liu, F. Costanzo and T. J. Huang, *ACS Nano*, 2017, **11**, 603–612.
343 E. T. Thostenson, Z. Ren and T.-W. Chou, *Composites Science and Technology*, 2001, **61**, 1899–1912.
344 R. E. Smalley, M. S. Dresselhaus, G. Dresselhaus and P. Avouris, *Carbon nanotubes: synthesis, structure, properties, and applications*, Springer Science & Business Media, 2003, vol. 80.
345 M. Whitby and N. Quirke, *Nature Nanotechnology*, 2007, **2**, 87–94.
346 A. Noy, H. G. Park, F. Fornasiero, J. K. Holt, C. P. Grigoropoulos and O. Bakajin, *Nano Today*, 2007, **2**, 22–29.
347 D. Mattia and Y. Gogotsi, *Microfluidics and Nanofluidics*, 2008, **5**, 289–305.
348 M. D. Haslam and B. Raeymaekers, *Composites Part B: Engineering*, 2014, **60**, 91–97.
349 C. Strobl, C. Schäflein, U. Beierlein, J. Ebbecke and A. Wixforth, *Applied Physics Letters*, 2004, **85**, 1427–1429.
350 Z. Ma, J. Guo, Y. J. Liu and Y. Ai, *Nanoscale*, 2015, **7**, 14047–14054.
351 X. Kong, C. Deneke, H. Schmidt, D. Thurmer, H. Ji, M. Bauer and O. Schmidt, *Applied Physics Letters*, 2010, **96**, 134105.
352 Y. Chen, X. Ding, S.-C. S. Lin, S. Yang, P.-H. Huang, N. Nama, Y. Zhao, A. A. Nawaz, F. Guo, W. Wang *et al.*, *ACS Nano*, 2013, **7**, 3306.
353 K. M. Seemann, J. Ebbecke and A. Wixforth, *Nanotechnology*, 2006, **17**, 4529.
354 M. Miansari, A. Qi, L. Y. Yeo and J. R. Friend, *Advanced Functional Materials*, 2015, **25**, 1014–1023.
355 M. Wu, Y. Ouyang, Z. Wang, R. Zhang, P.-H. Huang, C. Chen, H. Li, P. Li, D. Quinn, M. Dao *et al.*, *Proceedings of the National Academy of Sciences*, 2017, 201709210.
356 A. Piruska, M. Gong, J. V. Sweedler and P. W. Bohn, *Chemical Society Reviews*, 2010, **39**, 1060–1072.
357 T. A. Zangle, A. Mani and J. G. Santiago, *Chemical Society Reviews*, 2010, **39**, 1014–1035.
358 J. W. van Honschoten, N. Brunets and N. R. Tas, *Chemical Society Reviews*, 2010, **39**, 1096–1114.
359 E. B. Kalman, I. Vlassiouk and Z. S. Siwy, *Advanced Materials*,

2008, **20**, 293–297.
360 R. B. Schoch, J. Han and P. Renaud, *Reviews of Modern Physics*, 2008, **80**, 839.
361 S. J. Kim, L. D. Li and J. Han, *Langmuir*, 2009, **25**, 7759–7765.
362 Q. Pu, J. Yun, H. Temkin and S. Liu, *Nano Letters*, 2004, **4**, 1099–1103.
363 S. J. Kim, Y.-C. Wang, J. H. Lee, H. Jang and J. Han, *Physical Review Letters*, 2007, **99**, 044501.
364 L. J. Guo, X. Cheng and C.-F. Chou, *Nano Letters*, 2004, **4**, 69–73.
365 M. Foquet, J. Korlach, W. Zipfel, W. W. Webb and H. G. Craighead, *Analytical Chemistry*, 2002, **74**, 1415–1422.
366 S. J. Kim, S. H. Ko, K. H. Kang and J. Han, *Nature Nanotechnology*, 2010, **5**, 297–301.
367 L. Bocquet and E. Charlaix, *Chemical Society Reviews*, 2010, **39**, 1073–1095.
368 W. v. Sparreboom, A. Van Den Berg and J. Eijkel, *Nature Nanotechnology*, 2009, **4**, 713–720.
369 K. M. Weerakoon-Ratnayake, C. E. O'Neil, F. I. Uba and S. A. Soper, *Lab on a Chip*, 2017, **17**, 362–381.
370 Z. Insepov, D. Wolf and A. Hassanein, *Nano Letters*, 2006, **6**, 1893–1895.
371 M. Longhurst and N. Quirke, *Nano Letters*, 2007, **7**, 3324–3328.
372 K. F. Rinne, S. Gekle, D. J. Bonthuis and R. R. Netz, *Nano Letters*, 2012, **12**, 1780–1783.
373 J. Goldberger, R. Fan and P. Yang, *Accounts of Chemical Research*, 2006, **39**, 239–248.
374 J. Edel, A. Ivanov and M. Kim, *Nanofluidics*, Royal Society of Chemistry, 2016, vol. 41.
375 K.-H. Lin, C.-M. Lai, C.-C. Pan, J.-I. Chyi, J.-W. Shi, S.-Z. Sun, C.-F. Chang and C.-K. Sun, *Nature Nanotechnology*, 2007, **2**, 704–708.
376 T. Pezeril, C. Klieber, S. Andrieu and K. Nelson, *Physical Review Letters*, 2009, **102**, 107402.
377 P. van Capel, E. Péronne and J. Dijkhuis, *Ultrasonics*, 2015, **56**, 36–51.
378 F. I. Uba, B. Hu, K. Weerakoon-Ratnayake, N. Oliver-Calixte and S. A. Soper, *Lab on a Chip*, 2015, **15**, 1038–1049.
379 D. Mijatovic, J. Eijkel and A. Van Den Berg, *Lab on a Chip*, 2005, **5**, 492–500.
380 J. Wu, R. Chantiwas, A. Amirsadeghi, S. A. Soper and S. Park, *Lab on a Chip*, 2011, **11**, 2984–2989.
381 J. O. Tegenfeldt, C. Prinz, H. Cao, S. Chou, W. W. Reisner, R. Riehn, Y. M. Wang, E. C. Cox, J. C. Sturm, P. Silberzan *et al.*, *Proceedings of the National Academy of Sciences of the United States of America*, 2004, **101**, 10979–10983.
382 L. H. Thamdrup, A. Klukowska and A. Kristensen, *Nanotechnology*, 2008, **19**, 125301.
383 W. Reisner, K. J. Morton, R. Riehn, Y. M. Wang, Z. Yu, M. Rosen, J. C. Sturm, S. Y. Chou, E. Frey and R. H. Austin, *Physical Review Letters*, 2005, **94**, 196101.
384 P. Utko, F. Persson, A. Kristensen and N. B. Larsen, *Lab on a Chip*, 2011, **11**, 303–308.
385 H. Takagi, R. Maeda, N. Hosoda and T. Suga, *Applied Physics Letters*, 1999, **74**, 2387–2389.